Universitat Autònoma de Barcelona

LAB-ON-A-CHIP INTEGRATION OF THE BIMODAL WAVEGUIDE NANOINTERFEROMETRIC BIOSENSOR

DANIEL GRAJALES GARCÍA

LAB-ON-A-CHIP INTEGRATION OF THE BIMODAL WAVEGUIDE NANOINTERFEROMETRIC BIOSENSOR

A dissertation submitted in partial fulfilment for the degree of

Doctor of Philosophy in Electronics and Telecommunications Engineering.

Departament d'Enginyeria Electrònica

Escola d'Enginyeria

Universitat Autònoma de Barcelona

Institut Català de Nanociència i Nanotecnologia (ICN2)

July 2018

DR. LAURA M. LECHUGA
DIRECTOR

DR. DAVID JIMÉNEZ
TUTOR

DR. JOSE RAMON SENDRA
CO-DIRECTOR

DANIEL GRAJALES GARCÍA
AUTHOR

A Mamá & Papá…

Por plantar la semilla del conocimiento y curiosidad…

Caro & Adolfo...

Por crecer juntos siempre aprendiendo y apoyándonos…

Nat & Giu.

Por la inspiración que me dan cada día…

"The important thing is not to stop questioning. Curiosity has its own reason for existing."

- Albert Einstein.

ABSTRACT

This doctoral Thesis focuses on the integration of the novel Bimodal Waveguide Nanointerferometric Biosensor (BiMW) into a Lab-On-a-Chip (LOC) platform which can allow the direct detection of biomarkers for diseases diagnosis directly in the patient´s sample. Even if real bioanalytical applications have been widely reported by our group using the BiMW as an optical transducer, its integration into a pre-commercial and portable LOC platform remains a difficult challenge. In this Thesis, we have accomplished optimizations in the waveguide structure, optical subsystems, microfluidic integration and read-out subsystems which greatly will help on its road towards a portable point-of-care device for on-site applications.

Firstly, the BiMW previously developed in our group has been in-deep analysed, setting the tools for its modelling, simulation and experimental characterization. Its design has been optimized for sensing with visible light coupled in a rib waveguide with nanometric dimensions. Simulation studies of the BiMW included: rib size optimization for maximizing its sensitivity as biosensor, the effects of the length of the sensor and the location of the step junction. With the aim to solve the challenges related to the light in-coupling in nanometric structures, two kinds of tapers have been designed, simulated, fabricated and finally characterized, demonstrating the advantages and disadvantages of such solution. With the aim to overcome the issues related to the interferometric signal readout, a chirp modulation system has been theoretically designed and experimentally implemented and characterized. Splitter series of 1x2, 1x4 and 1x8 for on-chip multiplexing have been designed, simulated, fabricated and characterized. A multiplexed detection readout method has been implemented via software and compared to analogue methods. Finally, the remaining challenges in terms of integration towards a final POC device are discussed.

The work done in this Thesis has greatly helped to push forward the integration of the BiMW nanointerferometric biosensor into a future portable biosensing platform intended for on-site use

RESUMEN

La presente tesis doctoral se centra en la integración del novedoso biosensor nanointerferométrico de guías de onda bimodal (BiMW biosensor) en una plataforma lab-on-chip para la detección temprana de biomarcadores relacionados con el diagnóstico clínico de enfermedades directamente en la muestra del paciente. Nuestro grupo ya ha demostrado a nivel de laboratorio la gran utilidad del biosensor BiMW para la detección de biomarcadores clínicos, pero su integración en una plataforma portátil tipo LOC que pueda ser empleada fuera del laboratorio sigue constituyendo un gran reto científico y tecnológico. Con este objetivo en mente, en esta Tesis hemos llevado a cabo optimizaciones en el diseño de las guías de ondas, sistemas de acoplamiento de la luz, la microfluidica, y los sistemas de lectura que sin duda ayudaran a conseguir su integración en un sistema portátil de análisis.

Para ello se ha llevado a cabo un estudio en profundidad del sensor BiMW previamente desarrollado mediante herramientas de modelado ysimulación. Su diseño ha sido optimizado para el sensado con luz visible acoplada en una guía de onda tipo rib con dimensiones nanométricas. Se han realizado estudios para optimizar: las dimensiones del rib para maximizar la sensibilidad del sensor, el efecto de la longitud total del dispositivo y la ubicación del escalón bimodal. Con el propósito de resolver el reto relacionado con el acople de la luz en las guías nanométricas de la BiMW, dos tipos de estructuras con disminuciones graduales han sido diseñadas, simuladas, fabricadas y evaluadas, discutiendo las ventajas e inconvenientes de dicha aproximación. Para conseguir una señal lineal de medida, evitando la lectura interferométrica, se ha diseñado, implementado y evaluado experimentalmente un sistema de modulación. Para conseguir un biosensor de respuesta multiplexada se han diseñado, simulado, fabricado y finalmente caracterizados divisores 1x2, 1x4 y 1x8. Además, se ha implementado un método de lectura multiplexada por software y comparado con los métodos analógicos. Por último, se discuten los pasos que quedan para conseguir el dispositivo POC final.

El trabajo de esta Tesis doctoral ha ayudado a conseguir la integración del biosensor nanointerferométrico BiMW en una futura plataforma tipo LOC que pueda ser empleada fuera del entorno del laboratorio.

ACKNOWLEDGEMENTS

During my PhD, I had the opportunity to interact with great talented people in science, art, culture and engineering. I learnt as much as I could from everybody and this is my time to thank for their contribution to make this work possible. This work would not be possible without the great help of all the giants I stand on.

Firstly, I would like to thank my supervisor Prof. Laura M. Lechuga. She was an example of leadership, hard work, imagination, resilience. She was always positive, even in the hard times. She had the ability to let me divagate and overthink my ideas, make my mistakes, and then take me back in track when I was dreaming too far away of my Thesis line of research. I learnt a lot from her about how to do research, to work in teams, to keep always updated, to keep the hard work and to keep motivated. Thanks for the trust deposited in me and for teaching me so much about life.

Thanks to my Thesis co-supervisor, Dr. Jose Ramón Sendra Sendra. You were an example of leadership, of vocation, of keeping track on science no matter what happens around your world. You spread your motivation to get the work done, to get hands-on, but at the same time, to think before to do and to explain what we observe. You always had a phrase for everything and all these weekly meetings were the best way to keep me on track. Thanks for taking me back on track when I was also rambling too much. Thanks for spreading your love for science.

Thanks to my Thesis tutor Dr. David Jiménez. You were always helpful and interested in the progress of the overall research. Thanks for listening to my ideas.

Special thanks to Prof. Carlos Domínguez from IMB-CNM-CSIC. It was always a pleasure to discuss ideas with you. You were such a source of ideas, and you had always the answers. I love your way of working and your positive energy at all times, spreading a good vibe wherever you are. Your presence was always noticed in any meeting with always a positive effect. Thank you so much for making the right questions, for making everything possible and for spreading your good energy.

Special thanks to Dr. Adrian Fernandez, to Dr. Ana Belén González, to Dr. Jesus Maldonado and to Dr. Jhonattan Cordoba for sharing the passion for science and photonics. I appreciate your friendship at life and work as well. Thank you for keeping everybody motivated. Thanks to Chantal Vilà from PROMAX. Thanks to Dr. César

Sánchez Huertas, to Dr. David Fariña, to Dr. Daphne Duval and Dr. Stefania Dante. Your guidance and inspiration was key to this Thesis.

Thanks to Dr. Isaac Rodriguez from the chemical transducers group from IMB-CNM-CSIC for his guidance in the fabrication of SU-8 moulds. Thanks for sharing your knowledge and passion for science and technology.

Thanks to Albert Serrano, for your friendship and for reminding me the beauty of science.

Thanks to Dr. Jessica Llop and to Dr. Rebeca Diéguez, for combating all our chaos with love and patience. Thanks to Dr. Mar Alvarez, to Dr. M. Carmen Estévez, Dr. Borja Sepulveda, Dr. Laura G. Carrascosa, Dr. Salomon Marquez, Dr. Bert Otte, Dr. Maria Soler, Dr. Iraís Solis, Dr. David Regatos, Dr. Antoni Homs, Dr. Sonia Herranz, Dr. Carlos Caro. Thanks to Dr. Cristina Kurachi, your knowledge is surpassed only by your heart. You are an example of life.

Thanks to Blanca Chocarro, to Gerardo López, to Cristina Peláez, to Santos Domínguez, to Patricia Ramirez, to Nuria Fabri, to Olalla Calvo, to Roger Guiu, to Heriberto Diaz, for your enthusiasm and positive energy every day.

Special thanks to Jens Hovik, to Crispin Szydzik, Dr. Iulia Arghir, Dr. Frehun Tsige, Dr. Melissa Rodríguez, Sebastian, Jesus Rebull, Albert Piqué, Remí Oudart for sharing the passion for science across continents. It has been a pleasure and I hope we meet again in the future!

Thanks to the ICN2 family: Xavi Ros, Paul, Isma and Dani, Natalia, Anabel, Laura. Thanks to the communication team at ICN2: Alex Arguemí, Ana de La Osa and Damaso Torres. Thanks for sharing many adventures, talks and discussions.

Special thanks to Rafael de Leon, I want to thank your patience when discussing the 3D fabrication of moulds and other components. It was always a pleasure to visit you in your workshop. I wish you the best in your new adventures to come.

Thanks to my friend Rafael Sibilo, for your inspiration, for keeping the passion for science, for your help, support, wisdom and advices. I hope we meet again. Thanks to Dr. Nuria Conde, Esteban, Rosen and Dr. Fernanda Píres. Your passion for tech and science keeps me inspired.

Then, I would like to thank to CONACYT (CVU 397275). I could not live without your support. Thank you!

Finally, I want to thank to my parents and siblings, and my new family: Nat and Giu. Thank you so much for all the nights you gave me a word of support, a hug, a warm bed, a kiss, an advice, love. These lines are for you. I love you all!

Finalmente, agradecer a quienes plantaron la semilla de la pasión por la ciencia: mis padres, mis hermanos. Y gracias también a mi nueva familia, Natalia y Giulia. Muchas gracias por todas las noches que me dieron alguna palabra de aliento, un abrazo, una cama caliente, un beso, un consejo, amor. Estas líneas van para ustedes. Los amo.

¡Muchas gracias a todos!

CONTENTS

MOTIVATION, AIM AND THESIS OUTLINE

Nowadays, the majority of tests for clinical or environmental diagnostics are done in full-equipped laboratories, using complex techniques with time consuming procedures and requiring specialized technicians. Due to the increasing demand of the ageing society in the industrialized world and the lack of resources in developing countries, there is a clear need for diagnostic methods able to provide real-time, multiplexed, sensitive and label-free detection at an affordable cost. One of the best solution is offered by the use of dedicated biosensor devices. A biosensor is a device capable of real-time detection of a biomolecular interaction, transducing it through a physical variable into information which after further processing can be interpreted by the final user (i.e. the doctor or even the patient himself). Such biosensors are the central core of Lab-on-a-Chip platforms (LOC). In a LOC platform, several subsystems take jobs in order to fulfil the recognition of the analyte to be detected: sample preparation (if required) and delivery, biomolecular interaction process, physical transduction, data information processing and display without forgetting the thermal and/or mechanical compensation. However, to orchestrate all different subsystems harmoniously is a challenge in terms of components integration and requires a holistic approach.

Interferometry is a powerful sensitive technique widely employed in science and industry. For example, IO interferometers are at the core of the internet revolution employed by the telecommunications industry as modulators (i.e. Mach-Zehnder Interferometer Modulators). The Bimodal Waveguide (BiMW) Interferometer Biosensor proposed by our group, simplifies the fabrication of the integrated MZI while maintaining the same benefits inherit to the IO interferometers (i.e. sensitivity, low-cost production through standard compatible CMOS processes, high level of integration, etc.).

The first part of this Thesis introduces the BiMW nanointerferometric biosensor and explains the different subsystems which are required to achieve a final LOC platform. Then diverse optimizations of the BiMW device are proposed, designed, fabricated, tested and discussed. In the following sections, the Thesis discusses the main challenges related to the integration of the BiMW nanointerferometric biosensor: light in- and out-coupling in nanometric waveguides, optical modulation to provide linear readings, implementation of multiplexing capabilities, microfluidics flow cells and coupling with the multiplexed sensor. The Thesis is organised as follows:

Chapter 1 provides a general introduction to biosensors and an overview of the most important IO based biosensors with a description of the state-of-the-art. Afterwards, it clarifies the physics behind the operation of the bimodal waveguide nanointerferometer and its application as biosensor. Then, it lists the difficulties related to the integration og interferometric biosensors in LOC platforms.

Chapter 2 shows the simulations and fabrication of the current BiMW design. Next, different sub-systems required for its experimental characterization are explained and results of the BiMW biosensor are described.

Chapter 3 describes the areas for improvement and optimization of the BiMW biosensor integration, with the final goal of providing a low-cost and portable prototype platform. Each section includes the theory and simulations behind the proposed optimization and the main experimental results.

Chapter 4 deals with one of the main challenges for the integration: the light in- and out-coupling to micrometric and nanometric waveguide structures. This chapter discusses the state-of-the-art solutions and proposes two novel ones: a vertically stacked taper and an inverted one. Their design, simulation, fabrication, optical characterization and comparison are showed as well.

Chapter 5 provides a description of the main modulation system as tools designed to overcome a variety of issues innate to interferometric signals. Then, the design, simulation, experimental evaluation and advantages of a proposed chirp modulation scheme are showed and discussed.

Chapter 6 provides a discussion of the multiplexing requirements for biosensing. Different solutions are simulated in order to select one for its fabrication and experimental evaluation. Read-out mechanisms are a challenge for multiplexed detections. A proposed software-based readout mechanism is described, characterized and compared with other readout systems. Finally, an experimental demonstration of the multiplexed capabilities of the BiMW is presented.

The general conclusions and future outlook of this Doctoral Thesis are summarized in **Chapter 7**.

LIST OF ABBREVIATIONS AND ACRONYMS

BiMW	Bimodal Waveguide
BMS	Bimodal Section
BMSsa	Bimodal Section with sensing area
CCD	Charge-coupled Device
CROW	Coupled-resonator optical-waveguide
DB	Database
DI	Deionized Water
DNA	Deoxyribonucleic Acid
EIM	Effective Index Method
EME	Eigen Mode Expansion Method
FDM	Finite Differences Method
FEM	Finite Element Mode
FFT	Fast Fourier Transform
FMM	Film Mode Matching
GUI	Graphical User Interface
IC	Integrated Circuit
IO	Integrated Optics
LD	Laser Diode
LHS	Left Hand Side
LIGO	Laser Interferometer for Gravitational Waves Observatory
LOC	Lab-on-a-Chip
LOD	Limit of Detection
MZI	Mach-Zehnder Interferometer
ND	Neutral Density filter
OOLV	Object-Oriented Labview

PC	Photonic Crystal
PD	Photodiode
PDMS	Polydimethylsiloxane
PECVD	Plasma Enhanced Chemical Vapour Deposition
PIC	Photonic Integrated Circuit
PID	Proportional Integrative Derivative Control
PMMA	Poly-(methyl methacrylate)
RHS	Right Hand Side
RIU	Refractive Index Units
RNA	Ribonucleic Acid
ROI	Region of Interest
RR	Ring Resonator
RT	Real Time
SM	Single Mode
SMS	Single Mode Section
SMSsa	Single Mode Section with sensing area
SIMO	Single Input, Multiple Output
TIR	Total Internal Reflection
TEC	Thermoelectric Cooling
WGM	Whispering Gallery Mode
XML	Extensible Markup Language
YI	Young Interferometer

1 INTRODUCTION

"There can be life after breast cancer. The prerequisite is early detection"

- *Ann Jillian*

This chapter provides a general introduction to biosensors and an overview to IO based biosensors describing the state-of-the-art. Then, it lists the characteristic of interferometric IO sensors, the difficulties related to the integration of LOC platforms and, finally, a complete description of the BiMW nanointerferometric biosensor.

Life is fragile. It is a concern and obligation of humankind to foster its development and continuity. We are biology thus, biological advances impact our quality of life directly. For example, after the finding of bacteria and microorganisms due to the microscopy advances of Leeuwenhoek, or the discovery of the biological origin of some illnesses by L. Pasteur, the life expectancy has increased uninterruptedly [1]. In order to protect life, we need to detect, track and identify different biological players present in our food, environment and in our body. Thus, there is a need for a rapid, direct, label-free, non-invasive detection of biological elements (i.e. proteins, viruses, bacteria, DNA, RNA, etc.). Diseases with problematic pictures are among the main drivers of the technological development in the area of this doctoral Thesis. Normally, the detection of these diseases requires trained personnel operating in complex laboratory setups, sample labelling or petri cultures for example, which are time-consuming.

In other hand, information technologies revolution has brought processing power and electronic peripherals right to the palm of our hand. It is of global interest to explode such

tools and use them to our benefit, particularly in remote areas with a lack of proper laboratory or hospital installations. For example, commercial developments for mobile glucose detection and monitoring could be represented by myDario[1] glucometer and iHealth align glucometer[2]. Kanchi et al. have published a review of different detection methods based in smart phones for Africa [2]. Among the applications, it is possible to find detection of pathogens in water [3], spectrometry [4], lateral flow immunoassays [5], HIV detection [6], etc. Efforts to detect Zika, Dengue and Chikungunya in Latina America are showing promising results as showed by Ganduli et al. [7], however, expensive laboratory setups are yet required. In that sense, Caliendo et al. recommend stimulating the research and development in portable diagnostic techniques [8]. Such devices are called Lab-on-a-Chip (LOC) which aim to include all the required units (sample preparation, sample deliver, detection, reporting to the user, etc.) to perform accurate multi-parametric analysis with all the assay steps normally carried out in an analytical chemistry laboratory. But even if the different units of the LOCs are presented as mature technologies, their integration into a complete platform remains a challenge and very few complete operational prototypes have emerged with real applications [9,10]. A biosensor lies at the core of these LOCs. A biosensor is defined as an analytical device capable to detect biological interactions through a bioreceptor (DNA, antibodies, bacteria, cells, etc.) and translate them into electrical signals thanks to physical-chemical properties of a transducer. These signals can be decoded into useful information to the final user (i.e. a health expert, or patient itself). Depending on the detection environment, the detection range of interest, the requirements of reusability and time of the essay and the own nature of the organism or biological molecule to detect (i.e. analyte), different biosensor transducers are available: electrochemical, optical and mechanical, mainly.

1.1 Optical biosensors

Since the dimensions of the biomolecules of interest to human health lay in the range of hundreds of nanometres to micrometres, it is clear that light wavelengths and consequently optical devices, offer an exceptional tool. Optical biosensors are defined as sensors which make use of optical principles for the transduction of a biomolecularinteraction into a suitable output signal [11]. They offer the advantage of real time and high sensitive detection without amplification or labelling, shielding to electromagnetic interference (EMI), the possibility of integration into a complete LOC and the capability of low-cost fabrication thanks to mass production in microelectronic

1 http://intro.mydario.com
2 https://ihealthlabs.com

foundries using standard Silicon microfabrication techniques. With the latest developments of microelectronics, nanofabrication and nanophotonics, it is possible to provide the required devices to perform rapid, simple, sensitive and inexpensive detection [12,13]. Several parameters of the light wave can be used as indicators of analyte binding events: intensity (amplitude), frequency (or wavelength), phase, polarization, etc. Moreover, the interactions of light with matter results in a wide family of sensors based in different phenomena: transmission, absorption, reflection, luminescence, fluorescence, Raman spectroscopy, plasmon resonance, interferometry, etc. The majority of optical biosensors rely in the evanescent wave phenome as detection principle, the evanescent field working principle: when a wave is confined due to total internal reflection (TIR) into a dielectric structure with a difference of dielectric constants (or refractive index) between the core and the cladding, the majority of the wave energy is guided in the core with a higher dielectric constant, yet, there is an exponential decay at the boundary between the core and the cladding. This evanescent tail penetrates tens to hundreds of nanometres and is affected by changes in the refractive index of the cladding (or sensing area in the case of biosensors). Thus, only changes occurring in the surface of the sensor will affect the propagation and the effective refractive index of the whole lightwave resulting in a natural filter to changes occurring in the bulk of the sensing area. This makes biosensors based in the evanescent wave principle ideal candidates for affinity-based detections without the need of molecular labels (fluorescent or radioactive tags) permitting label-free detection.

Figure 1.1 illustrates the fundamental and a first order mode confined in a planar waveguide. In this case, antibodies are bound to the surface acting as bioreceptors modifying the effective refractive index of both modes upon the binding of the analytes. It is remarkable to mention that the first order mode has a larger evanescent tail as compared to the fundamental one.

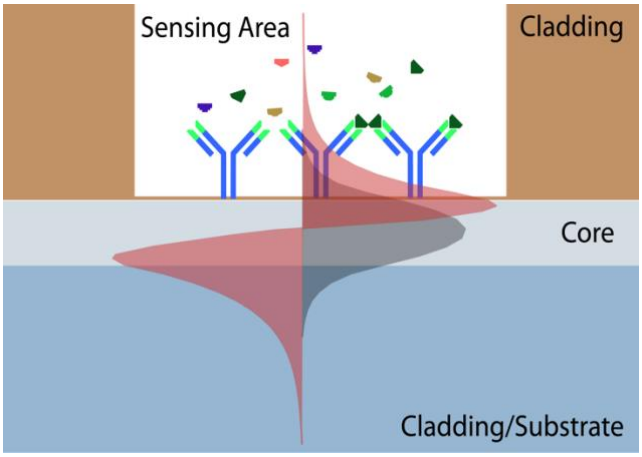

Figure 1.1 Scheme to illustrate the principle of evanescent wave based biosensors. The light fundamental (grey) and the first order mode (red) are showed. Antibodies bound to the surface act as bioreceptors and the biomolecular interaction with their specific antigens modify the effective refractive index of both modes.

1.1.1 Parameters of sensor evaluation

Sensitivity (S) represents the magnitude of the transducer response (S_r) to the change in the analyte concentration. However, since it depends on the transduction type and the nature of the analyte, it is not possible to perform a direct comparison using only this parameter. In other hand, *resolution* is the smallest variation that can be accurately measured $\Delta S_{r,min}$. The resolution is limited by the noise sources of the experimental set-up employed (mechanical and thermal instabilities, detector noise, light source variations, etc.) and is estimated as three times the standard deviation (σ) of the noise of the system [14].

Sensitivity and resolution are then combined to define the *Limit of Detection* (LOD), which allow us to compare different sensor configurations:

$$LOD = \frac{\Delta S_{r,min}}{S} \qquad (1.1)$$

where S is the sensor sensitivity. When there is a homogeneous variation of the refractive index in the bulk of the sensing area, the most convenient form of expressing the LOD is in terms of Refractive Index Units (RIU). In the case of a variation of the refractive index due to a molecular interaction taking place only in a thin layer in the proximity of the sensor surface (i.e., surface sensing), it is more convenient to express the LOD in terms of analyte concentration or surface density.

1.2 Biosensors based in integrated optics (IO)

Marcatili and Miller predicted the rise of integrated optics in 1969 after the invention of the laser [15,16]. They envisioned optical couplers which could act as transistors guiding the light to different outputs according to the design. They foresaw that photonic integrated circuits (PICs) could perform several complex optical operations and that they could be made by properly manufacturing several optical components into a single chip using microelectronics fabrication techniques. It could be compared as integrated circuits (ICs) using light couplers instead of transistors and photons instead of electrons. Despite the efforts to integrate rare earth materials, biological materials or polymers into PICs, silicon remains as the workhorse of the IO research and industry. Silicon is widely available in the earth and exhibits good mechanical stability, optical properties which can be controlled by variations on shape, structure, dopants concentrations or chemically bonding to other materials as silicon nitride (Si_3N_4). IO based devices fabricated in Si or Si_3N_4 can be employed as highly sensitivity biosensors by using the evanescent wave sensing mechanism. Ring resonators

Biosensors based in ring resonators (RR) show a great potential because of its integration feasibility. In this configuration, light is coupled into a ring waveguide and propagates as Whispering Gallery Modes (WGM) resonating at a selected frequency. The energy will keep resonating until vanished due to dispersion or absorption of photons. The Q factor is an indicator of the efficiency of the resonator by relating the stored to the dissipated energy. Q factors as high as 10^{10} have been reported [17]. The effective length L_{eff} is given by:

$$L_{eff} = Q\frac{\lambda}{2\pi n} \qquad (1.2)$$

where n is the resonator refractive index and the resonance wavelength, λ, is given by:

$$\lambda = 2\pi r\frac{n_{eff}}{m} \qquad (1.3)$$

where r is the ring radius, n_{eff} is the waveguide effective refractive index and m an integer number. When used as biosensors, the surface of the ring is functionalized with the bioreceptors. Among the advantages of ring resonators, there is the integration possibilities for multiplex sensing [18], enhancements in microfluidics systems, in-coupling and read-out. In terms of applications, relevant biomarkers have been tested [19]. Achieving limits of detection (LOD) in the order of 10^{-6} RIU.

However, most of the ring resonators sensors need bulky and expensive tunable lasers in order to excite the resonant cavity. In this sense, efforts to make a system which requires only a fixed wavelength to excite the RR have been done by Jiang et al [20] adding a coupled-resonator optical-waveguide (CROW). Commercial solutions are being offered by companies like Genalyte[3] which sells the Maverick system.

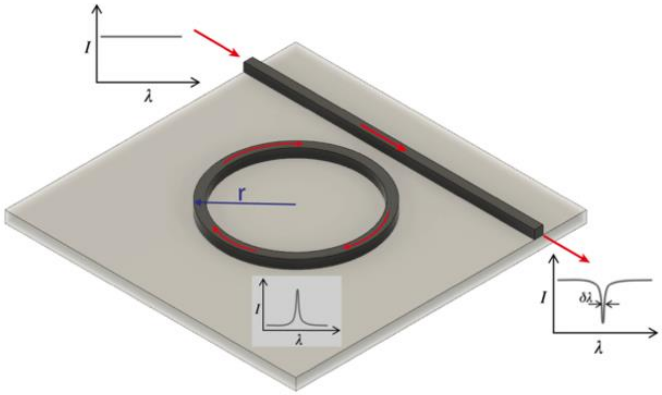

Figure 1.2 Example of a conventional ring resonator.

1.2.1 Photonic crystals

A photonic crystal (PC) is a periodic structure of materials with different refractive index and periods in the order of dimensions of the wavelength of the electromagnetic wave of interest. Due to their periodic nature, there are a range of wavelengths not propagated in the PC waveguide (photonic bandgap). The photonic bandgap will experiment shifts depending in defects introduced in the structure. In the case of the applications of PC as biosensors, the bioreceptor and the analyte will be the defects introduced to the structure [21]. The quality factor Q of a PC is given by:

$$Q = \frac{f_0}{\Delta f}, \qquad (1.4)$$

where f_0 is the peak frequency and Δf is the bandwidth of the bandgap. As an effort to permit multiplexed detections using PCs, an array of three nanocavities coupled to a PC waveguide was developed by Dorfner et al [22], however, due to a low Q factor, a non-competitive LOD of 10^{-2} RIU in bulk was obtained. In an effort to improve the LOD, multiple hole defects (MHDs) were introduced increasing the surface area available for label-free detection as showed in Figure 1.3a [23]. Another approach for multiplexed detections was the addition of a PC waveguide filter connected in series to each PC microcavity sensor. So, a transmission bandpass filter containing the

3 www.genalyte.com

resonances of the PCs allows the multiplexed detection using a single input and output as showed in Figure 1.3b [24]. However, its integration into a fully commercial system remains a challenge. Fabrication of PCs requires e-beam lithography increasing the cost and complicating its final integration into a disposable biosensor for clinical applications.

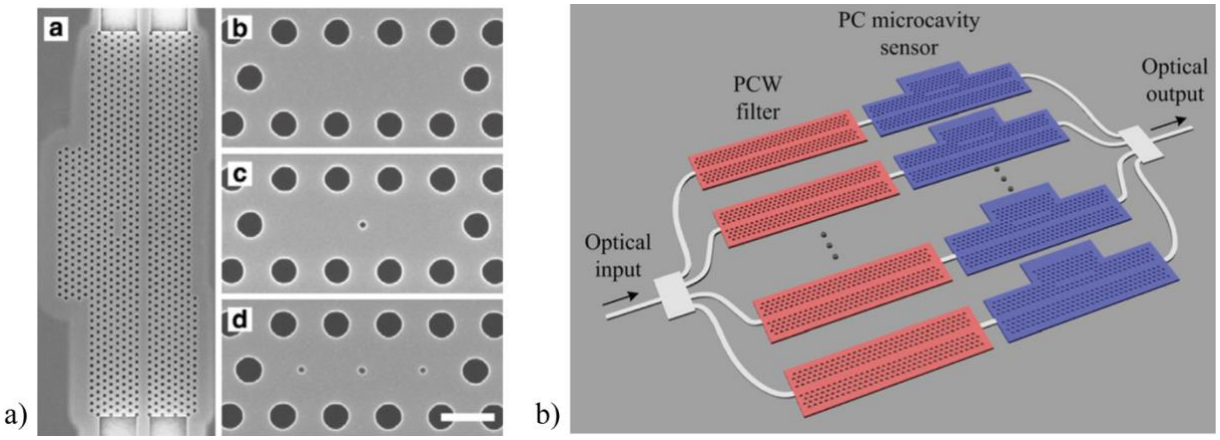

Figure 1.3. Advances in PCs biosensors. a) Multiple hole defects (MHDs) [23]**, with permission of the Optical Society of America. b) Transmission bandpass combined with PC sensor** [24]**, with permission of the Optical Society of America.**

1.2.2 Interferometers

Interferometry is a powerful metrology technique. Different interferometer schemes are widely use in science and technology applications such as gyroscopes, astronomic telescopes, or more recently, the detection of gravitational waves using the Laser Interferometer Gravitational-Wave Observatory (LIGO) [25]. Interferometry is a technique based in two waves interfering: one serves as reference and the second as a sensing probe. Due to changes in the refractive index of the sensing section, a phase shift between both signals will occur resulting in constructive and destructive interference. Three of the most popular configurations are discussed below.

1.2.2.1 Mach-Zehnder Interferometer

In a standard Mach-Zehnder Interferometer (MZI) configuration, the in-coupled light is split by a Y-junction into the sensing and the reference arm. The lightwave will experience different effective refractive indexes on each arm (n_{eff}^{r} for the reference arm and n_{eff}^{s} for the sensing arm) if a sensing process in occurring in the sensing arm and then the output intensity will vary from maximum to minimum as the sensing signal completes a whole 2π phase shift delay with regard to the reference one. The signal intensity I at the output depends on the phase change $\Delta\varphi(t)$,

$$I \propto cos\left(\Delta\varphi(t)\right) \qquad (1.5)$$

$$\Delta\varphi(t) = \frac{2\pi L}{\lambda}\left(n_{eff}^{s} - n_{eff}^{r}\right) \qquad (1.6)$$

where L is the length of the sensing arm, λ is the wavelength of the light, and n_{eff}^{s} and n_{eff}^{r} are the effective refractive indices of the guided modes in the sensing and reference arms, respectively. Figure 1.4 shows an illustration of the typical MZI for biosensing purposes. The first MZIs for biosensing applications based in silicon microelectronic fabrication technologies were reported in the 90's [26–28]. Since then, new configurations employing Silicon Nitride (Si_3N_4) as the core waveguide have been tested with the aim to improve its biosensing capabilities [26–29] achieving a sensitivity of up to $1x10^{-7}$ RIU [30]. Other waveguide structures based on silicon technology, like silicon wires, have been employed for constructing a MZI device [31,32]. Assemblies based on glass [33] or polymer [34] have been successfully implemented, but the LOD generally remains worse (~10^{-4} RIU) as compared to the silicon nitride- based MZIs. Alternatives to Si_3N_4 as a core layer have been suggested with the goal to improve cost-efficiency of the fabrication process using Si-technology, such as SiO_xN_y, deposited using plasma-enhanced chemical vapour deposition (PECVD) [35,36]. The majority of biomolecules are non-absorbent in the visible, avoiding any damage or light absorption making Si_3N_4 one of the best candidates for IO waveguides based sensors in the visible spectra.

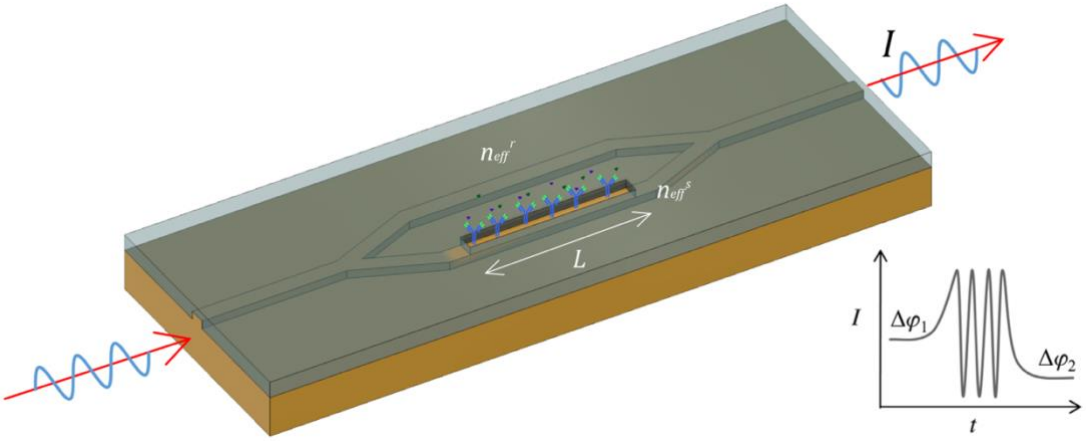

Figure 1.4 Standard integrated MZI for biosensing and representation of its interferometric output. The intensity variation is due to the periodic interference of the fundamental modes propagated on each arm with n_{eff}^{r} and n_{eff}^{s} and recombined at the output Y-junction. The phase change between both arms is related to the sensing length L.

Light in-coupling remains one of the major challenges in IO biosensors. One of the possible solutions is the use of grating couplers. For example, grating couplers were used to build a LOC MZI biosensor and a low-cost diode as a source reaching a LOD of 1.6×10^{-7} RIU [37], comparable with the most sensitive MZIs [38].

1.2.2.2 Young interferometer

Young Interferometers (YI) have a similar configuration to MZI but without the output Y junction to recombine the sensing and reference signal. Instead, each arm output radiates to a screen or Charge-Coupled Device (CCD) sensor, where they interfere creating a typical interference pattern. The phase difference between both reference and sensing arms is given by:

$$\Delta\varphi(t) = \frac{2\pi}{\lambda}\left[\frac{d \cdot x}{f} - \left(n_{eff}^{s} - n_{eff}^{r}\right)L\right] \qquad (1.7)$$

where d is the distance between the two arms, x the position of the interference pattern on the screen, f the distance between the sensor output and the camera and n_{eff}^{s} and n_{eff}^{r} are the effective refractive indices of the guided modes in the sensing and reference arms, respectively. Many advances have been achieved since the first integrated YI was proposed in 1994 [39]. The first application of this structure as a biosensor was reported in 2000 [40], reaching a detection limit of 9×10^{-8} RIU. Detection of analytes in human plasma were evaluated using this device [41]. A multi-analytical YI sensor of four branches (one of them as reference) was proposed by Ymeti et al. [42] showing the detection of herpes simplex virus type 1 (HSV-1), estimating that the detection limit can approach even the level of a single HSV-1 particle binding [43]. Recent advances have shown, theoretically, the possibility of applying the YI for analyte size-selective detection by launching multiple wavelengths, which allow discriminating between refractive index changes from different locations [44].

Other YI configurations, designed with two slab waveguides, have been developed [45]. This structure employs Ta_2O_5 as waveguide core, and is the most sensitive biosensor reported until now, with 9×10^{-9} RIU and 0.013 pg•mm^{-2} for bulk and surface sensitivity, respectively [46]. Another version of YI is the Dual Polarization Interferometry (DPI) sensor [47], which is composed by five layers, forming two slab waveguides. One slab waveguide is used as reference and the other senses the changes occurring on its surface. DPI uses TM and TE polarization, allowing determination of the thickness and the

refractive index of a film adsorbed on the sensor surface, by simultaneously measuring both polarizations. DPI is scarcely employed nowadays due to its complexity.

1.2.2.3 Bimodal interferometer

More recently, a modal interferometer fabricated in a single straight rib waveguide of Si_3N_4 enclosed in SiO_2 was proposed by Zinoviev et al. [48]. In the so-called Bimodal Waveguide (BiMW) Interferometer biosensor, light is coupled into a single mode rib waveguide where the core thickness is abruptly increased after a certain distance, allowing the propagation of the fundamental and first order modes of light of the same wavelength and polarization (see Figure 1.5). The interference between both guided modes is collected by a two-sectional photodetector at the end of the device. A sensing window is etched at the top of the bimodal section and bioreceptors are attached to the waveguide surface. Upon a biomolecular binding event, the refractive index on the surface will change, inducing a change of the effective refractive index of each mode. Since both modes have different propagation constants (thus, N_{eff}), the phase shift experienced by each mode will be different, obtaining an intensity variation across the vertical axis. The phase shift produced by a variation on the refractive index of the sensing area is quantified by monitoring the output intensity distribution given by the signal S_R:

$$S_R = \frac{I_{up} - I_{down}}{I_{up} + I_{down}} \qquad (1.8)$$

where I_{up} and I_{down} are the intensities measured in the upper and lower sections of a two-section photodiode (PD). The sensitivity level of the BiMW shows a LOD of 2.5×10^{-7} RIU in bulk comparable to other integrated interferometers.

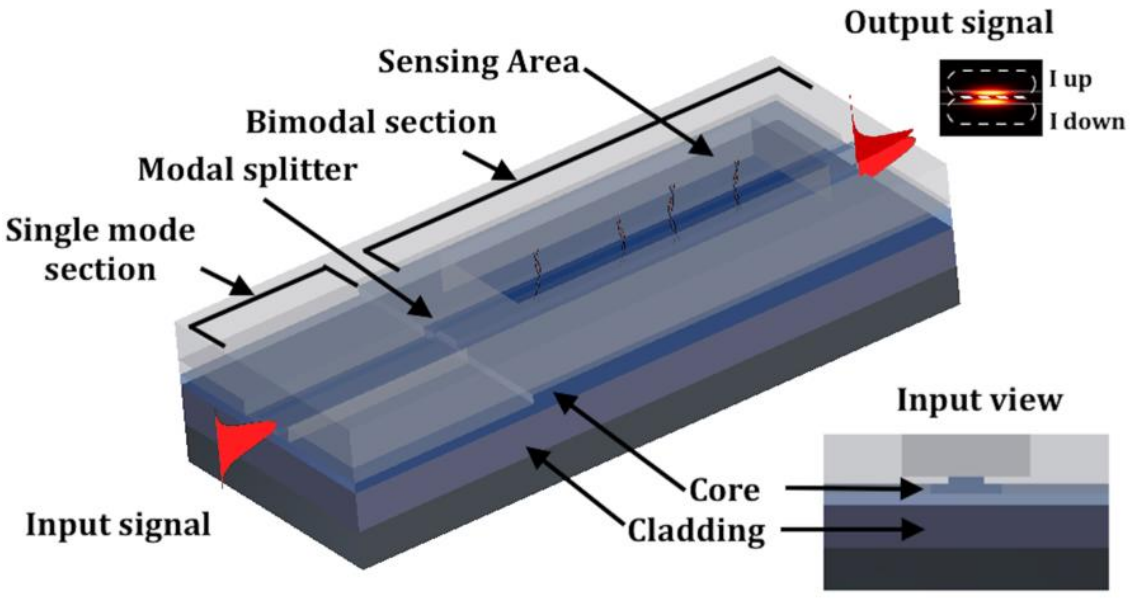

Figure 1.5 Bimodal waveguide interferometer (BiMW) sensor. The input signal is coupled into a single mode section. The core thickness is abruptly increased in the step junction (modal splitter) becoming a bimodal waveguide, allowing only the propagation of the fundamental (TE_{00} or TM_{00}) and the first order mode (TE_{10} or TM_{10}). A sensing window is opened for bio-functionalization and the output signal intensity is collected by a two-section photodiode.

1.2.3 Comparison of different IO biosensors for LOC integration

In an effort to compare different technologies, the LOD has become a standard indicator of the performance of IO biosensors. However, in terms of real life applications, it is worth to distinguish between the bulk and the surface sensitivity. The bulk sensitivity intrinsic to each biosensor is the variation of the effective index of a guided mode induced by a homogeneous variation of the external cladding medium index. Meanwhile, when acting as a biosensor, a thin layer (DNA, antibodies, RNA, the bioreceptor of interest) model can be adopted since only a region smaller than the penetration depth of the guided mode is involved in the biological interaction process [49]. In this case, the surface sensitivity is the variation of the effective refractive index of the guided mode as a function of the thickness of the biological layer. In most cases a refractive index of n=1.45 is assumed for a protein molecular layer. Table 1.1 shows the surface and bulk LODs for the above discussed biosensors.

Table 1.1 Surface and bulk LOD comparison for different IO biosensors

Technology	LOD in surface [pg•mm^{-2}]	LOD in bulk [RIU]
Interferometers (MZI and BiMW)	0.01-0.06	10^{-7} – 10^{-8}
Young Interferometer	0.013-0.75	10^{-8} – 10^{-9}
Micro ring resonators	1-3	10^{-5} – 10^{-7}
Photonic Crystals	0.4-7.5	10^{-4} – 10^{-5}

Where the surface LOD or surface mass coverage Γ (in pg•mm^{-2}) has been calculated according to:

$$\Gamma = \frac{(n_l - n_o)}{\left(\frac{\partial n_l}{\partial [C]}\right)\left(\frac{\partial N_{eff}}{\partial d_l}\right)} \Delta N_{eff} \qquad (1.9)$$

where d_l is the thickness of a biological layer covering the surface, n_l is the refractive index of the surface layer, n_o is the refractive index of the media, $[C]$ is the analyte concentration and N_{eff} is the effective refractive index [40,46]. As showed, the BiMW

biosensor is one of the most sensitive biosensors in surface terms and at the same time, it offers a much simpler fabrication process and integration feasibilities as compared to the other IO biosensors. This is the main reason why the BiMW biosensor is one of the most promising IO biosensing technologies.

1.3 Lab-on-a-Chip integration

An ideal biosensor should include all the steps of a traditional laboratory essay: sample treatment, specific receptors, signal transducers and electronics, multiple analytes receptors and the display with real-time results upon detection (see Figure 1.6). In that sense, several efforts to bring multiplexed, integrated LOC for real life applications have been done by industry and research projects, normally, with large multidisciplinary teams. The European Union (EU) for instance, has launched projects under the Horizon 2020 program to tackle real life applications, normally with collaborations across several research groups of different universities and companies with expertise in the area. To name a few, in the BRAAVOO[4] project a team of four research groups and five SMEs companies from seven countries tried to locate biosensors inside a buoy deployed in the ocean to detect the concentration of contaminants in situ.

Thus, a realistic biosensor, should be adapted to the detection requirements: the detection environment, the size of the molecule to be detected, the assay time and reusability requirements, to name a few. In the case of clinical applications for instance, single-use is mandatory, making low-cost a must. Multiplexing is also necessary in order to make precise diagnostics while detecting multiple analytes in a single sample. Depending on the analytes to be detected, normally it is required to sense very low concentrations, making high surface sensitivity a must. In that sense, IO biosensors offer a promising technology for real life LOC biosensors. However, there are many challenges to overcome in terms of both, interferometric biosensors and LOC integration.

1.3.1 Challenges related to interferometric IO biosensors

Depending on the interferometric configuration selected, IO biosensors fabrication can be complex, reaching up to 100 fabrication steps at clean room foundries in some cases. Besides that, the interferometric signal has some ambiguities which can be challenging in the road to a fully integrated LOC IO biosensor. Due to the periodic nature of the interferometric signal, some of the drawbacks are:

4 www.braavoo.org

- **Sensitivity fading.** Since the sensitivity is a function of the rate of change of the effective refractive index over the rate of change of either the refractive index of the bulk or the thickness of the biological thin layer, the sensitivity will vary along with the measurement, becoming maximum at the quadrature points and minimum at the curve extremes. Thus, different responses will be obtained depending in the initial conditions of the detection.
- **Directional and fringe order ambiguity.** Since the intensity fluctuation is also periodic, it is not possible to determine the direction of the phase change from the final intensity value alone. If only one intensity value is measured, any $\Delta\phi_m' = \Delta\phi_m + 2\pi \cdot k$, with k being an integer number, is a similarly possible solution.
- **Relative measurement.** When a complete period of the interferometric signal is not induced by the refractive index change in the sensing area, a reference is required in order to know the fringe period equivalence to a 2π•radians cycle.

1.3.2 Challenges related to integration

LOC systems are challenging in terms of integration. They are made up of several subsystems. It is required a systems architect approach in order to properly tackle all differentcomponents. For example, Figure 1.6 shows an ideal LOC including four BiMW nanointerferometric biosensors and coupling elements. As showed, there are electronic and software systems for the data acquisition, optical system for the sensor excitation and read-out, microfluidic systems for the sample delivery, thermal system for temperature fluctuations compensation, mechanical systems for positioning of the light sources and detectors, multiplexing systems and finally, biological systems for biofunctionalization and biological detection.

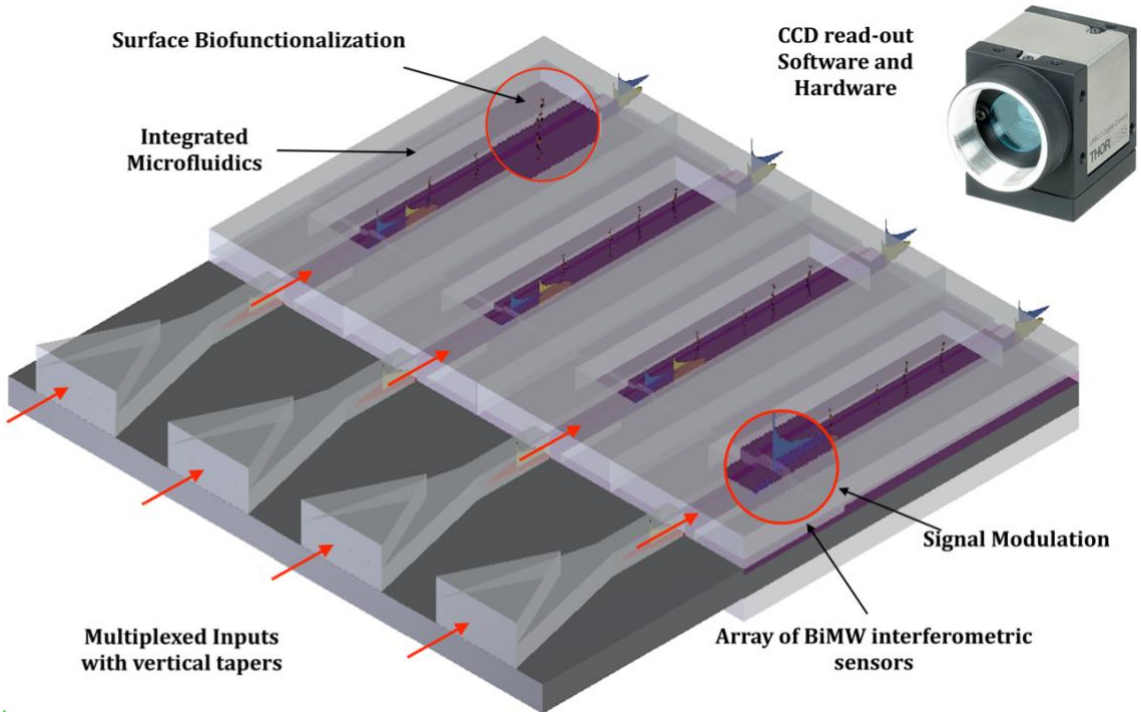

Figure 1.6 Ideal LOC BiMW biosensor systems: optical in-coupling and read-out, modulation system, microfluidics system for sample delivery and surface bionfunctionalization.

The BiMW nanointerferometric biosensor proposed by our group is one of the best candidates for LOC integration due to its simplest fabrication, high sensitivity, and it could be designed to work without expensive setups or bulky equipment. It could provide a multiplexed platform for real time, label-free detection. This is why it has been selected for LOC integration, even knowing the challenges previously discussed. An idealistic design is showed in Figure 1.6. Since the aim of the Thesis is to integrate the BiMW nanointerferometric biosensor into a LOC platform, we should start by understanding what has been done so far and which are the steps which are still to be done. We will begin studying the BiMW nanointerferometer working principle and then defining the tools for its simulation and design.

1.4 BiMW working principle

In order to understand the physics of the Bimodal Waveguide Interferometer biosensor, we start by solving the Maxwell equations in planar dielectric waveguides.

1.4.1 Maxwell's equations in dielectric planar waveguides

Maxwell equations represent the cumber stone of electromagnetic theory. They consist in a set of four equations relating the electric (*E*) and magnetic (*H*) field. For light propagating through a dielectric *($\sigma = 0$)*, non-magnetic *($\mu = \mu 0$)*, isotropic and linear medium *($D = \varepsilon E$)*, the equations become:

$$\nabla \cdot E = 0\,, \qquad (1.10)$$

$$\nabla \cdot H = 0, \qquad (1.11)$$

$$\nabla \times E = -\mu_0 \frac{\partial H}{\partial t}\,, \qquad (1.12)$$

$$\nabla \times H = -\varepsilon_0 n^2 \frac{\partial E}{\partial t}, \qquad (1.13)$$

Equations 1.10 and 1.11 mean that there are no sink or sources of electric or magnetic fields. Equations 1.12 and 1.13 show that for a given electric field varying over time, there is a related magnetic field and vice versa. μ_0 is the free space permeability and ε_0 the permittivity. If the medium is non-homogenous, the refractive index *n* would be position dependent $n = n(r)$.

If the z axis is chosen as the travel direction, the refractive index would vary only in x in a planar waveguide and a set of solutions would exist with the form

$$E(r,t) = E(x)e^{i(\omega t - \beta z)} \qquad (1.14)$$

$$H(r,t) = H(x)e^{i(\omega t - \beta z)} \qquad (1.15)$$

where β is the propagation constant and ω is the angular frequency. A propagation constant β is determined for each one of the guided modes for a given $n(x)$.

There are two possible sets of solutions: the case having all electrical components transverse to the direction of propagation and no electrical component in the propagation direction *z* is called Transverse Electrical (TE) and the case where all magnetic components are transversal to the direction of propagation called Transverse Magnetic (TM). Figure 1.7 shows a scheme of how the electric and field components are related for both modes in a planar waveguide. Analysing Figure 1.7a is possible to realize that $H_y = 0, E_x = 0$ and $E_z = 0$ and the only components are H_x, H_z and E_y for a TE polarization.

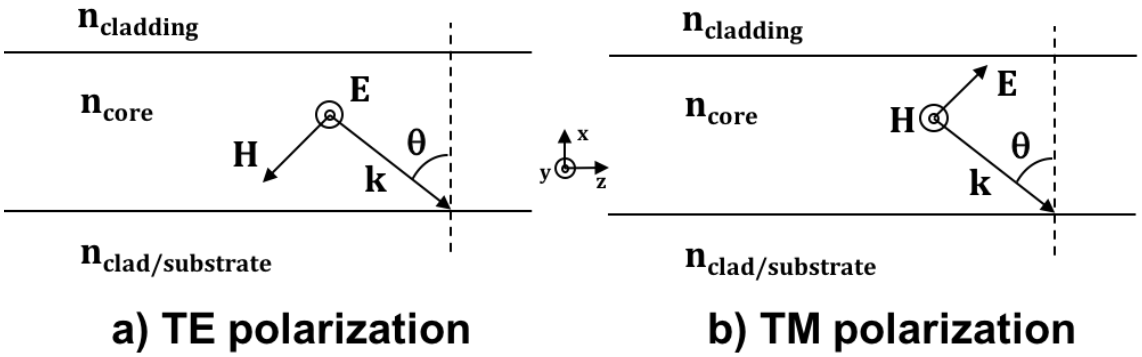

Figure 1.7 Wave vector (*k*), electric (*E*) and magnetic (*H*) components with incident angle θ of a TE (a) and TM (b) polarizations in an asymmetric planar waveguide with core refractive index n_{core} and cladding and substrate refractive index n_{clad} and $n_{substrate}$ respectively.

Substituting equations 2.5 and 2.6 into 2.3 and 2.4, the next set of equations is obtained:

$$H_x = \frac{-\beta E_y}{\mu_0 \omega} \qquad (1.16)$$

$$H_z = \frac{i}{\mu_0 \omega} \frac{\partial E_y}{\partial x} \qquad (1.17)$$

$$\beta i H_x + \frac{\partial H_z}{\partial x} = -i\omega\varepsilon_0 n^2(x) E_y \qquad (1.18)$$

Which lead us to

$$\frac{\partial^2 E_y}{\partial x^2} + E_y[k_0^2 n^2(x) - \beta^2] = 0 \qquad (1.19)$$

Where the value $k_0^2 = \omega^2 \varepsilon_0 \mu_0$ is the square of the wave number $k_0 = 2\pi / \lambda_0$. Equation 1.19 is a second order differential equation and additional conditions would be required in order to solve it. Recalling boundary conditions, the tangential component to the boundary plane H_t and E_t should be constant across both mediums, in this case H_x and H_z which are related to E_y by equations 1.16 and 1.17 constituting a set of three differential equations. Finally, it is worth to remember that the propagation constant β will be related to k_0 by:

$$\beta = k_0 n_{core} \sin\theta \qquad (1.20)$$

where θ is the incident angle. The effective refractive index $N_{eff} = n_{core} sin\theta$ denotes the refractive index encountered by the propagating mode in the z-direction. The mode will be guided as long as it satisfies the condition

$$k_0 n_{clad} < \beta < k_0 n_{core} \quad (1.21)$$

or represented as a function of the effective refractive index:

$$n_{clad} < N_{eff} < n_{core} \quad (1.22)$$

A similar set of equations exist for TM modes. Analysing Figure 1.7(b), it is possible to determine that the only components would be E_x, E_z and H_y, leading to:

$$E_x = \frac{\beta H_y}{\omega \varepsilon_0 n^2(x)} \quad (1.23)$$

$$E_z = \frac{1}{i\omega \varepsilon_0 n^2(x)} \frac{\partial E_y}{\partial x} \quad (1.24)$$

$$\beta i E_x + \frac{\partial E_z}{\partial x} = i\mu_0 \omega H_y \quad (1.25)$$

And substituting equations 1.23 and 1.24 into equation 1.25, leads us to

$$\frac{\partial^2 H_y}{\partial x^2} + H_y[k_0^2 n^2(x) - \beta^2] = 0 \quad (1.26)$$

The set of Helmholtz equations found for TE and TM (equations 1.19 and 1.26 respectively) can be divided in three regions to be solved: the core of the slab waveguide, the top cladding and the bottom cladding (substrate), resulting in three scalar equations to be solved:

$$\frac{\partial^2 E_y}{\partial x^2} - \gamma_{clad}^2 E_y = 0, \; x \geq 0 \quad \textit{(top cladding)}, \quad (1.27)$$

$$\frac{\partial^2 E_y}{\partial x^2} + k_{core}^2 E_y = 0, \; -d < x < 0 \quad \textit{(core)}, \quad (1.28)$$

$$\frac{\partial^2 E_y}{\partial x^2} - \gamma_{subs}^2 E_y = 0, \; -x \leq -d \quad \textit{(bottom cladding)}, \quad (1.29)$$

in the case of TE polarization, where *d* is the thickness of the core layer, k_{core}, γ_{subs} and γ_{clad} represent the transversal propagation constant for the core (k_{core}) and the attenuation coefficients for the cladding regions ($\gamma_{subs}$and γ_{clad}), which are given by:

$$\gamma_{clad} = \sqrt{\beta^2 - k_0^2 n_{clad}^2} \quad (1.30)$$

$$k_{core} = \sqrt{k_0^2 n_{core}^2 - \beta^2} \qquad (1.31)$$

$$\gamma_{subs} = \sqrt{\beta^2 - k_0^2 n_{subs}^2} \qquad (1.32)$$

Solving equations 1.27 to 1.29, the electric field E_y can be expressed as:

$$E_y = \begin{cases} Ae^{-\gamma_{clad}x}, & x \geq 0 \\ Be^{ik_{core}x} + Ce^{-ik_{core}x}, & -d < x < 0 \\ De^{-\gamma_{subs}x}, & x \geq -d \end{cases} \qquad (1.33)$$

The constants *A, B, C, D* and β are solved by matching the continuity E_y and dE_y/dx as boundary conditions at *x = 0* and *x = -d*. A set of four equations with five variables is required to be solved leaving one parameter free (*A* in this case). The expression:

$$k_{core}d = m\pi + arctan\frac{\gamma_{clad}}{k_{core}} + arctan\frac{\gamma_{subs}}{k_{core}} \qquad (1.34)$$

is obtained after solving the set of equations and it represents the eigenvalues of the TE modes. It is considered the *dispersion relation* for the asymmetric planar waveguide and it is a transcendental equation.

Similarly, for TM modes, the eigenvalues equation can be expressed as:

$$k_{core}d = m\pi + arctan\left(\frac{\gamma_{clad}}{k_{core}}\eta_a\right) + arctan\left(\frac{\gamma_{subs}}{k_{core}}\eta_b\right), \qquad (1.35)$$

where $\eta_a = \left(\frac{n_{core}}{n_{clad}}\right)^2$ and $\eta_b = \left(\frac{n_{core}}{n_{subs}}\right)^2$, which are equal to 1 in the case of TE polarization.

Due to the periodic nature of the tangent function, multiple solutions for the propagation constant β will exist depending in the integer number *m* called the *mode order* associated with a unique β_m. The parameters *d, n_{core}, n_{clad}* and *n_{subs}* will determine the admitted solutions and of course, the wavelength λ. In the case of only one admitted solution, the waveguide is called a *single mode* waveguide, and structures admitting more than one mode are named *multimode* waveguides. In the case of non-propagating modes, the structure is said to be in cut-off condition for the working λ. The electric field distribution can be made explicit in the equation 2.24:

$$E_y = \begin{cases} Ae^{-\gamma_{clad}x}, & x \geq 0 \\ A(cos(k_{core}x) - \frac{\gamma_{clad}}{k_{core}}sin(k_{core}x)), & -d < x < 0 \\ A(cos(k_{core}d) + \frac{\gamma_{clad}}{k_{core}}sin(k_{core}d))e^{-\gamma_{clad}(x+d)}, & x \geq -d \end{cases} \qquad (1.36)$$

The electric field shows an exponential decay in the claddings and a sinusoidal dependence in the core. The value A is related to the energy carried by the mode and it represents the field amplitude. The magnetic field components H_x, H_z can be determined by equations 2.7 and 2.8 after determining E_y providing a whole description of the propagating mode. Figure 1.8 shows the first three modes profiles and the fundamental mode TE_0 in an asymmetric waveguide with TE polarization [50]. It is worth to notice the exponential decay in the cladding and substrate of the evanescent wave.

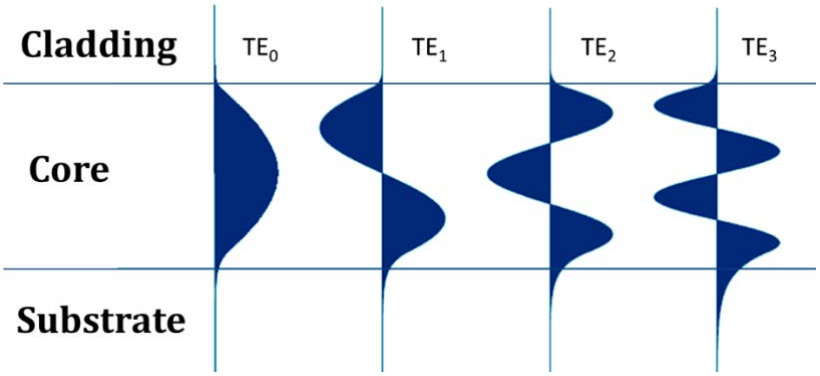

Figure 1.8 Fundamental and first three modes profiles of a TE polarized wave in an asymmetric slab waveguide.

In order to ensure total internal reflection, the reflected wave must have a total phase shift of $2m\pi$ at the boundary of both planes ($x=0$ and $x=d$). The *transverse resonance condition* is given by:

$$2kn_f h\cos\theta - 2\phi_s - 2\phi_c = 2m\pi \qquad (1.37)$$

where m is the mode number, ϕ_c and ϕ_s are the phase shift occurred at the cladding-film and substrate-film boundaries respectively. The *self-consistency equation* can be used in numerical methods simulations for the determination of the N_{eff}:

$$\tan\left(\pi\frac{d}{\lambda}\sin\theta_m - m\frac{\pi}{2}\right) = \sqrt{\left(\frac{\sin^2\bar{\theta}_c}{\sin^2\theta_m} - 1\right)} \qquad (1.38)$$

where d is the slab waveguide thickness, λ is the wavelength, θ_c is the critical angle and θ_m is the bouncing angle of the rays being guided if $\theta_m < \theta_c$ of the m mode. We can then calculate the propagation constant β_m, and finally calculate N_{eff} for different modes. And finally, the penetration depth ξ_e of the E field is given by [49]:

$$\xi_e \equiv \frac{\lambda}{2\pi\sqrt{N_{eff}^2 - n_{clad}^2}} \qquad (1.39)$$

1.4.2 Cut-Off conditions

Depending on the wavelength and the waveguide shape and dimensions, a given set of transverse modes will be allowed to be guided. So, there exist a cut-off condition for each mode for a given waveguide. The cut-off occurs when $Neff \approx n_{subs}$, leading b towards zero. Under this condition, no m mode waves can be guided in the structure. Using geometrical optics approach, the cut off formula for asymmetrical waveguides is given by the next equation for TE:

$$V_c^{TE} = arctan\sqrt{a} + m\pi \qquad (1.40)$$

And similarly, for TM modes:

$$V_c^{TM} = arctan\frac{\sqrt{a}}{\gamma_2} + m\pi \qquad (1.41)$$

In the case of a symmetric waveguide, the cut-off would be given only by the mode index. In the case of the fundamental mode $m = 0$, the $V_{cut\text{-}off}$ is always 0. This means that for a symmetric waveguide, there could always be a wavelength so small or a core thickness so small that at least the fundamental mode can be guided. In that sense, the only cut-off condition for the fundamental mode within a structure is to maintain the symmetry. That means tight restrictions with respect to the values of the refractive indexes of core, cladding and substrate.

1.4.3 Marcatili and the Effective Refractive Index Method (EIM)

Using the Marcatili Method for a slab waveguide, it is possible to calculate the Effective Refractive Index of a rib waveguide by splitting it in three different regions as proposed in Figure 1.9. Region *I* and *II* have similar dimensions (slab width *l*) and refractive indexes. So, the calculated N_{eff1} would be the same for both. Region *II* has a slightly larger slab width due to the rib height increase (h), so the obtained N_{eff2} would be slightly larger than N_{eff1}. Once both effective refractive indexes have been calculated, an equivalent slab waveguide can be analysed having a slab width of W, a cladding and substrate index of $n_c = n_s = N_{eff1}$ and a film index $n_f = N_{eff2}$. However, it is worthy to note that EIM is only reasonably accurate for well guided modes [51].

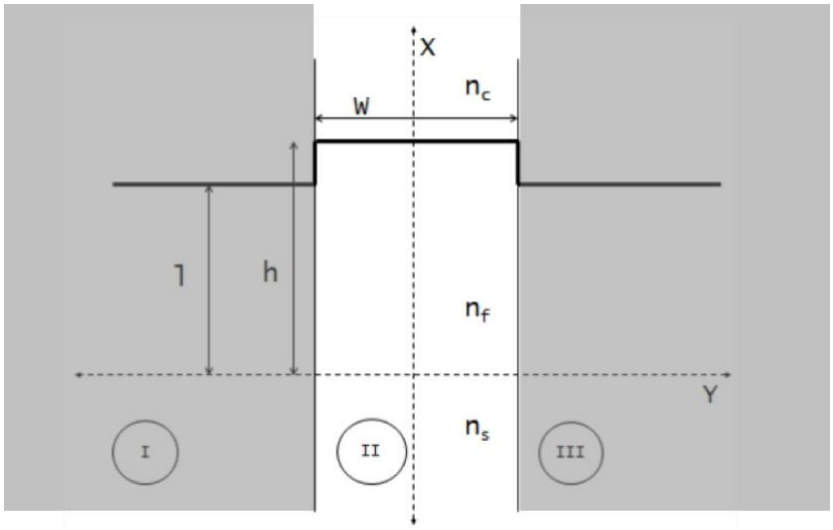

Figure 1.9 Diagram of a rib waveguide. Transmission direction is in the z axis. Using the Marcatili method, it is possible to calculate the N_{eff} of the whole rib waveguide. First, we calculate the N_{eff} using the slab model for regions I, II and III separately. Then, the N_{eff} of a new slab waveguide model is calculated by using region II as core and regions I and III as cladding.

1.4.4 Numerical methods

Scripts in Matlab or Python could be written for quick calculations of the N_{eff} using the Marcatili method. The only required parameters are the wavelength, core thickness, rib height and width, and the refractive index of the substrate, core and cladding. Scripts were made in Matlab and Python to numerically solve the transcendental self-consistency equation as a function of β (equation 1.38) when quick calculations of the N_{eff} were required.

However, for more robust studies in which 3D propagation simulations are required, it is more convenient to use commercial software solutions. In this case, the selected tools are FIMMWAVE and FIMMPROP from *Photon Design*®. It incorporates good CAD designing tools and a large set of numerical methods. Among the most used numerical methods for solving confinement and propagation of optical waves in waveguides, one can mention:

Film Mode Matching (FMM): This is a semi analytical, vectorial waveguide solver based on the film mode matching method (FMM) by Sudbo [52]. Being an analytical method, it is fast and precise when used in structures with long sections of constant refractive index.

Finite Differences Method (FDM): based on Taylor´s theorem, an approximation of the differential equation is implemented. This method is good for solving high step index profiles, curved interfaces and gradient profiles.

Finite Element Mode Solver (FEM): it is a well-known numerical method applied in a wide range of complex problems in physics. By solving small parts that integrate the overall complex problem, a good approximation can be estimated. It is better for solving complex waveguides including their vectorial and anisotropic effects. However, it requires intense processing resources.

Effective Index Method (EIM): it is a well-known numerical method for estimating the N_{eff} in optical waveguides. It calculates the equivalent effective index of a given wave when travelling through a slab waveguide. More details in section 1.4.3

Eigen Mode Expansion (EME): This method is adequate for solving three-dimensional propagation models since it requires less processing power than FDM or FEM. It is the selected method for studying large propagating structures which is the case for the BiMW nanointerferometric devices analyzed in this Thesis. This algorithm is bidirectional by employing scattering matrix (S-matrix) parameters commonly employed in telecommunications in order to join different sections. Moreover, it concatenates the S-matrix of each section to finally obtain a global S-matrix of the device. This way is also possible to describe the overlap of energy between modes when travelling across the different sections.

1.5 Design of the BiMW Biosensor

As explained in section 1.2.2.3, in the BiMW nanointerferometric biosensor, light is coupled and guided into a single mode rib waveguide. Then, after travelling a few millimetres, the core thickness is abruptly increased allowing the guiding of the fundamental and first order mode, TX_{00} and TX_{10}. Both modes keep guided until reaching a sensing area where they will experience different phase shifts respect to the same change of the cladding refractive index (i.e. a detection event). The majority of the analytes for clinical or environmental applications are contained in aqueous solutions as body fluids or water. Thus, it is desired to work in the water spectra absorption window (around 400 to 700 nm) to keep as much energy as possible. The most employed wavelengths are 633 and 660 nm due to the low-cost commercial available solutions (further discussed in section 2.4.3.1).

In terms of materials, certain restrictions must be kept in order to ensure a low-cost biosensing platform yet sensitive: the materials must exhibit a strong index contrast, they should be compatible with standard microelectronics fabrication techniques, the design dimensions should be achievable through photolithographic techniques and they must have low propagation losses. The selected materials are Si_3N_4 (n=2.0) for the core waveguide and SiO_2 (n=1.46) for the substrate and cladding, since they ensure high sensitivities to surface changes and silicon nitrite provides a good confinement of light between 600-700 nm [53]. A rib waveguide has been selected in order to ensure the lateral confinement of light.

Devices dealing with bimodal interference for sensing applications should be able to propagate the fundamental mode that acts as a reference signal and the desired mode that will act as probe in order to create the interfering signal. At the same time, it is necessary to avoid the propagation of any other mode, which would add interference to the system making the readout of the interference pattern more complicated. Each mode propagates with different velocity creating the interference pattern at the exit, which intensity distribution depends on various design parameters: rib height and width, core thickness, wavelength and the refractive index of the selected materials. In case of the BiMW device, TE_{10} is the chosen mode to act as a probe due to the longer penetration of the evanescent tail respect to the fundamental mode TE_{00}. Figure 1.10 shows the cross section of the rib waveguide and the most important variables for its design.

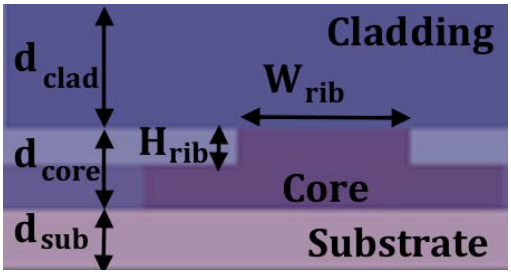

Figure 1.10 Schematic representation of the two-dimensional cross section model of the rib waveguide for the BiMW nanointerferometric biosensor. The core thickness (d_{core}) is different between the single mode section and the bimodal section.

The device is composed of two different core thicknesses: single mode section (SMS) and bimodal section (BMS). Both thicknesses have been previously studied and optimized for sensing, choosing 150 nm thickness for the single mode section and 340 nm for the bimodal section [54]. There is a region in the BMS where the cladding has been etched to work as a sensing window. A model to represent the BiMW nanointerferometric

biosensor has been divided in three different sections: SMS, BMS and BMS with sensing area (BMSsa). This way, it is possible to analyse each section separately and then to execute an overall analysis of the complete device. Recapping, there are the sections:

1. Single Mode Section (SMS). 6500 µm long.
2. Bimodal Section (BMS). 500 µm long.
3. Bimodal Section with sensing area (BMSsa). 15,000 µm long.
4. Bimodal section (BMS). 8,000 µm long.

as showed in Figure 1.11.

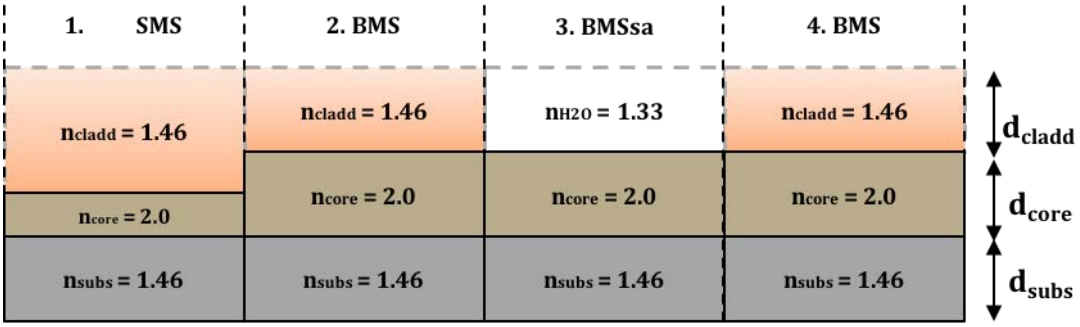

Figure 1.11 Division of the bimodal waveguide interferometer transducer in four sections for propagation studies and simulations. This model is used to simulate the nominal parameters: thickness, rib width and height and sections lengths.

1.5.1 Design parameters

The BiMW device has a dimension of 5 mm long for the single mode section, 5 mm for bimodal section and 15 mm for the bimodal section with sensing window and 5 mm for the final part of a bimodal section. Table 1.2 shows a list of the parameters used for the design and construction of the three different sections in a bimodal waveguide model to be used as a sensing device.

Table 1.2 Parameters used for the simulation of the bimodal waveguide

Section	n_{cladd}	n_{core}	n_{subs}	d_{clad}	d_{core}	d_{sub}	h_{rib}	w_{rib}	length
Single mode	1.46	2.00	1.46	1.5 µm	150 nm	2 µm	1.5 nm	4 µm	6,500 µm
Bimodal	1.46	2.00	1.46	1.5 µm	340 nm	2 µm	1.5 nm	4 µm	500 µm
Bimodal with sensing area	1.46	2.00	1.33	1.5 µm	340 nm	2 µm	1.5 nm	4 µm	15000 µm
Bimodal	1.46	2.00	1.46	1.5 µm	340 nm	2 µm	1.5 nm	4 µm	8000 µm

The EIM has the advantage of requiring less processing power compared to other methods as FEM or FDM. The sweep of the TE/TM fraction from 0 to 100 allow us to find the solutions for TM modes as well (when TE fraction = 0).

On the road towards a fully integration into a LOC system, it is desired to study the coupling coefficients between modes across sections. Besides, we want to investigate what is the influence of the rib size in the confinement of modes? Should we locate the modal splitter or step junction under the silicon dioxide or under the sensing area? Could we have smaller chips without compromising the actual sensitivity?

The current or nominal design parameters of the BiMW nanophotonic biosensor are: core thicknesses of 150 nm for the single mode sections and 340 nm for the bimodal sections and rib height of 1.5 nm and rib width of 4 μm. Even if the BiMW has been probed to work as an excellent biosensor, it has not been yet optimized or characterized for biosensing, neither fully integrated in a LOC system. This device shows bulk sensitivities of ~2000•2π•rad•RIU^{-1} and LODs of the order of ~10^{-7} RIU.

The work of this doctoral Thesis begins at this stage of research trying to answer such questions and at the same time, to drive the integration of the BiMW nanointerferometer biosensor into a LOC platform as far as possible. To do so, we start by modelling the actual BiMW nanointerferometric biosensor to further study the design implications in the biosensing process.

2 MODELLING, FABRICATION AND EXPERIMENTAL SETUPS OF THE BIMW BIOSENSOR.

"All models are wrong but some are useful"

- *George Box*

The BiMW nanointerferometric biosensor has been successfully fabricated and tested for biosensing applications. In order to understand its actual behavior, its sensitivity and its optical characteristics, it is necessary to model it and run simulations.

Simulations will allow us "test" if a smaller design will work as well as the actual device (smaller is cheaper and better integration capabilities) without compromising sensitivity. It will help us to stablish fabrication tolerance limits in a cheaper way (without fabricating). Moreover, it will help us to clarify design questions as where to locate the step junction? What energy is passed to each mode? What are the rib size limits to ensure bimodal behavior? Or what is the smaller biological layer that could be detected by the BiMW? Then, the fabrication process is described and finally, a description of the subsystems for experimental characterization is listed.

2.1 Simulations systems architecture

The self-consistency transcendental equation (eq. 1.38) can be solved using numerical methods either using commercial or self-made software as described in 1.4.4. Furthermore, scripts were made in Python to run simulation studies connecting to *Photon Design* engine through their proprietary Application Program Interface (API). This way, it is easier to design complicated structures via scripts, to modify variables easily (as they are stored in the script itself) and to execute more complex and larger simulation studies in an automated way. The goal is to generate datasets large enough where to look for unexpected tendencies. Figure 2.1 shows a description of the architecture employed to connect the servers to a main data cube (Microsoft® Access Database).

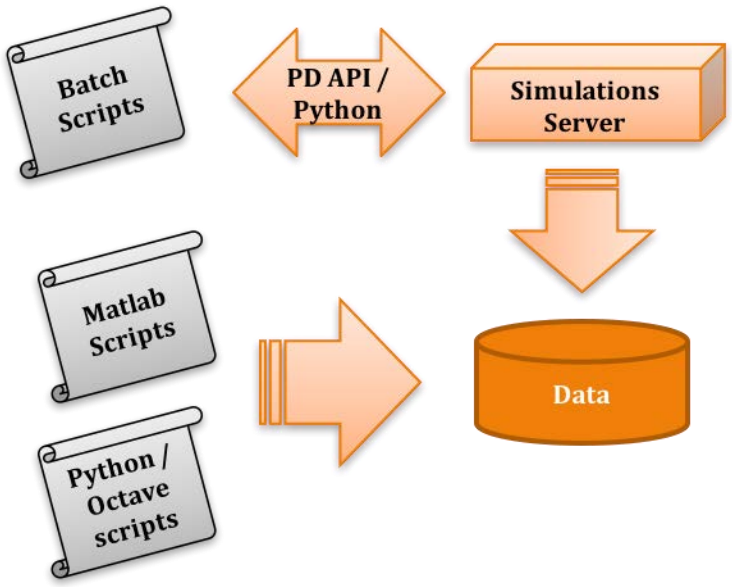

Figure 2.1 Illustration of the simulation system architecture. The *Photon Design Application Programming Interface* (PD API) is accessed using scripts developed in Python to draw the structures and run simulation studies automatically. Data is collected into a central data cube (a Microsoft® Access database – DB) for further analysis. Searches were done with MySQL and results post-processed in Origin®.

Once the simulation system has been implemented following the architecture depicted in Figure 2.1, we start with 2D simulations in order to ensure the confinement of the modes of interest. The 2D model is showed in Figure 1.10. For 3D studies of propagation, the device has been segmented in three different parts as showed in Figure 1.11.

2.2 Simulations of the BiMW nanointerferometric biosensor

Table 2.1 shows the calculated effective refractive index with a λ = 633 nm and 660 nm. The solutions are calculated through the EIM solver in *Photon design*.

Table 2.1 N_{eff} calculated with Photon Design for λ = 633 nm and 660 nm in different sections of the BiMW nanointerferometric biosensor.

λ(nm)	Section	N_{eff} TE_{00}	N_{eff} TE_{10}	N_{eff} TM_{00}	N_{eff} TM_{10}
633	Single Mode	1.725952	-	1.628488	-
633	Bimodal	1.893997	1.588741	1.859086	1.531913
633	Bimodal with SA.	1.890911	1.570647	1.851484	1.4992
660	Single Mode	1.719539	-	-	1.61734
660	Bimodal	1.88776	1.568854	1.849789	1.516863
660	Bimodal with S.A.	1.884375	1.548801	1.841337	1.483695

2.2.1 Modes Profiles

A graphical representation of the simulated guided modes is showed below. Using the design and solver parameter showed in 1.5.1, the mode profiles were plotted simulating a water cladding and a SiO_2 cladding as showed in Figure 2.2 and Figure 2.3 for TE and TM polarizations respectively.

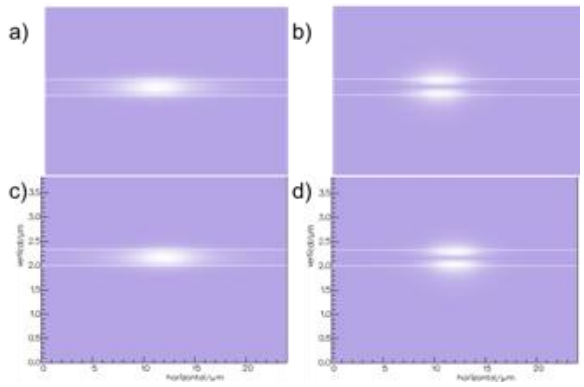

Figure 2.2 Intensity radiation profiles for modes TE_{00} (a) and TE_{10} (b) in the bimodal section covered by SiO_2 and TE_{00}(c) and TE_{10}(d) covered by H_2O.

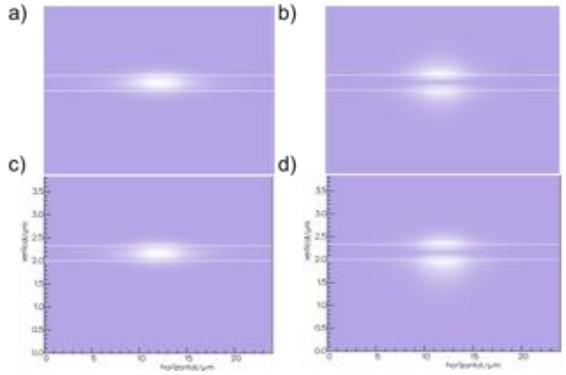

Figure 2.3 Intensity radiation profiles for modes TM_{00} (a) and TM_{10} (b) in the bimodal section covered by SiO_2 and TM_{00}(c) and TM_{10}(d) covered by H_2O.

2.2.2 Cut-off conditions

For a wavelength of 633 nm, core refractive index of 2 and cladding and substrate indexes of 1.46, the cut off thickness would be 233 nm for the first mode (TE_{10}) and 436 nm for the second mode (TE_{20}). Table 2.2 resumes the core thickness values of cut-off for λ = 633 and 660 nm. After running simulations in *photon design* where the core thickness was varied around the cut-off values and the guided and radiated modes manually evaluated, cut-off thicknesses of 233 and 245 nm were calculated for the first order mode

in TE and TM, respectively, with λ = 633 nm; and 243 and 256 nm cut-off thicknesses for TE and TM respectively with λ = 660 nm.

Table 2.2 Cut-off core thicknesses of the first mode obtained with simulations in *Photon Design* for two wavelengths.

Wavelength	λ=633 nm	λ=660 nm
Cut-off TE_{10}	233 nm	243 nm
Cut-off TM_{10}	245 nm	256 nm

2.2.3 Coupling coefficients and propagation

The propagation for TE_{00}, TE_{10} and TE_{01} modes was simulated using the nominal values. Figure 2.4 shows the top and lateral views of the propagation of the modes. Table 2.3 shows the coupling coefficients.

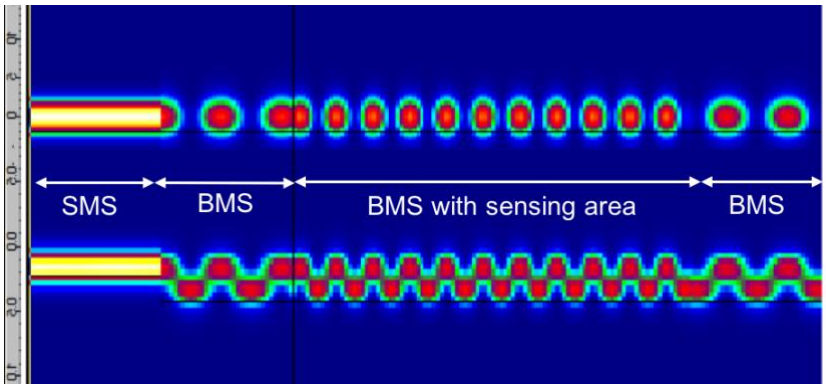

Figure 2.4 Top and lateral view of the simulation of propagation of TE_{00} and TE_{10} modes in the BiMW device with current design parameters and dimensions.

It is worth to mention that the coupling coefficient of the mode TE_{01} is so low (in the order of 10^{-30}) that is considered non-guided (or radiated) mode.

Table 2.3 Coupling coefficients using nominal conditions

Coupling Coeff.	η_{00}	η_{10}
TE	0.69174	0.19474
TM	0.76995	0.11636

With current conditions (listed in Table 1.2), the first order mode is using 19 and 11% of the total input energy in the device, for TE and TM polarizations respectively.

2.2.4 Bulk Sensitivity

The changes of the difference between the effective index of the first and fundamental modes of the device to the changes of the refractive index of the volume above the surface in the sensing area is defined as the bulk sensitivity. The response to a variation of the refractive index from 1.33 to 1.46 was estimated and fitted using a linear and then a polynomial approximation. Results are showed in Table 2.4.

Table 2.4 Sensitivity values for different wavelengths and modes of the bimodal waveguide

Wavelength:	**633 nm**				**660 nm**			
Mode	TE_{00}	TE_{10}	TM_{00}	TM_{10}	TE_{00}	TE_{10}	TM_{00}	TM_{10}
$\delta N/\delta n$ (slope)	0.02347	0.137	0.05776	0.24973	0.02573	0.15185	0.06422	0.25367
$\delta(N_{TX1} - N_{TX0})/\delta n$	TE		TM		TE		TM	
Slope (linear approximation)	0.11363		0.19197		0.12612		0.18945	
Slope (polynomial approximation)	0.21497		0.46641		0.25433		0.5896	

By comparing the sensitivity of modes TX_{00} and TX_{10}, one can observe that the first order mode is one order of magnitude more sensible to changes in the bulk of the sensing window as expected. Additionally, TM polarization is more sensitive than TE cases. The results obtained are in good agreement with previous works in our group.

Recapping, the current dimensions are waveguide ribs of 1.5 nm height by 4 μm width, core thicknesses of 150 nm for single mode sections and 340 nm for bimodal sections, and the step junction is located under silicon oxide. Once the BiMW sensors have been designed, the cut-off conditions studied and the working range defined, it is necessary to design the photolithographic masks in order to fabricate the devices in clean room facilities. All the fabrication reported in this Thesis has been done in the production clean room facilities of the ICTS at the Barcelona Institute of Microelectronics (IMB-CNM-CSIC).

2.3 Fabrication

2.3.1 Modular design of masks for clean-room fabrication

For the lithographic mask designs and its further use in the clean room facilities, the open source library GDSPY[5] and the open source software KLayout[6] was employed. It is an open source library where the developer can build classes to be used in Python scripts. This way, it is possible to use a modular design

5.https://github.com/heitzmann/gdspy
6. http://www.klayout.de

approach to the waveguide design. The current design of the BiMW chips includes two groups of eight waveguide sensors in the lateral sides and one group with four sensors in the middle. Each group includes two single mode waveguides, a bimodal waveguide and a single mode which becomes bimodal waveguide, as references. All of them buried under silicon oxide. A schematic representation of one single chip is showed in Figure 2.5. The whole wafer mask is showed in Figure 2.6.

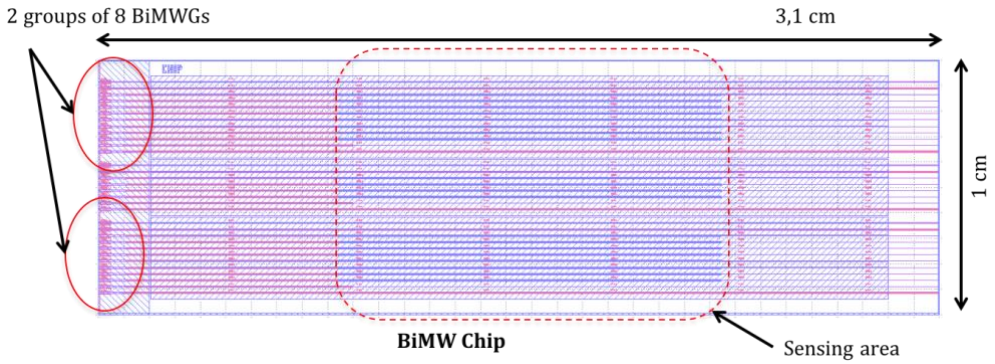

Figure 2.5 Scheme of a BiMW chip including two groups of 8 biosensors and a central group with 4 biosensors.

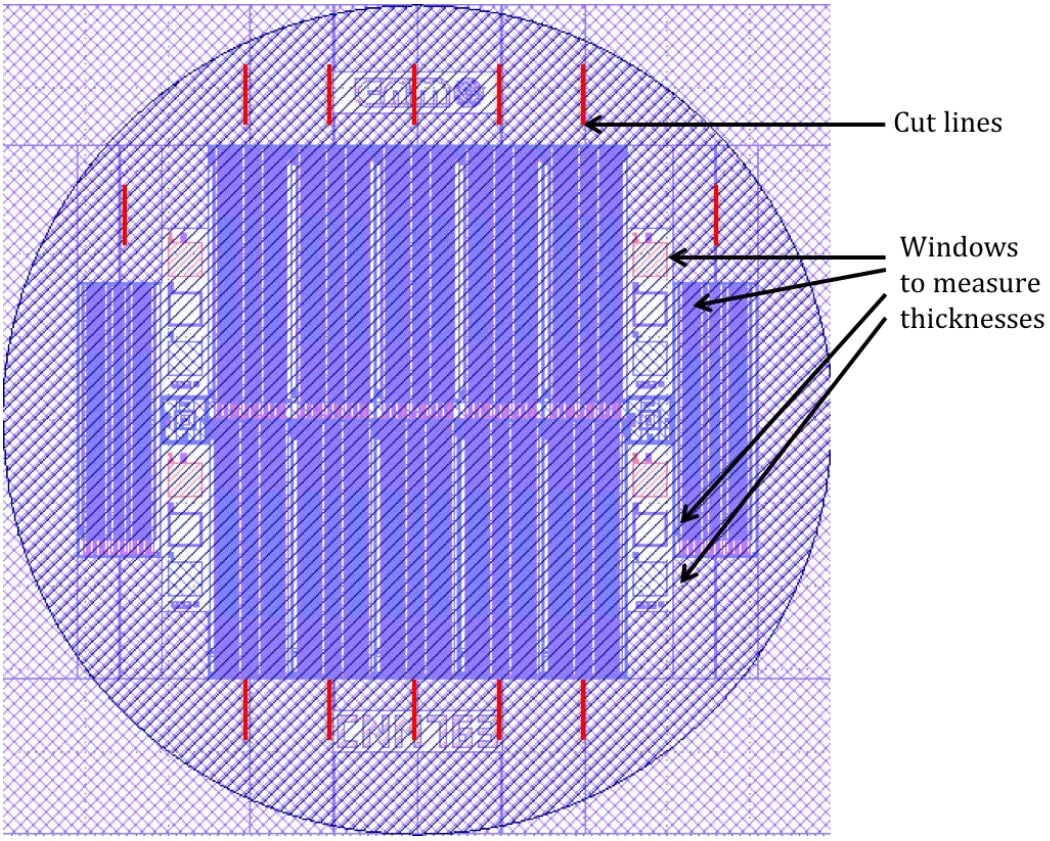

Figure 2.6 Actual design of the BiMW photolithographic wafer mask. It has 12 chips containing 240 sensors in total.

2.3.2 Fabrication steps

Once the BiMW photolithographic masks have been designed, they are fabricated by Photronics Inc. Manufacturing[7] and delivered directly to the clean room facilities. The whole wafer includes up to 12 chips with 20 BiMW nanointerferometric biosensors each one. There are four windows to verify the thickness of the deposited layers through the fabrication process as showed in Figure 2.6.

The fabrication starts with a 2 μm layer of silicon oxide (n = 1.46 at λ = 660 nm) thermally grown over a p-doped silicon 4 inches wafer (Figure 2.7a). Then, 340 nm of silicon nitride (n = 2.0 at λ = 660 nm) is deposited by Low Pressure Chemical Vapor Deposition (LPCVD) since it offers better mechanical stability as compared to other methods (Figure 2.7b). Using the first level of the photolithographic mask made out of Boron Phosphorous Silicon Glass (BPSG, STEP level), the single mode sections are reduced down to 150 nm using hot phosphoric acid as wet etching (Figure 2.7c). After the two modal sections are defined, a nanometric rib structure of 4 μm width and 2 nm height is defined by wet etching with buffered hydrofluoric acid (BHF) using the second photolithographic mask (MZIN level, Figure 2.7d). Then, 100 nm of poly-crystalline silicon (n = 3.9) is deposited over 200 nm of thermally grown silicon oxide, to work as absorbent layer and to avoid cross talking and leaking of light across the plane (Figure 2.7e). The waveguides are opened using the third photolithographic mask by etching of the poly-silicon (META level, Figure 2.7f). Subsequently, a 1.5 μm layer of silicon oxide is deposited by Plasma Enhanced Chemical Vapour Deposition (PECVD) as showed in Figure 2.7g. And finally, the sensing window is opened over the bimodal section by Reactive Ion Etching (RIE) using the fourth photolithographic mask (ASEN level, Figure 2.7h) defining a sensing window of 50 μm width by 15 mm length. Then, a standard photoresist is spin over the wafers in order to provide protection during the dicing process of the chips, which is performed with a diamond saw.

7. http://www.photronics.com/

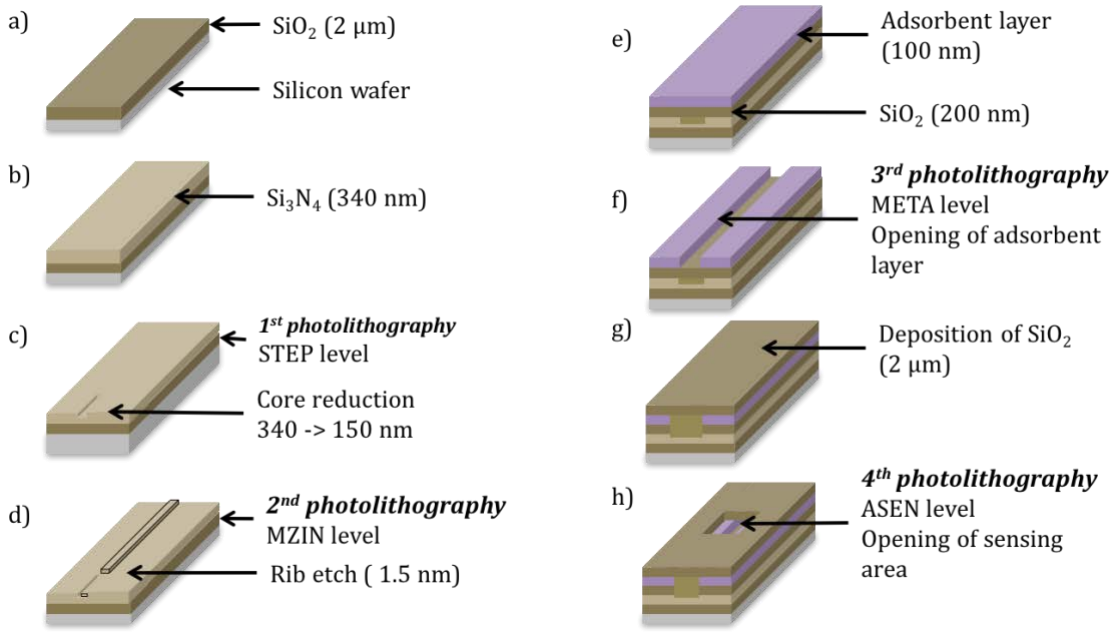

Figure 2.7 Fabrication steps of the BiMW nanointerferometric biosensor.

After individual dicing of the chips, the final dimensions for each of them are 3.1 cm x 1 cm. Each chip includes two lateral groups of 8 BiMW biosensors and a central group of 4 BiMW biosensors. Moreover, each group includes a single mode, a bimodal and a single mode – bimodal reference waveguide in order to verify the guiding conditions of each chip after fabrication.

The wafer with the individualized chips is protected with a standard transparency sheet for its transport and delivery, as showed in Figure 2.8. Before characterization, the chips are cleaned with acetone (Ac, 99.5%, from Panreac, Spain) to remove the protective resin, then rinsed with ethanol (EtOH, 99%, from Panreac, Spain) and finally rinsed with purified milli-Q water (Millipore, USA). A photography of the cleaned chip is showed in Figure 2.9.

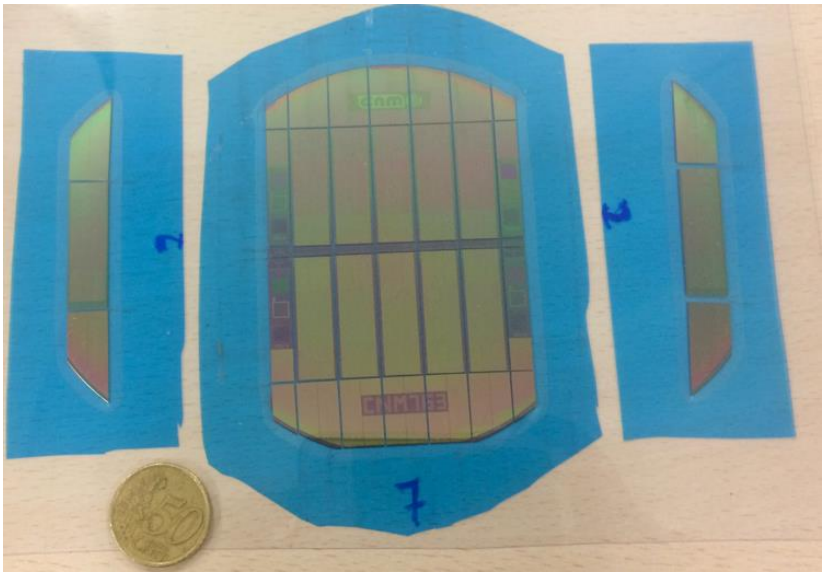

Figure 2.8 Photograph of the fabricated wafer after dicing in clean room facilities. The wafer includes 12 chips with 20 sensors each one.

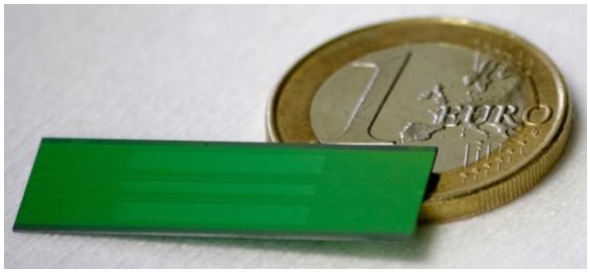

Figure 2.9 Photograph of a BiMW sensor chip after cleaning. Each chip includes three groups of 8, 4 and 8 BiMWs and has a total dimension of 3 x 1 cm.

Polishing with optical quality of the end facets of the chips for appropriate in and out-coupling of the light is required. To do so, we use a lapping machine from Logitech®, model CL50. For correct positioning of the chip facets, a micrometric positioner is used to push a home-made chip holder capable of polish up to three chips simultaneously. The chips are attached using commercial wax in order to facilitate the subsequent detach. They are polished using continuous water flow and a 9 µm grain size paper followed by paper with 3 µm and then 0.3 µm grain size in order to ensure an optical quality and reduce the in-coupling scattering loses. Figure 2.10 and Figure 2.11 show pictures of the holder, polisher and the heating plate.

After polishing, it is necessary to remove the protective photoresist layer and clean any residues of the polishing process. To do so, the chips are sonicated 2 minutes in acetone, and then 2 minutes more with ethanol and water. In order to remove any organic rests, a

solution of HCl:MeOH in 1:1 proportion is employed to sonicate the chips for 2 minutes. Finally, the chips are rinsed with DI water and dried with N_2 flow.

Once the optical quality has been achieved with the polishing process (as observed by naked eye), the chip is ready for characterization.

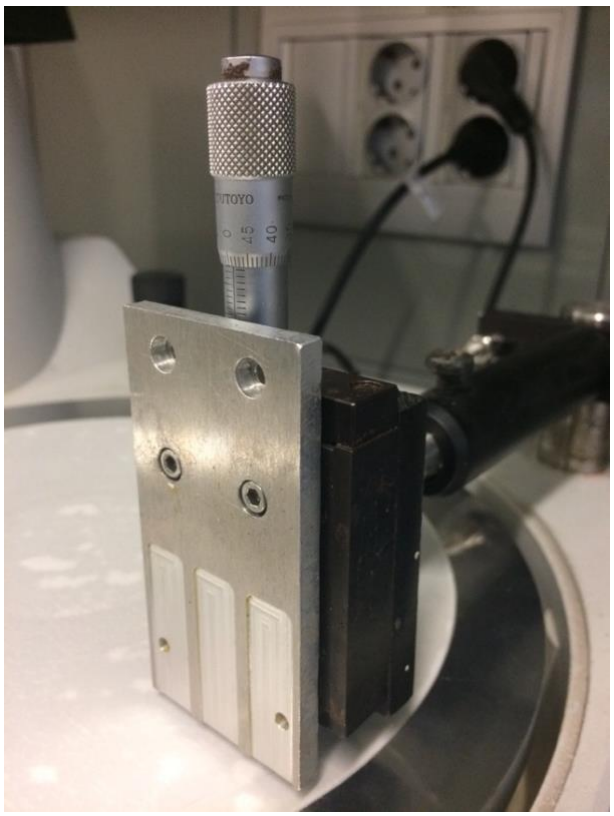

Figure 2.10 Lapping machine CL50 from Logitech with in-house build chip holders. The micrometric positioner helps to apply the appropriate pressure to the chip against the polishing paper continuously.

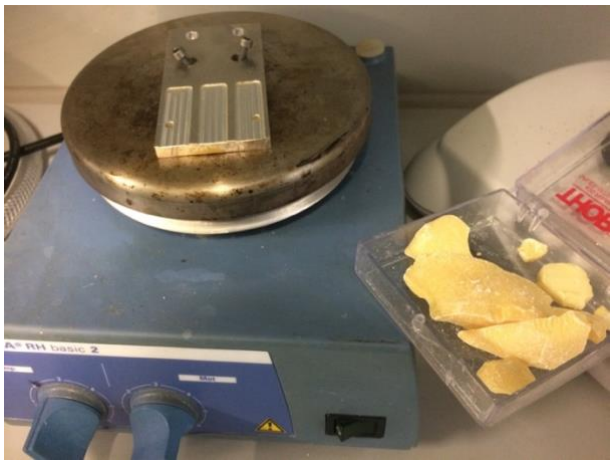

Figure 2.11 Chip holders and wax for polishing. They were heated in a plate at 90ºC, then cooled down for polishing and re-heated for the chip removal.

2.4 Experimental set-ups

The next sub-sections describe each of the systems involved in the experimental evaluation.

2.4.1 Mechanical system

Interferometers are among the most sensitive sensors; thus, its mechanical stabilization is critical to minimize the noise floor during the measurements. Holders were designed in Autodesk ® Inventor Professional Edition and assemblies were performed with the same software in order to validate the integration of the different mechanical pieces (see Figure 2.12 and Figure 2.13). Then, the pieces were 3D printed using a Witbox printer (by BQ[10]) for quick prototyping and correction of possible design mistakes. Once the setup was tested and assembled with the 3D printed pieces, a whole set was fabricated in aluminium using a CNC (Computer Numerical Control) milling machine in our mechanical workshop facilities.

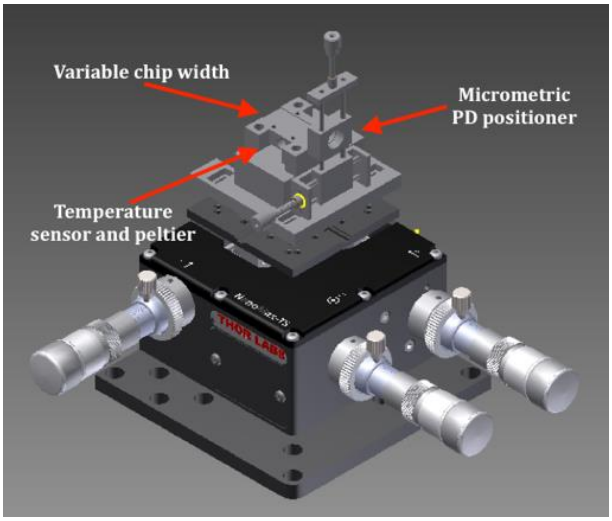

Figure 2.12 Overview of the mechanical assembly of the mechanical holder and photodiode micrometric positioner.

The 3 main modules are the photodiode holder, the chip holder and the radiator piece to be placed into a nanomax 302 stage by Thorlabs®. Some of the critical aspects taken into account were the modular design to allow quick swapping of pieces without requiring disassembling the whole setup. The micrometric positioner includes four magnets (3 mm diameter, 1 mm height, N48 Neodymium nickel-plated by supermagnete[11]) to ensure the exact positioning each time the photodiode was swapped (see Figure 2.13). The adapter piece has a reel to facilitate its displacement over the nanomax stage. The four bores

permit the translation of the whole holder to ensure the posterior coupling of all the BiMWs in each chip. Finally, the chip holder has micrometric indents to keep the chip fixed. It includes bores for the microfluidic cell fixation, a hole for the temperature sensor and a cavity for the peltier installation, which form the temperature control system.

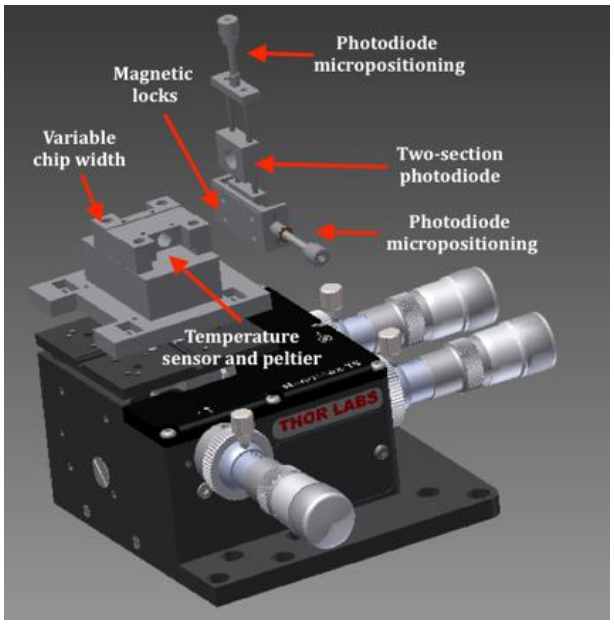

Figure 2.13 Frontal view of the detailed assembly of mechanical holders and micro positioning systems.

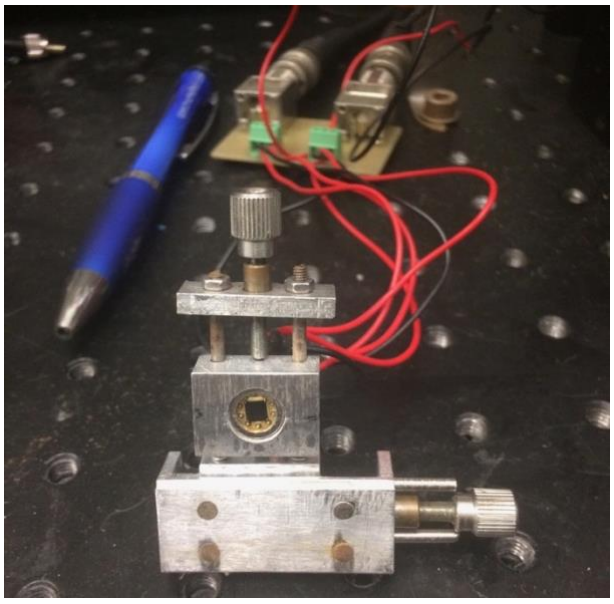

Figure 2.14 Photodiode micro-positioner holder with magnets for automatic placement.

2.4.2 Temperature control system

The BiMW nanointerferometric biosensor is intrinsically sensitive to temperature fluctuations. The temperature of the sensor has to be therefore stabilized and for that we use a thermoelectric cooler (TEC). The temperature controller is a TED200C by Thorlabs® which has an accuracy of 0.1°C and a resolution of 0.01°C by already incorporating a Proportional Integrative Derivative (PID) closed loop control. The reading of the temperature controller only indicates the temperature of the TEC cooler, not the sensor surface temperature, which is also affected by the fluid temperature fluctuations and limited by the thermal conductance of the nitride and oxide layers. The sensor employed is an AD590 by Thorlabs ® with an output current linearly proportional to the absolute temperature, a resolution of 1 μAK^{-1}, a long-term drift of ±0.1º C, a repeatability of ±0.1º C and a calibration error of ±2.5º C at 25° C. The peltier used is a TEC3-2.5 by Thorlabs ® with a measurement accuracy of ±10 mA (out of 10 V) and a resolution of 1 mA. As part of the characterization of the setup, an experiment was run during 4000 minutes and the drift of the setup was measured under stable conditions (between 24.9ºC and 25.1ºC). The results are showed in Figure 2.15. For a 15 minutes injection experiment, the current drift would be $15x10^{-9}$ A corresponding to a $15x10^{-9}$ ºC shift in temperature, which is already well below the 0.1ºC or 0.01ºC values.

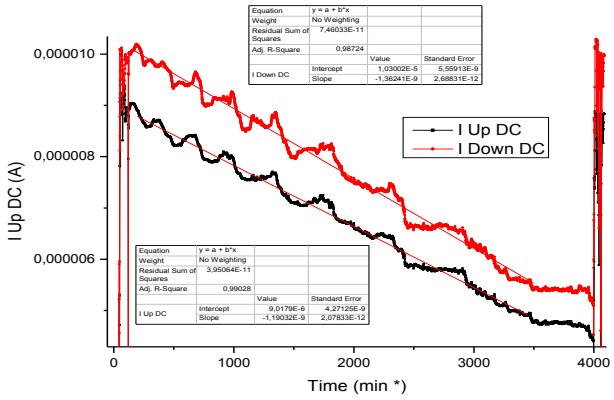

Figure 2.15 Temperature drift evaluated as the photodiode current diminishing during 4000 minutes under stable conditions. Slopes are in the order of 10^{-9} (STD deviation of $2x10^{-12}$).

2.4.3 Optical system

2.4.3.1 Laser sources

Each laser source offers different spectra and light characteristics. The main concerns are the spectra intensity, stability and the feasibility to be incorporated into a LOC system.

The selection of the light source depends upon the experiment requirements. In all cases, the current/TEC controller was a ITC4005 from Thorlabs® (except for the He-Ne lasers). The laser and holders arrangements in the setups have been made in a modular way in order to facilitate the exchange of different laser sources and read-out mechanisms. The variety of sources employed are described below.

2.4.3.1.1 He-Ne Laser

Helium-Neon lasers are appreciated for its narrow spectra, stability and low power. They offer a good solution for characterization at laboratory level but the large resonant cavity makes them bulky and unfeasible for LOC integration. Moreover, due to the nature of the light emission mechanisms, no spectral modulation will be possible. For experiments where a He-Ne laser was required, we have employed a HNL050RB laser (λ = 632.8 nm, P = 5 mW) from Thorlabs®. This is the main laser used for optical characterization experiments.

2.4.3.1.2 Laser Diodes (LD)

Laser diodes have been widely employed in industrial applications since its invention in the decade of the 60s. They offer a more compact laser source as compared to He-Ne lasers. There is a wide variety of wavelengths already available in the market. However, they require thermal and current control systems to provide spectral stability. Nevertheless, this disadvantage can be exploited if a spectral modulation is required [55]. The mount employed in these cases was a TCLDM9 from Thorlabs® allowing a stable operation at 25º C. We have mainly employed the LD ML101J27 from Mitsubishi (λ = 658 nm, P = 120 mW) due to its spectral modulation capabilities further discussed in section 5.2. A typical LD is depicted in Figure 2.16a.

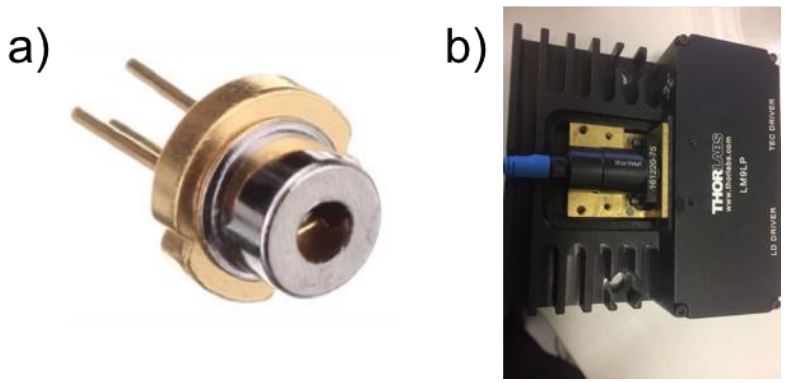

Figure 2.16 Inset a: picture of a ML101J27 FP Laser diode with a metal cavity. It has a central wavelength of 660 nm (operates from 654 to 664 nm) and optical power

of 120 mW. Inset b: photograph of a fibered laser diode LD-642 (λ = 642 nm, P = 20 mW). The output fibre is single mode (SM) with polarization maintaining (PM). The case is an LM9LP with temperature control, all equipment from Thorlabs®.

2.4.3.1.3 Fibered Laser Diodes

Fibered laser diodes offer advantages for assembly in a LOC platform. The light can be guided to the input of the chip without demanding lenses, mirrors, beam splitters or other optical components. There are commercial solutions incorporating single mode fibres in the visible spectra. In our case, we used two main types: LP660-PF60-SP (λ = 660 nm, P = 60 mW, single mode fibre with FC/PC connector) and LP-642-PF20 (λ = 642 nm, P = 20 mW, single mode - polarization maintaining -PM- fibre with FC/PC connector). In the case of the LP660-PF60-SP, a fibre polarization controller (LPVIS050-MP2) was added to the light circuit and a patch cable P1-630PM-FC-2 (λ = 630 nm, PM, Panda style) was incorporated to deliver properly polarized light to the input of the sensor chip. The current and temperature controller employed in all cases is a LM9LP mount for fibre-pigtailed LDs. All the equipment was acquired from Thorlabs®. A photograph of the setup is showed in Figure 2.16b. The spectra of the employed LDs are showed in section 5.2. A picture of a setup with two alternative light sources is depicted in Figure 2.17.

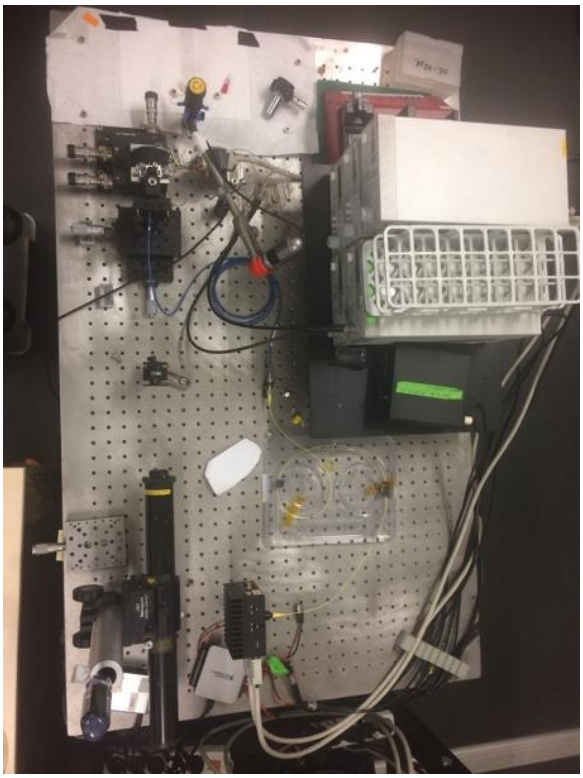

Figure 2.17 Setup with He-Ne and Fibered LD sources.

2.4.3.2 Signal Read-out mechanisms

Once the chip has been excited and it is guiding the light, it is necessary to read-out the light signals at the output of the device. The main concerns are the read-out mechanism sensitivity and its assembly feasibility in a LOC platform.

2.4.3.2.1 Photodiode

Since the output signal S_R of the BiMW is dependent of the intensity difference between the upper and lower part (equation 1.7), a two-section photodiode will be required. The photodiode employed is a S4349 four quadrants (2x2) PD from Hamamatsu® (190 to 1000 nm response range, experimental gain = 4.45 A/W at 660 nm) as we had the availability of many of them in our lab. For using with the BiMW sensor, the two upper quadrants have been wired together to create the upper section, and similarly, the two lower quadrants are wired to form a single lower-section. Figure 2.18 shows a picture of the employed PD and the simulated output of the BiMW nanointerferometric biosensor. The main advantage of the photodiode is its analogue transduction providing better resolution and sensitivity.

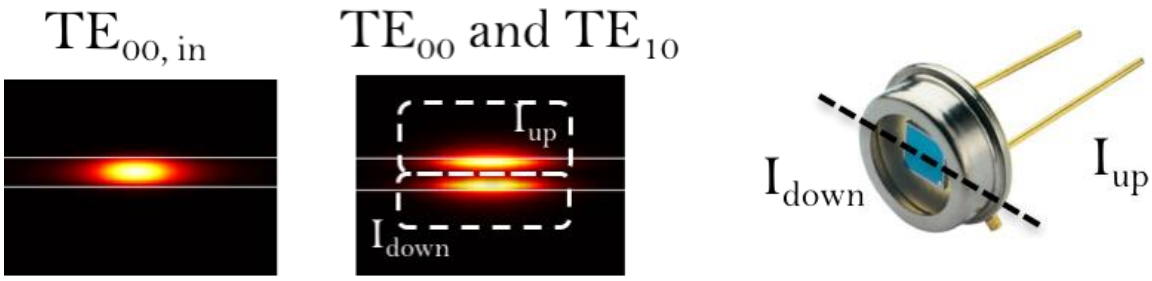

Figure 2.18 Examples of simulated output intensity profiles and the two-section photodiode used for its transduction into an interferometric signal.

2.4.3.2.2 Photodiode arrays

Multiplexing is a mandatory requirement for LOC platforms and it remains as one of the major challenges (see chapter 6). A photodiode array could be employed to simultaneously read-out all the outputs from a BiMW chip. Even if there are commercial photodiode arrays, none of them fit in our two vertical section requirements and maintaining a 250 µm horizontal pitch between sensor waveguides outputs. Custom made solutions are expensive due to the required tailored design and the low-production volume. Moreover, there are not many solutions offered in the visible range.

2.4.3.2.3 CCD

CCDs have become an everyday technology that can be found in multiple appliances: from cameras or optical mousses to telescopes or microscopes to explore the cosmos and the nanoworld. It could be possible to implement a CCD read-out algorithm, as illustrated in Figure 2.19, to create a virtual two-section photodiode by defining regions of interest (ROIs). Several ROIs could be created thus achieving real-time multiplexing.

The selected CCD was the DCU224M – monochrome CCD from Thorlabs® with a sensor resolution of 1280 x 1024 pixels, an exact optical sensor dimension of 7.6 mm (3") and a pixel size of 4.65 µm x 4.65 µm and 8 bits resolution. The software for acquisition and implementation of the CCD detection has been implemented in Labview 2014® and it is further explained in section 2.4.5.

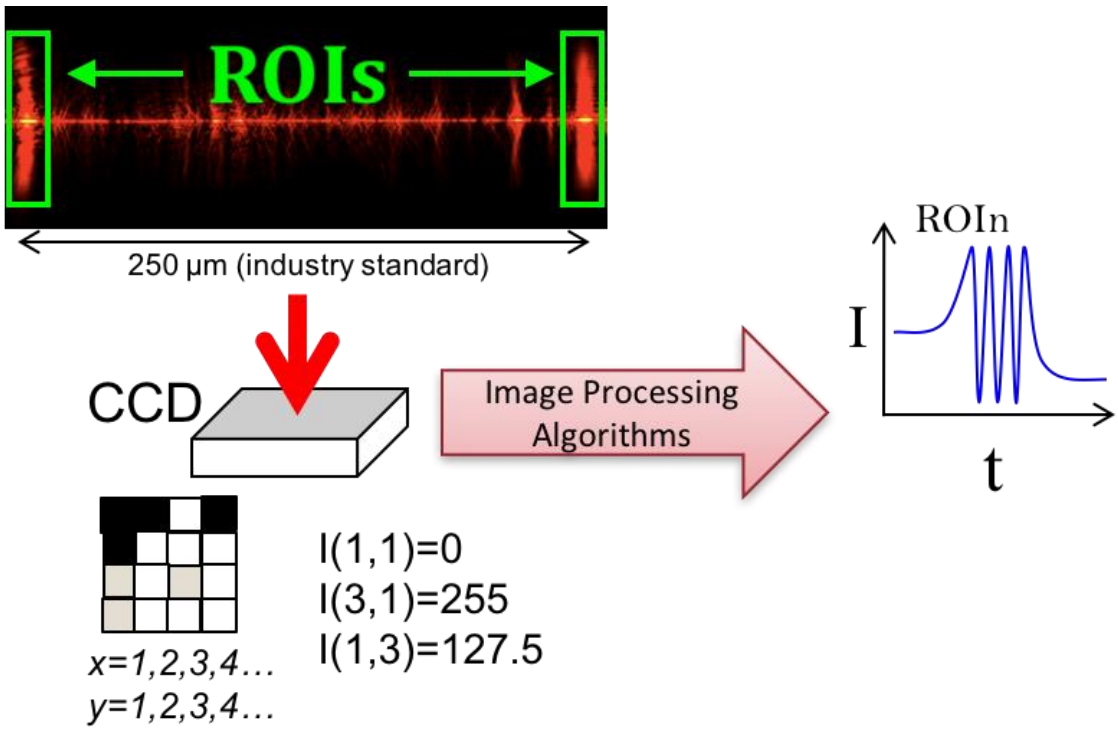

Figure 2.19 Image processing architecture for CCD detection. The CCD sensor has a digital pixel resolution of 8 bits. The algorithm helps to diminish the background noise and construct the interferometric signal for each ROI.

Depending on the experiment requirements, different laser sources and detection methods are selected. Figure 2.20 depicts an example of a setup using a laser diode source, optical components for light collimation, polarization and coupling into the chip (butt coupling

in this case) and CCD read-out after collecting the light with a 40x objective and an intensity filter (ND).

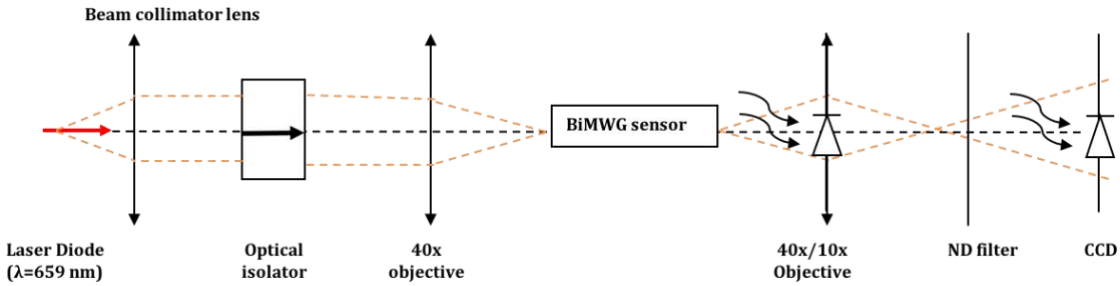

Figure 2.20 Scheme of butt-coupling with laser diode source and BiMW sensor with CCD detection.

2.4.4 Flow cell and microfluidic delivery system

In order to deliver the sample in a controlled manner, a flow cell and a microfluidic circuit must be implemented. The microfluidic circuit consists of an injection pump, an injection valve with a 175 µL sample loop and a waste collection vessel.

The flow cell includes two macro channels of 15 µL volume to cover up to two BiMW biosensor groups on each chip and it is made of Polydimethylsiloxane (PDMS) by polymer casting. The moulds are fabricated using CNC micro-milling machining in our local workshop in Polymethyl Methacrylate (PMMA) blocks. The moulds are then filled with PDMS using a ratio of 10:1 of elastomer and curing agent. Air bubbles are removed by applying a vacuum degasification to the cells by up to 30 minutes. Then, the cell is cured 1 hour at 75º C to ensure the cross-linking of the polymer. After this, the cells are removed of the PMMA mould. In order to reduce the high hydrophobicity of the PDSM channels, a mixture of Polyethylene glycol (PEG200, Sigma-Aldrich) is applied after an ozone plasma treatment to expose functional groups on the polymer surface.

The injection pump is the model NE300 from New Era Pump Systems. PolyTetraFluoroEthylene (PTFE) tubes of 0.5 mm and 0.6 mm of inner and outer diameter respectively are employed to interconnect the pump to the flow cell. The microfluidic valve is a 2-way 6 ports model V-540 from Upchurch Scientific. For connectivity between the tubes and the fluidic cell a 0.5 mm hole was done and the tubes are fixed by pressure of the surrounding PDMS. Figure 2.21 shows a picture of the complete setup including the temperature control, optical components, electronics for data acquisition and the microfluidic system for controlled sample delivering. Figure 2.22

shows a detail of the microfluidic PDMS cell, tube connectors and PMMA cap with end-fire coupling of a BiMW sensor and CCD detection. Further explanation of the improvements and effects of the microfluidic system is discussed in chapter 0.

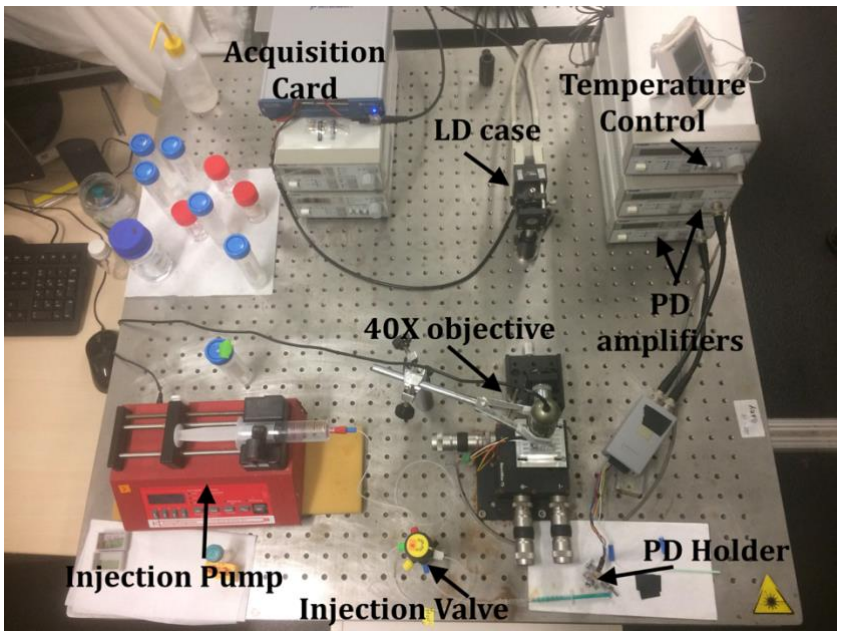

Figure 2.21 Experimental setup including the microfluidic system, temperature control and electronics for data acquisition. The light source is a LD butt-coupled to the BiMW sensor and using PD read-out.

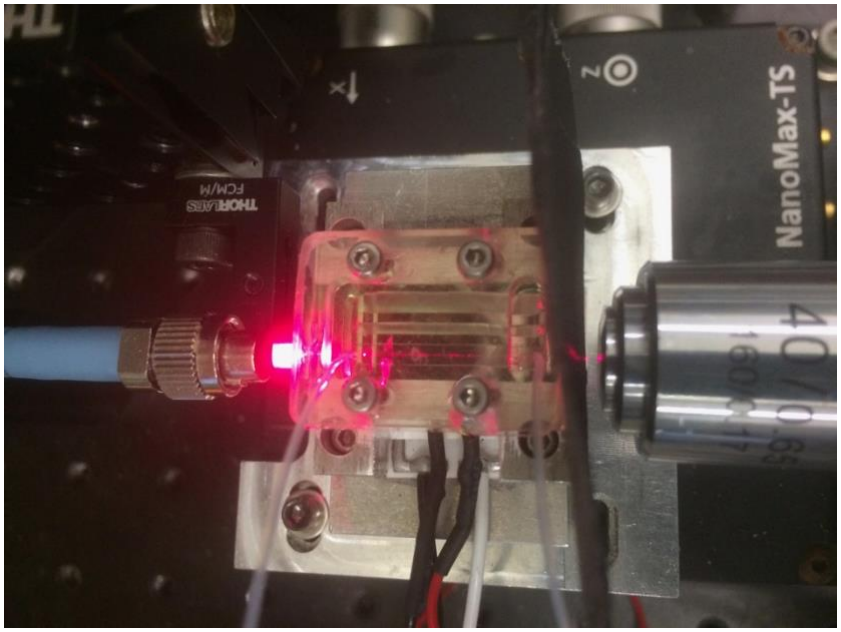

Figure 2.22 Microfluidic cap and tubes connectors. End-fire in-coupling and CCD detection with 40X objective.

2.4.5 Software and data acquisition system

Other important aspect is the software and electronics post-processing of the acquired signal in order to build the sensogram. The definition of the sampling frequency is determined by the velocity of the biochemical reaction taking place in the surface of the biosensor, which is determined by the sample delivering rate of the microfluidic circuit. In our case, the majority of experiments occur in the order of seconds to tens of seconds which is considered a slow process in terms of electronics processing. The main tasks of the software are the laser source control, the data acquisition, the data processing and, finally, the data storage and visualization.

Since several readout methods and laser sources are implemented and each one of them requires different control algorithms, the software has been designed with an Object-Oriented Labview (OOLV) approach and using an *event-driven* systems architecture. With this architecture, the software executes functions depending on events (or *interruptions*). There is a first stage of initialization of variables (previously stored in a XML file), and then an infinite loop is on execution just waiting for events. Upon closing of the software, the configuration changes are saved in the XML file for future opening. When the system is on acquisition mode, two separate loops are executed: one for data acquisition and a second one for data processing (included visualization and storage). The data queue is a FIFO (firs in first out) type ensuring that no data losses occur. This way is possible to have different rates between acquisition and signal modulation of the laser, both processes controlled by the same acquisition card avoiding simultaneous access. Moreover, GIT version control has been implemented during the whole development having up to three development branches and a production branch at the same time. There was a constant communication between the users (other members of the laboratory) and the developers in order to implement their requirements. The GUI consist of two main parts: the left column where the user configures the acquisition by choosing hardware and setting up variables related to it, and the main section where there are four different tabs: the first one is for the data display, the second one for harmonics and post-processing visualization, the third one is the motors tab for the autofocus system configuration and finally the Image Processing tab for CCD multiplexed detection. Figure 2.23 shows a screenshot of the Graphical User Interface (GUI) after implementation of the software and implementing a modulation control of the laser driving current. Figure 2.24 shows a screenshot of the GUI of the fourth tab with multiplexed CCD detection.

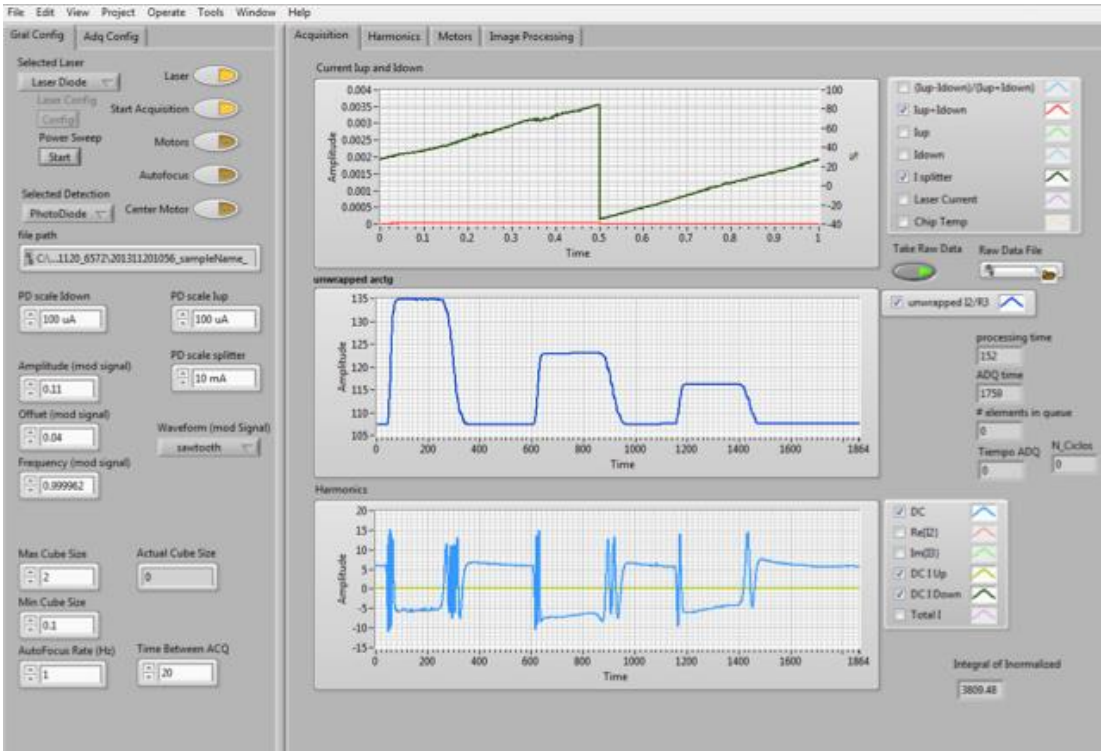

Figure 2.23 Screenshot of the GUI of the software implemented in Labview with OOLV. The upper graph is the driving current of a modulated LD. The middle graph shows the linear readout of three successive injections of different concentrations of HCl and the lower graph the typical interferometric signal without modulation.

Among the functions implemented during the development of this Thesis are the automatic adaptation to different acquisition cards models (all of them from National Instruments – NI); the implementation of LD classes and polymorphic heritage between objects, the simultaneous readout and display, the multiplexed detection while using CCD post-processing, the possibility to choose between RAW information as acquired from the card or the post-processed averaged data, the implementation of laser modulation control system, making possible to situate the PD in the quadrature point (Q point) for sensitivity enhancement (further detailed information in chapter 5).

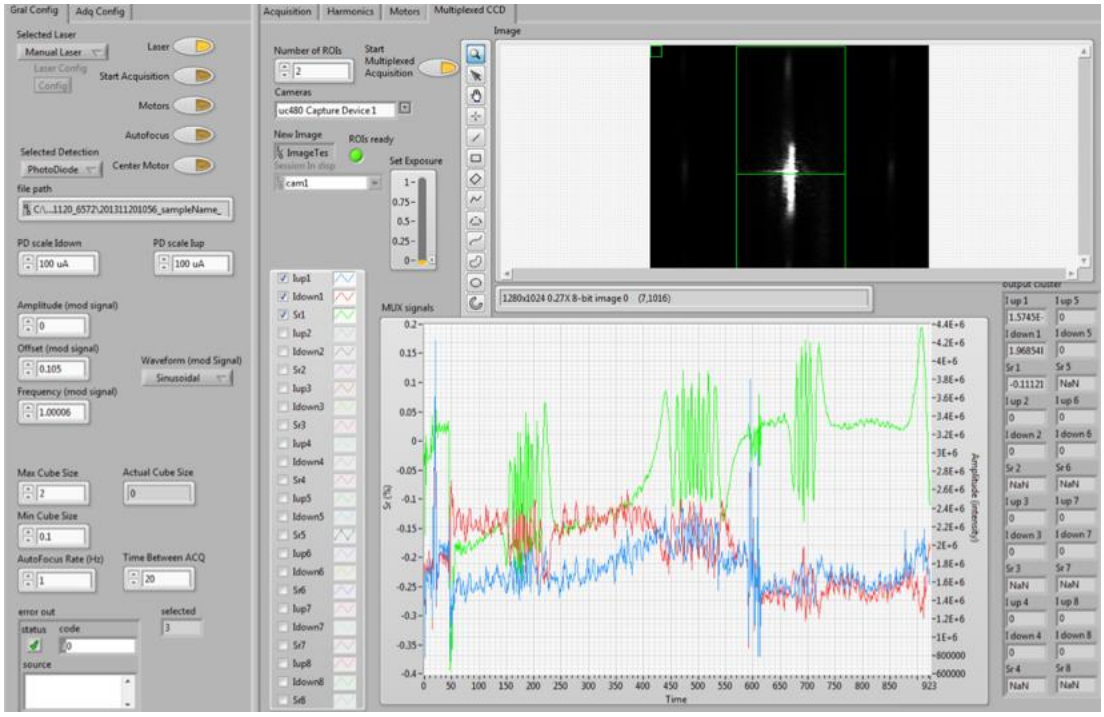

Figure 2.24 Screenshot of the GUI after implementing a multiplexed detection with CCD and multiple ROIs defined by the user.

2.5 Sensitivity evaluation

Two kinds of sensing can be distinguished, each one with its own characteristics: one is the bulk sensing and the other is the surface sensing.

2.5.1 Bulk sensitivity

When sensing in bulk, the changes of phase are caused by a homogeneous change of the refractive index in the whole volume above the sensing surface. This is a non-selective kind of sensing. In case of a bimodal waveguide, the bulk sensitivity S_{bulk} is given by

$$S_{bulk} = \frac{\delta\phi}{\delta n} = 2\pi \frac{L}{\lambda} \frac{\delta(N_{TE10} - N_{TE00})}{\delta n}, \qquad (2.1)$$

where L is the sensor length, λ is the wavelength, N_{TE10} and N_{TE00} are the effective refractive index of the first order and fundamental TE modes, and n is the sensing refractive index.

2.5.2 Surface sensitivity

In the other hand, if the change of the effective refractive index occurs on the core surface in a region smaller than the penetration depth of the evanescent field (equation 2.30 for the cladding region), it is called surface sensitivity S_{surf} and isgiven by

$$S_{surface} = \frac{\delta\phi}{\delta d} = 2\pi \frac{L}{\lambda} \frac{\delta(N_{TE10} - N_{TE00})}{\delta d}, \qquad (2.2)$$

where L is the sensor length, λ is the wavelength, N_{TE10} and N_{TE00} are the effective refractive index of the first order and fundamental TE modes, and n is the sensing refractive index. in the case of Bimodal waveguides.

Once the different systems are ready and setup, it is yet necessary to calibrate the sensor previous to a biosensing characterization. Recapping section 1.2.3 above, it is necessary to distinguish between bulk and surface sensitivity. In this case, the evaluation of the bulk sensitivity intrinsic to each sensor would provide information about the performance of the sensors. Therefore, different concentrations of HCl are successively injected and since each solution has a different refractive index dependent of the HCl concentration, the interferometric phase shift response will be different for each solution (as depicted in insets a to d from Figure 2.25). By plotting the phase shift corresponding to each refractive index change it is possible to calculate the slope of the curve (inset e from Figure 2.25). Such slope is the bulk sensitivity of the device as explained in section 1.2.3. The refractive indexes of all samples are measured with a commercial digital refractometer (Rudolph J57) with up to 5 digits of precision and temperature compensated (at 25 C) and the data is postprocessed either with iPython Notebook or Origin® 8. Furthermore, the LOD, defined as the minimum change of refractive index detectable by the system Δn_{min}, is given by:

$$\Delta n_{min} = LOD = \frac{\Delta\varphi_{min}}{S_{bulk}} = \frac{\Delta S_{R,min}}{S_{bulk}} \frac{\pi}{2V} = \frac{3 \bullet \sigma_{S_R}}{S_{bulk}} \frac{\pi}{2V}, \qquad (2.3)$$

where the phase resolution $\Delta\varphi_{min}$ is evaluated from the measured S_R resolution, ΔS_{Rmin}, which is estimated as three times the standard deviation of the baseline noise σ_{SR}. The factor $\pi/2V$ corresponds to a S_R variation of $2V$ where V is the signal visibility (amplitude) of the S_R when completing a whole cycle, given by:

$$V = \frac{S_{R,MAX} - S_{R,min}}{2}. \qquad (2.4)$$

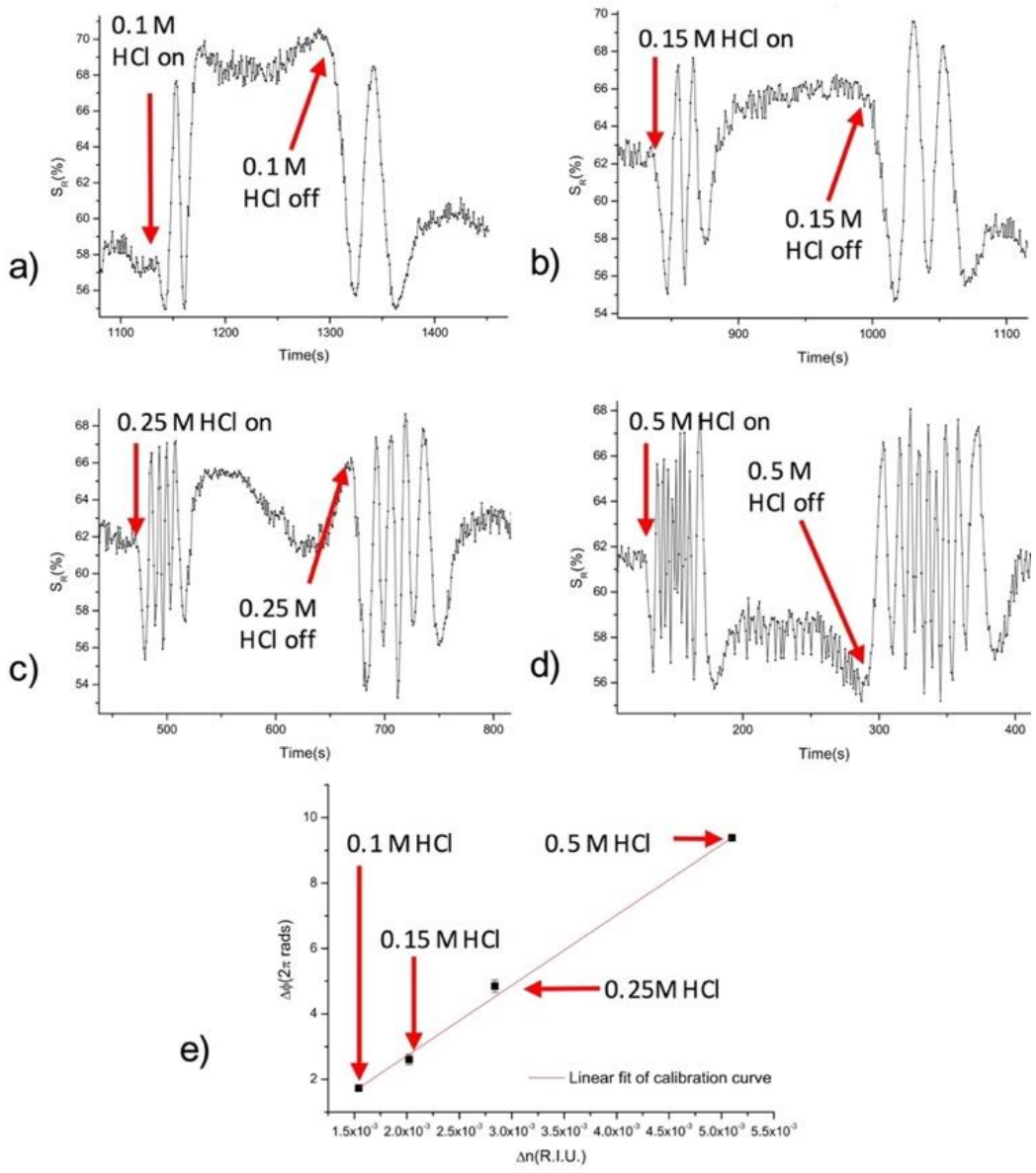

Figure 2.25 Interferometric signals (in %) for injections of different concentrations of HCl: 0.1 M (a), 0.15 M (b), 0.25 M (c) and 0.5 M (d) and a plot of the fitted calibration of a bimodal waveguide sensor (e). The slope (bulk sensitivity) is 4873•π radRIU^{-1} and the limit of detection is 2.72x10^{-7} RIU.

Typical values of S_{bulk} are in the range of ~4000•πrad•RIU^{-1} and typical LODs are in the order of ~10^{-7} RIU.

2.6 Conclusion

The results obtained by simulations performed with FIMMWAVE and FIMMPROP in *Photon Design* show a good agreement with previous studies. Moreover, with the aim to perform larger or more complicated simulation studies a system of python scripts

connected to the *Photon Design* system was developed. Such scripts offer the advantages of faster construction of structures, and the possibility of modifying variables in a simpler way. The system stores the results in a larger database where unexpected tendencies can be further analysed and discovered.

The fabrication has been performed at clean room facilities of the ICTS at the Barcelona Institute of Microelectronics (IMB-CNM-CSIC) following standard microelectronic techniques and using designs with dimensions achievable through photolithographic techniques. Each wafer includes up to 12 chips of 1 cm x 3 cm and each chip includes up to 20 biosensors. After fabrication and dicing the chips are polished to obtain optical quality.

A typical setup for BiMW nanointerferometric biosensor includes several subsystems: mechanical, thermal, optical, microfluidic, hardware and software. As part of the work of this Thesis, several mechanical parts were designed to test different

As showed, the BiMW nanointerferometric biosensor offers one of the most promising candidates for integration into a LOC thanks to its simpler design and fabrication as a straight rib waveguide; yet offering one of the lowest LOD and multiplexed detection capabilities. Moreover, real time detection can be achieved in a label-free manner. However, its integration into a LOC platform is still a challenge to overcome.

Using the proposed simulation tools, the experimental setups, and the clean room fabrication facilities, we propose a set of studies trying to find optimizations that could help in the road towards a full integration into LOC systems. The next chapter will discuss improvements that can help to further integrate the BiMW into a LOC system as well as experimental results for its characterization.

3 BiMW Biosensor Optimizations for LOC Integration

"Without continual growth and progress, such words as improvement, achievement, and success have no meaning."

- *Benjamin Franklin*

This chapter describes the areas of opportunity for improvement and optimization for the BiMW biosensor integration, with the final goal of providing a low-cost, integrated fully portable LOC platform. Each section includes the theory and simulations behind the proposed optimization followed by experimental results and discussion of their suitability

As commented previously, the BiMW interferometric scheme provides one of the most sensitive configuration while allowing a simpler fabrication as compared to other photonic devices. It is of our interest to find areas of opportunity for improvement in the design and fabrication of the BiMW interferometric sensors with the goal to end in a full integrated system but without compromising the excellent device sensitivity. For example, smaller sensor chips would provide more sensor chips per wafer thus, lowering the cost per sensor. The step junction can be located under the silicon oxide or in the sensing window, what would be better in terms of sensitivity? And why? What is the optimal biolayer thickness? What is the influence of the rib size in terms of surface sensitivity? All these questions are addressed in the subsequent sections. We start with rib size optimizations in section 3.1. Then we evaluate the influence of the step junction in section 3.2. The device length is studied and optimized in section 3.3 and then, the biolayer thickness optimization is presented in section 3.4. Section 0 shows improvements to the microfluidic system and finally, the optical characterization of the optimized waveguides is showed in section 3.7.

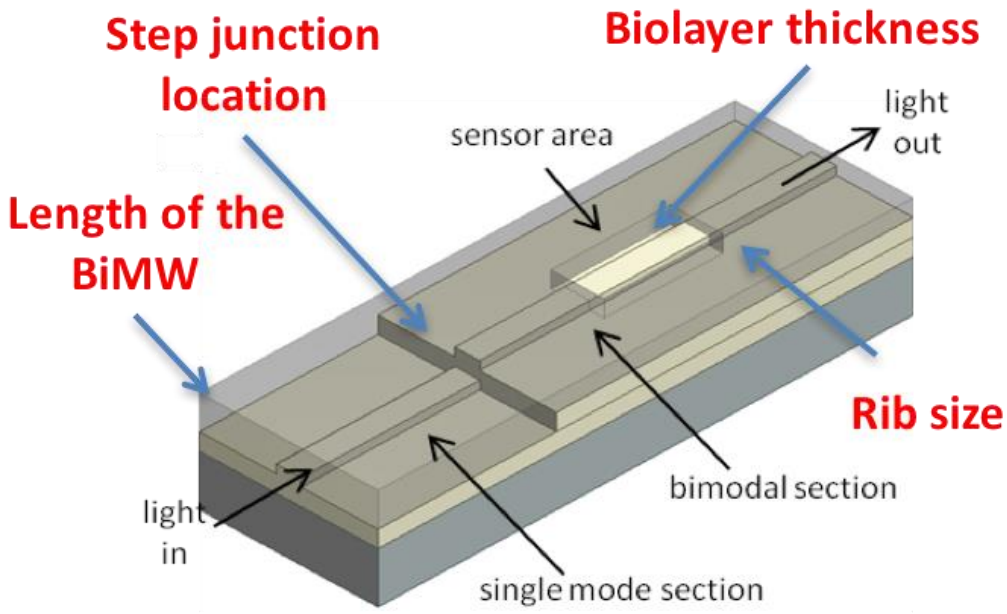

Figure 3.1 Areas of opportunity (*in red*) for improvements of the current design of the BiMW nanointerferometric sensor with the goal of integration towards a LOC system. A new design of the microfluidic cell for sample delivery is also proposed.

3.1 BiMW nanointerferometer rib size optimization for biosensing

The first section of the device is a single mode one designed to filter all other modes. After some distance, this section is coupled into another section, which supports two modes: the fundamental and the first vertical mode (TE_{10}).

Even if single mode conditions have been widely evaluated [53,56], changing the rib size dimensions or the cladding material will lead to different behaviors. The interest of this simulated study is to compare different scenarios where single mode condition must be preserved. Using commercial software *(Photon Design®)* and the EIM, a scan of different rib widths was performed for different rib heights and cladding materials. Firstly, we evaluate the single mode condition for a core thickness of 150 nm having a SiO_2 substrate, Si_3N_4 core and comparing with different materials on the cladding (water and silicon dioxide). Results for different combinations of rib heights and widths are plotted in Figure 3.2.

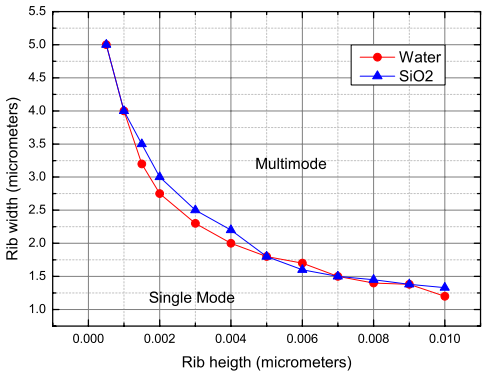

Figure 3.2 Cut-off plot of mode TE_{10} with a core thickness of 150 nm. Comparison of lateral single mode and multimode behavior for different cladding materials.

Moreover, Figure 3.3 shows the effects of the rib height/width combinations on the guided modes for a 340 nm thickness waveguide in both cases: under water and under silicon dioxide. This way, it is possible to define a working region where only the fundamental and the firs order modes will propagate. It is noticeable that a combination of 2 nm height and 4 µm width is just at the border between the working region and the guiding of extra non-desired modes. Thus, fabrication errors could directly impact the correct functioning of the sensors by increasing/decreasing the rib width: if the rib width is 4.2 µm instead of 4 µm, the sensor will not work properly; but if the error yields to a width of 3.8 µm, the sensor will work.

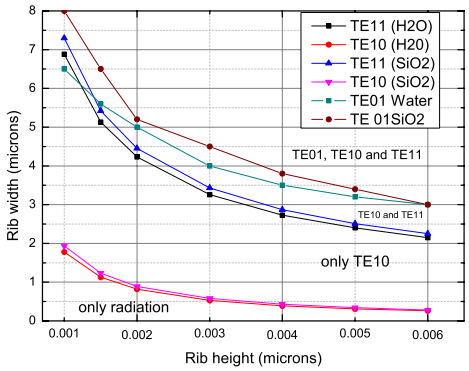

Figure 3.3 Cut-off curves for modes TE_{10}, TE_{01}, TE_{11} with core thickness of 340 nm and different rib combinations and claddings of SiO_2 and H_20.

To ensure that no other modes than TE_{00} and TE_{10} are guided, the cut off plots were obtained for different configurations of rib heights and widths. For example, the cut off plots of modes TE_{00}, TE_{01}, TE_{10} and TE_{11} for a rib of 2 nm are showed in Figure 3.4.

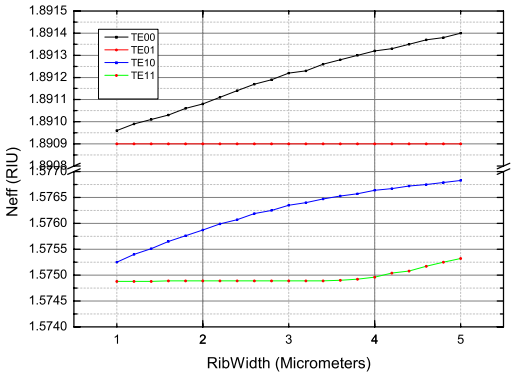

Figure 3.4 Cut off plots of modes TE_{00}, TE_{01}, TE_{10} and TE_{11} for different rib widths. In this example, the core thickness is 340 nm and rib height is 2 nm.

In this example, we can conclude that the mode TE_{10} will not appear when having rib widths of up to 5 microns. However, the mode TE_{11} would appear when having rib widths higher than 4 microns. Moreover, the sensitivity as a function of the rib size variations can be plotted obtaining sensitivities in the order of $2190 \bullet 2\pi radRIU^{-1}$ as showed in Figure 3.5 which are in good agreement with previous studies [54]. The energy coupling efficiency across modes is plotted in Figure 3.6 and seems to be consistent with the previous findings.

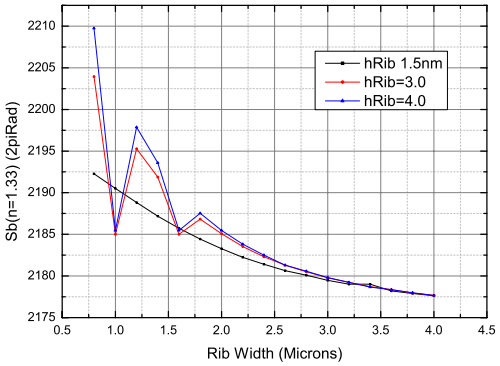

Figure 3.5 Bulk sensitivity of a 340 nm core rib waveguide for different rib sizes. Study made using the EIM.

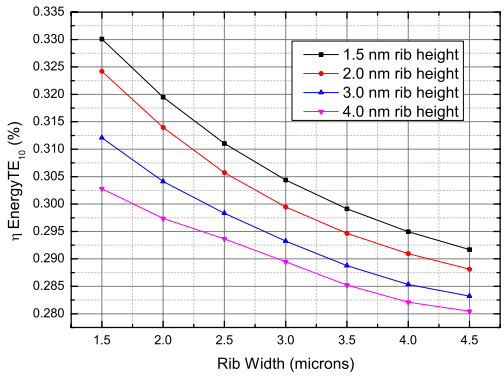

Figure 3.6 Coupling efficiency for intermodal energy distribution.

It is worth to mention that according to simulated results, rib heights of 1.5 nm will require rib widths smaller than 3 µm in order to ensure single mode behavior for all possible materials. Another possible configuration would be a rib height of 2 nm and rib widths below 2.6 µm. With this goal in mind, new sets of the masks used for the second level photolithography were designed as described in section 2.3.1, reducing the rib width to 2.5 µm in one case and 3 µm in another case. Then, two new runs of BiMW chips were fabricated following the process described in section 2.3.2: a wafer with BiMW rib width of 2.5 µm and a second wafer with BiMW rib width of 3 µm.

3.1.1 Experimental evaluation of different rib widths

The rib height is controlled during the etching process step (second photolithography step, see Figure 2.7) obtaining rib heights of 1.5 to 2 nm. The rib width is controlled by the photolithographic mask employed in the same fabrication step. Three different photolithographic masks were designed to allow for the fabrication of rib widths of 2.5 µm, 3 µm and the previous versions of 4 µm. After fabrication, the chips were optically characterized using a CCD as read-out, and morphological characterized using AFM. Figure 3.7 shows the characterization for the 3 µm and 4 µm width waveguides. It is evident that a non-desired transversal mode (TE_{01}) is being propagated in the bimodal section of the waveguide of 4 µm width. As previously discussed, having more than two modes interfering will result in multimodal behavior which is undesired for modal interferometric biosensors. In other hand, the waveguides fabricated using the 2.5 µm rib width masks ended up having a total rib width of 2.8 µm, so finally we decided to use the 3 µm width mask.

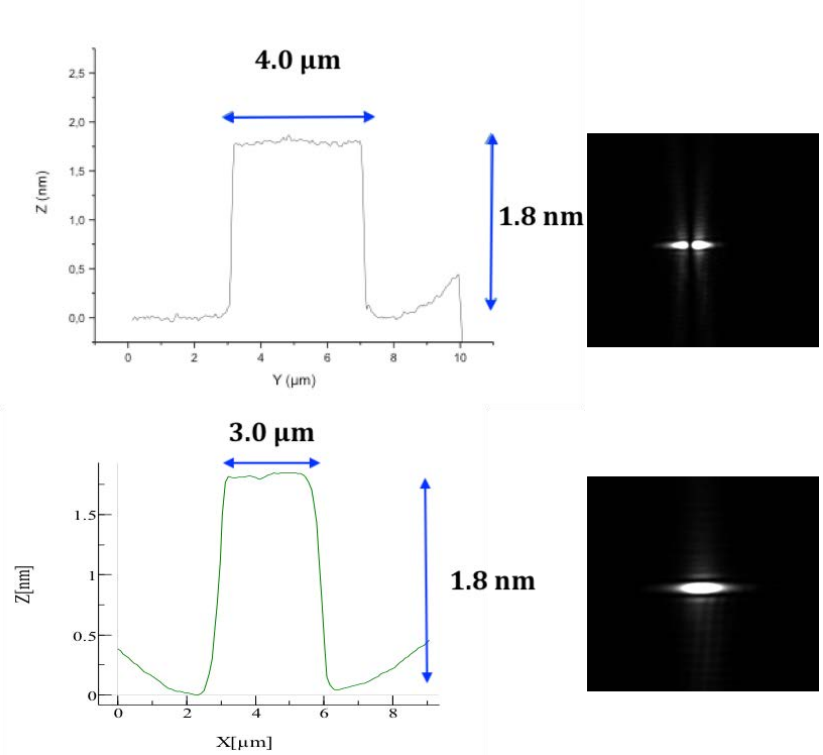

Figure 3.7 Comparison of BiMW sensors fabricated with 4 µm width (upper part) and 3 µm width (lower part). The left side is the AFM morphological characterization and the right side is the light spot as observed at the waveguide output. As discussed, the 4 µm width allows the propagation of non-desired modes, in this case the mode TE_{01}.

3.2 Optimization of the step junction location

The thicknesses of the single-mode and bimodal sections determine how the energy carried by the fundamental mode propagating in the single-mode section is distributed into the two modes propagating in the bimodal section. The energy distribution can be quantified through the coupling coefficients at the step junction. Using the *Photon Design* software, the coupling coefficients are directly obtained from the scattering matrix.

If the device is treated as a black box, the scattering matrix (S matrix) indicates the coupling coefficients for transmittance (left to right and right to left) and reflectance (left to left and right to right) for each one of the possible input modes at left hand side or right hand side of the device, for a given lambda [57]. It is our interest to find the maximum power of the second mode because in this way, it will be possible to increase the visibility, index contrast and thus, sensitivity. There are currently two kinds of chips: the first ones with the bimodal step junction buried under the top cladding and the second group with

the bimodal step junction in the sensing area (approximately 550 µm apart of the beginning of the sensing area) as showed in Figure 3.10.

3.2.1 Modelling and Simulation

The step junction is critical in the guiding and excitation of the first order and the fundamental mode, thus, for the correct generation of the interferometry phenomenon. Moreover, the energy carried by the fundamental mode in the SMS will be distributed between the fundamental and the first order mode in the BMS. The sensitivity should increase as the energy is more evenly distributed across modes. Therefore, it is desirable to study the effect of having the bimodal step junction within the sensing area and compare it to having it under SiO_2. To simulate it, the model previously used in Figure 1.11 is slightly modified to include the step junction under the sensing area. The model is split in four different sections as showed in Figure 3.8:

1. Single Mode Section (SMS). 6,500 µm long.
2. Single Mode Section with sensing area (SMSsa). 550 µm long.
3. Bimodal Section with sensing area (BMSsa). 14,450 µm long.
4. Bimodal Section (BMS). 5000 µm long. 8,500 µm long.

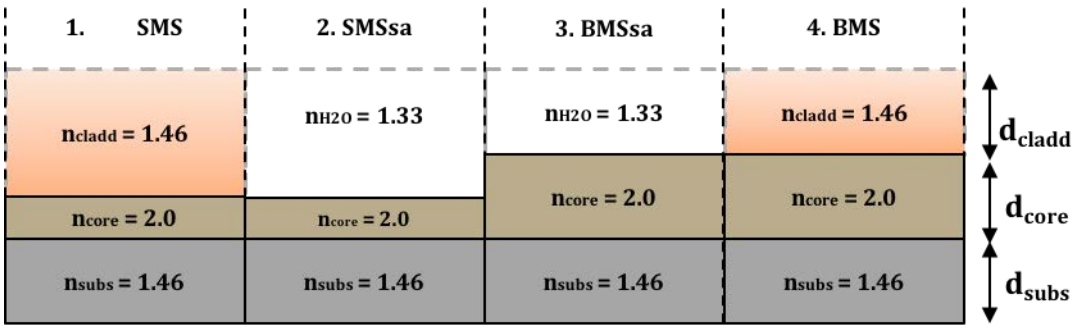

Figure 3.8 Proposed model of a BiMW nanointerferometric biosensor with the step junction located under the sensing area.

The coupling coefficients are 63.94% for TM_{00}, 24.39% for mode TM_{10}, 61.83% for mode TE_{00} and 27.86% for mode TE_{10}. Coupling coefficients are higher for the second mode (TE_{10}) under this configuration due to the lower refractive index of the cladding (1.33 instead of 1.46) which provides a stronger energy confinement.

Table 3.1 Coupling coefficients when the SM-BM step junction is located under the sensing window.

Mode	L_{SMS} (µm)	L_{SMSSA} (µm)	L_{BMSSA} (µm)	L_{BMS} (µm)	η_{00}	η_{10}
TE (nom. L)	6500	550	14450	8550	0.61831	0.27865
TM (nom. L)	6500	550	14450	8550	0.6394	0.2439

Figure 3.9 shows the propagation of TE modes in a sensor waveguide when the single mode-bimodal step junction is located under the sensing window.

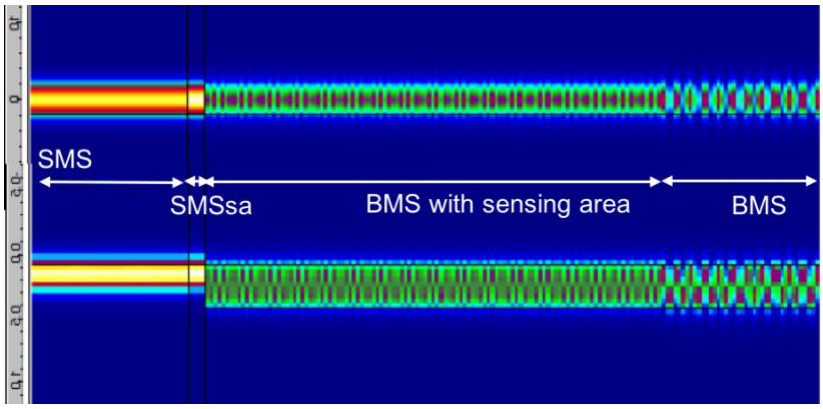

Figure 3.9 Top and lateral view of the propagation of TE_{00} and TE_{10} modes when the single mode – bimodal step junction is located under the sensing window.

Another advantage of having the step junction under the sensing window besides the increment in the coupling coefficient is the fact that a more homogeneous distribution of the E_y field will be obtained over the entire surface of the rib, in contrast with the field distribution when the step junction is buried under the SiO_2 cladding. Such distribution can be due to a reflectance effect similar to the ones observed in microwave waveguides or conducting lines. In our case, a more homogeneous distribution will increase the possibilities of detection changes in the sensing area, and consequently, a better sensing device. For further details please refer to appendix A.

3.2.2 Fabrication and experimental evaluation

Following the standard fabrication process as depicted in section 2.3.2, six different groups of BiMW sensors are contained within the same chips. The first three groups of 8 BiMW sensors included a bimodal step junction located under the SiO_2 (upper part in Figure 3.10) and the next three groups of 8 BiMW sensors included a bimodal step junction located at 550 µm away from the sensing area (lower part of Figure 3.10). The optical characterization was performed coupling by end-fire the light from a HeNe laser with a wavelength of 632.8 nm, with TE polarization. The PD gain was experimentally

calculated to be G = 0.446 AW^{-1} at 630 nm (described in page 41). The bulk calibrations were performed as described in section 2.5.

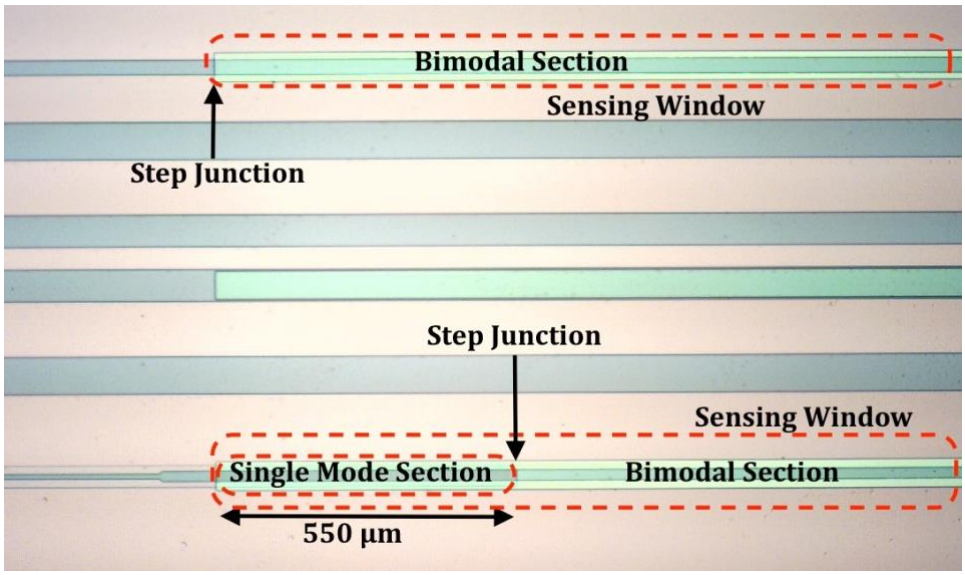

Figure 3.10 Photography of the fabricated chips comparing BiMW sensors with the step junction located under silicon oxide (upper part) and located 550 µm under the sensing area (lower part).

Table 3.2 shows the comparison of the optical power read at the output of the sensor and bulk calibrations performed in similar conditions. As expected, the BiMW sensors having a step junction located 550 µm under the sensing area were capable of confining more light (up to 4 times more output optical power), thus increasing the visibility and achieving better and more consistent LODs.

Table 3.2 Comparison of sensing calibrations, sensitivities, limits of detection and output power between BiMW sensors with the step junction located under silicon oxide (sensors 1.2, 2.2 and 2.3) and under the sensing area (4.2, 4.3, 5.2 and 5.3).

BiMW sensor	I_{up} [µA]	I_{down} [µA]	Slope [2πrad]	Visibility [%]	LOD [RIU][a]	Step junction cladding	Power [µW]
1.2	1.1	0.5	1777	69.7	$1.14X10^{-6}$	SiO2	3.58
2.2	0.5	0.8	1713	88	$6.96\ X10^{-7}$	SiO2	2.91
2.3	2.6	1.4	1668	83	$4.97\ X10^{-7}$	SiO2	8.96
4.2	3.7	3.7	1661	110	$3.7\ X10^{-7}$	H2O	16.59
4.3	5.3	2.1	1667	112	$4.24\ X10^{-7}$	H2O	16.59
5.2	1.6	4.3	1616	118	$5.94\ X10^{-7}$	H2O	13.22
5.3	1.7	2.5	1638	114	$3.27\ X10^{-7}$	H2O	9.41

[a] Refractive Index Units

3.2.3 Conclusion

It has been previously simulated in section 2.2.3, that a 19.47% of energy coupling will be transferred to the second order mode and 69.17% to the fundamental mode in the BiMW nanointerferometric biosensor when the step junction is located right at the beginning of the sensing area (i.e. under SiO_2, n = 1.46) as modelled in Figure 1.11. In the other hand, when placing the step junction 550 μm into the sensing area (i.e. under H_2O, n = 1.33) there will be a 27.83% of energy coupling to the first order mode and 61.83% to the fundamental mode. A more homogeneous distribution of the modal power will be translated into a higher sensitivity. This has been experimentally demonstrated when characterizing two groups of BiMW sensors within the same chips and comparing its total output power and sensitivities. Therefore, since now on, we will adopt this change in the design of the BiMW sensor technology for all future fabrications.

3.3 Total length optimization

It is desirable to know the influence of the dimensions of the BiMW in the sensitivity in order to know the effect of reducing the size of the device while maintaining the coupling coefficient and the losses, in order to provide with a more compact device for a lab-on-chip integration. This reduction will also contribute to decrease the cost of the fabrication at clean room facilities, as more sensors could be allocated in the same wafer size.

3.3.1 Simulation

Firstly, it is desirable to simulate the nominal conditions of the actual dimensions of the bimodal waveguide sensor. Simulations were done using the EIM in *Photon Design*. Photon Design includes an optimization tool called Kallistos, which can sweep different variables and find the best set for a given parameter. In our case, the S matrix with the coupling coefficients for each mode is analyzed looking for the largest total forward power or the largest power of mode 0 or 1, or maximization of the total power within the device.

Transferring more power to the first mode (TX_{10}) will increase the difference between the effective indexes of the fundamental mode and the first mode, thus increasing the sensitivity of the device.

The only conditions are:

1. To keep the sensing area as large as it is now to avoid any worsening of the LOD due to the reduction of the length (due to the interferometric nature of the device, sensitivity increases with the interaction length), and
2. try to compare the effects of reducing the length size of different sections.

A Kallistos optimizer has been run in order to find the appropriate dimensions that could provide a good trade between coupled energy from the first mode and the device dimensions. Appendix A shows the coupling coefficients and radiation patterns for different lengths and modes, simulated with a wavelength of 633 and 660 nm, respectively. Table 3.3 shows the simulated modal coupling efficiencies from the fundamental TE or TM mode (first column) to the fundamental (η_{00}) and first order mode (η_{10}) when having different section lengths. The original BiMW has a dimension of 6500 μm in the SMS, then 550 μm for SMSsa, 14450 μm for BMSsa and finally 8550 for the BMS at the output and the fundamental mode from the SMS distributes 61.83% of its energy to the fundamental mode and 27.86% to the first order mode in the BMSsa. These are the nominal conditions. Then, optimizations were run looking for shorter lengths where the modal coupling energy could be improved, obtaining a maximum of 61.67% to the fundamental and 28.05% for the first order TE modes when having lengths of 186.5 μm for SMS, 2500.5 μm for SMSsa, 8611.5 μm for the BMSsa and 186.17 μm for the BMS. These are values impractical for fabrication giving the required precision, but they are a good approach for determining the maximum theoretical achievable. A more realistic approach could include SMS of 1029 μm and BMS at the output of 655 μm, obtaining coupling coefficients slightly higher than the nominal ones (61.83% to the fundamental and 27.86% to the first order mode). Moreover, a larger BMSsa (15000 μm instead of 14450 μm) was simulated slightly increasing the coupling coefficient of the fundamental mode to 62.77% but lowering the first order mode to 26.83%. Finally, the simulation of a sensor with lengths of 1029 μm for SMS, 550 μm for SMSsa, 14450 μm for BMSsa and 655 μm for the BMS of the output shows an increase of the coupling coefficient for TE_{10} mode to 27.86% and keeping 61.83% for the fundamental mode. The same device will have a coupling coefficient of 63.94% for mode TM_{00} and 24.39% for TM_{10}. These are the last two rows from Table 3.3 which are a fine trading between device dimensions and energy coupled to the first mode in both, TE and TM polarizations. Figure 3.11 shows the propagation intensity across the device with these dimensions.

Table 3.3 Coupling coefficients when the SM-BM step junction is located under the sensing window and comparing different lengths in the SMS and BMS.

Mode	L_{SMS} (µm)	L_{SMSSA} (µm)	L_{BMSSA} (µm)	L_{BMS} (µm)	η_{00}	η_{10}
TE_{00}	186.17	2500.5	8611.5	186.17	0.6167	0.2805
TM_{00}	186.17	2500.5	8611.5	186.17	0.6863	0.1913
TE_{00} (nom. L)	6500	550	14450	8550	0.61831	0.27865
TM_{00} (nom. L)	6500	550	14450	8550	0.6394	0.2439
TE_{00}	1029	550	15000	655	0.6277	0.26832
TM_{00}	1029	550	15000	655	0.6294	0.2550
TE_{00}	1029	550	14450	655	0.6183	0.2786
TM_{00}	1029	550	14450	655	0.6394	0.2439

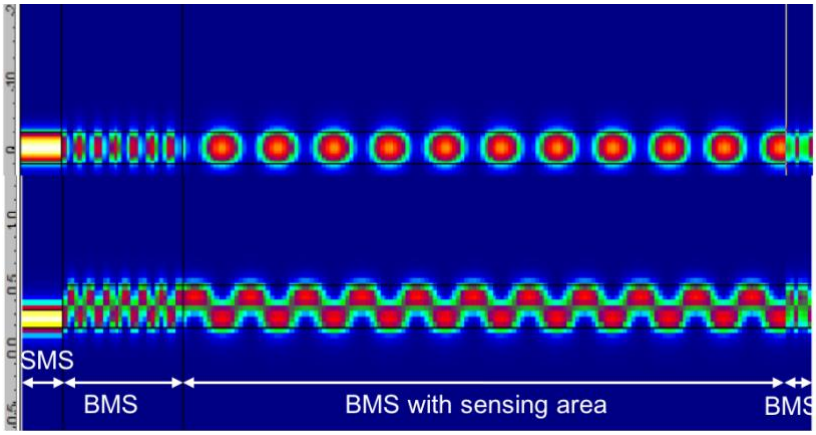

Figure 3.11 Top and lateral view of the propagation of TE_{00} and TE_{10} modes in the optimized device with shorter dimensions.

Based in the simulated results, it is clear that the modal energy coupling coefficients would not be significantly affected by changes in the length of the device. Thus, it can be suggested that the sensitivity would not be affected by length reductions. Moreover, smaller chips would help to reduce the fabrication cost per chip and finally per diagnostic.

3.3.2 Experimental evaluation

To experimentally compare the implications of a shorter BiMW sensor, a chip with the standard dimensions and its shorter version were calibrated. For that, the standard chip with length of 31 mm was calibrated injecting three times the HCl solutions as explained in section 2.5. The slope of the curve (bulk sensitivity) was estimated to be 4873•πradsRIU-1, a visibility of 29.86%, and a LOD estimated of 2.72×10^{-7} RIU, as plotted in Figure 3.13.

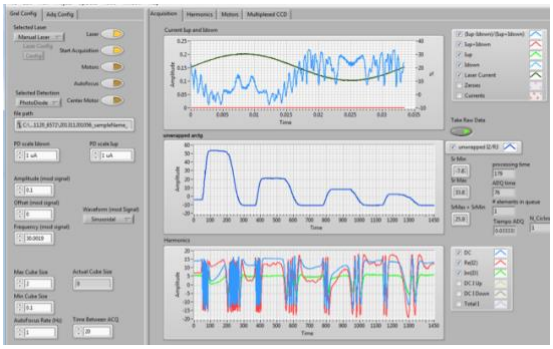

Figure 3.12 Bulk calibration of a standard sensor chip by injecting successive solutions of HCl with concentrations of 0.5, 0.25, 0.15 and 0.10 M HCl.

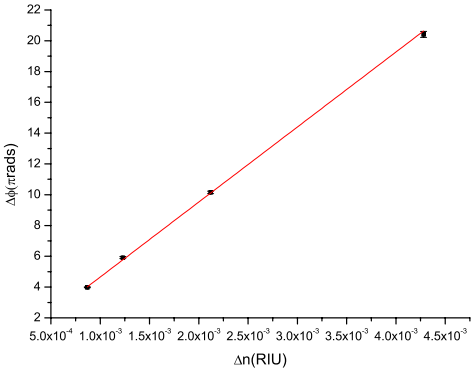

Figure 3.13 Standard sensor chip: phase shift plotted as a function of the difference in refractive index units of 0.5, 0.25, 0.15, 0.10 M solutions of HCl. The slope of the curve is 4873•πradRIU^{-1} and the LOD is estimated to be 2.72x10^{-7} RIU.

The sensor chip was then diced using a diamond tip pen for silicon leaving a single mode section (input) of 2 mm, a sensing area of 15 mm and a bimodal output section of 5 mm as showed in Figure 3.14. Even if it was desired to use a chip with 1 mm length in the SMS and 0.65 mm length in the BMS as simulated, due to the setup restrictions and the difficulty to couple the light while keeping the microfluidic cell and all other sub-systems operating, it was decided to employ the chip with 2 mm length SMS and 5 mm length BMS. The chip was polished following the protocol explained in section 2.4.3 and then placed in the holder previously redesigned to handle the smaller length. The calibration was performed again by injecting the same concentrations of HCl as showed above in Figure 3.15.

Figure 3.14 Sensor chip diced with a 2 mm single mode section followed by a 15 mm sensing area and 5 mm bimodal section. The chip was later polished and the microfluidic system was attached to repeat the calibration of the shorter biosensor.

Figure 3.15 Bulk calibration of the short chip (total length of 22 mm). Injections of 0.5, 0.25, 0.15 and 0.10 M of HCl were successive performed.

The phase shift was plotted as a function of the different refractive index changes obtaining a bulk sensitivity of 4938•πradRIU^{-1}, a visibility of 18.3% and an estimated LOD of 4.24x10^{-7} RIU as showed in Figure 3.16.

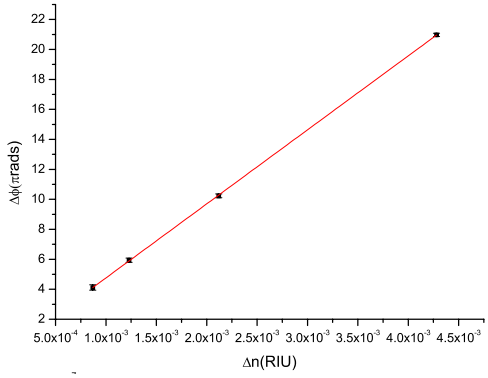

Figure 3.16 Phase shift as a function of the change in refractive index units of the three solutions with different concentrations of HCl (0.5, 0.25, 0.15 and 0.10 M). The slope has been calculated to be 4938•πradRIU^{-1} and the LOD estimated to be 4.24x10^{-7} RIU.

3.3.3 Conclusion

Different lengths were simulated obtaining no significant difference between the energy coupled into the fundamental and the first order mode thus, no significant differences in terms of sensitivity should be expected. Reductions of the single mode section as short as 186 µm could be performed without affecting the device sensitivity. Moreover, a BiMW sensor chip with 2 mm SMS and 5 mm BMS and a total length of 2.2 cm was experimentally tested achieving LODs in the same order of magnitude and similar sensitivities and visibilities than for the long version. Smaller reductions as short as 1.6 cm should be feasible as well and this way, it could be possible to increase almost 50% the production of chips per wafer without comprising the device sensitivity.

3.4 Biolayer thickness and surface sensing range

Since the evanescent field travelling on the boundary of the core and cladding penetrates only some hundreds of nanometers exponentially decaying (due to the light wavelength), it is important for all kind of photonic biosensors to keep the bioreceptors close enough to the surface [58].

3.4.1 Simulation

In order to evaluate the surface sensitivity, a biolayer is simulated as uniformly growing in the boundary between the core and the sensing media interface as showed in Figure 3.17. For a biolayer process we can assume a growing from 0.1 nm to 1 µm with a

refractive index of 1.45 (value for a protein layer) and the bulk sensitivity dependence on it will be:

$$\partial S_{surface} = \partial(N_{eff}TX_{10} - N_{eff}TX_{00})/\partial d_{bio}. \qquad (3.3)$$

We employed for the simulation waveguide core thicknesses between 260 and 380 nm and the plots are showed in Figure 3.18 for TE polarization and in Figure 3.19 for TM polarization.

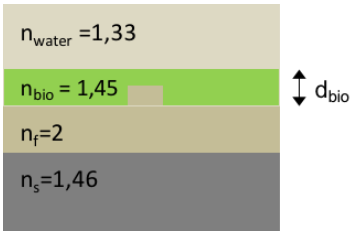

Figure 3.17 Proposed 2D model for simulations of a biolayer on top of the sensing area with refractive index 1.45 and thickness d_{bio}.

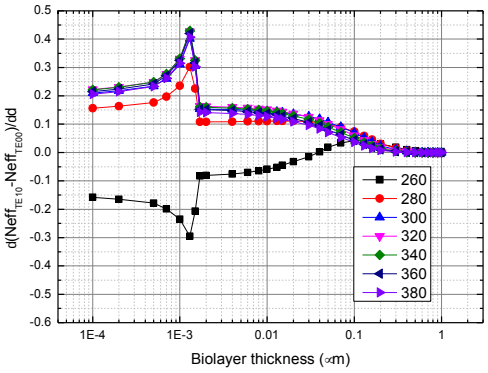

Figure 3.18 Simulation of the surface sensitivity (x 10^{-6} nm^{-1}) for TE polarization as a function of a biolayer with thickness *d_{bio}* growing in the boundary of the core-water interface for different waveguide core thicknesses (260 to 380 nm) of the BiMW biosensor.

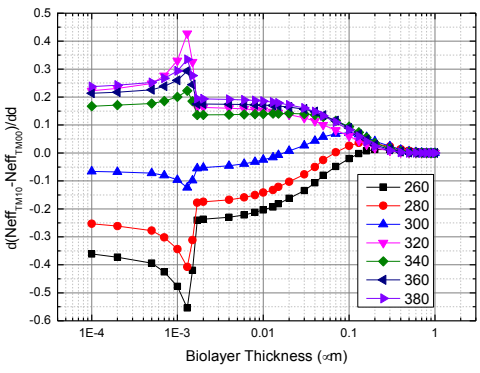

Figure 3.19 Simulation of the surface sensitivity for TM polarization as a function of a biolayer with thickness d_{bio} growing in the boundary of the core-water interface for different waveguide core thicknesses (260 to 380 nm) of the BiMW sensor.

There is an increasing tendency of the surface sensitivity as the biolayer grows between 0.1 and 2 nm. Then, after the thickness of the biolayer reaches the rib height (2 nm) a discontinuity is observed followed by a decreasing behaviour until the surface sensitivity is practically zero after biolayer thicknesses higher than 400 nm. Different core thicknesses will have different sensitivities and behaviours. For example, core thicknesses below 270 nm in TE polarization or 300 nm in TM polarization, will show an increasing sensitivity behaviour in the biolayer thicknesses between 2 – 400 nm. This could be related to the critical working point effect in hetero modal interferometer biosensors where a divergence in spectral sensitivity is expected [59]. When moving to the right or left of the critical point a switch in the increasing or decreasing sensitivity behaviour is expected. Biolayers between 3 and 100 nm will provide the most stable surface sensitivity value which is within the usual range for biological interactions (as antigen-antibody or DNA-DNA hybridizations) relevant for clinical diagnosis. As observed in the graphic, the best sensitivity will be obtained with waveguide cores of 340 nm which is in a good agreement with our physical design.

Moreover, the effects of the rib size in the surface sensitivity (as expressed in equation 3.3) were also simulated observing no direct effect in the actual working size ranges. The plot is showed in Figure 3.20.

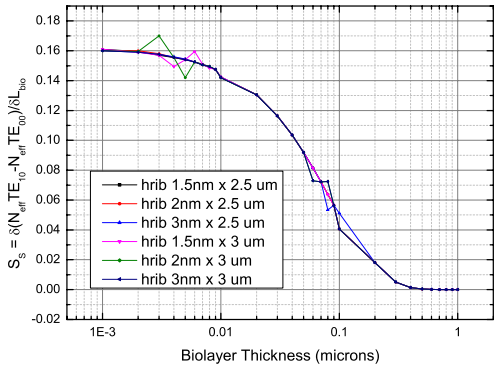

Figure 3.20 Surface Sensitivity for different rib sizes in relative terms as a function of the biolayer thickness.

3.4.2 Experimental evaluation

Given the required expertise to properly assemble surface biolayers, a collaboration with PhD students from our group was established. Human growth hormone has been sensed using a BiMW nanointerferometric biosensor with experimental LOD in the order of 3 pg•mL^{-1} [60]. An experimental bulk sensitivity S_{bulk} = 2056•2π rad RIU^{-1} was calculated. In order to calculate the surface sensitivity $S_{surface}$, firstly, it is necessary to calculate the resolution of the effective refractive index. It is given by

$$\Delta N_{eff,min} = \frac{\Delta\varphi_{min}\bullet\lambda}{2\pi\bullet l}, \qquad (3.4)$$

where $\Delta\varphi_{min}$ is the phase resolution, λ is the wavelength and l is the interaction length Having an interaction length of 15 mm, a λ = 633 nm and a phase resolution experimentally calculated to be 1x10^{-4} 2π•rad, a resolution of the effective refractive index of **4.2x10^{-9} RIU** is calculated. By using these values and the ones obtained by simulating a 10 nm biolayer with a refractive index n_{bio} = 1.45 in aqueous media (n_{H2O} = 1.33), of a BiMW nanointerferometric biosensor with 340 nm core thickness and 4 μm rib width and 1.5 nm rib height, as listed in Table 3.4, and the relation given by

$$\Delta N_{eff} = (\Delta Z_C)^{-1}\frac{\eth N}{\eth n_c}\frac{dn}{dc}h\Delta\Gamma, \qquad (3.5)$$

where $\Delta\Gamma$ is the surface coverage, h is approximated to 2 (see [61]) and dn/dc is taken as 0.188 cm^{3}g^{-1} [40], it is possible to resolve the equation to obtain a final surface coverage $\Delta\Gamma$ using the values of the mode TE$_{10}$ as listed in Table 3.4 when simulating a nominal BiMW with h_{bio} = 10 nm, n_{bio} = 1.45, of only 2.8 fg•mm^{-2}.

Table 3.4 Calculated sensitivities of the BiMW at λ = 633 nm. For bulk sensitivity, an aqueous media was employed. For surface sensitivity, a 10 nm thick biolayer was simulated as being placed in the boundary of the core and cladding.

Mode	N_{eff} [RIU]	ΔZ_C [nm]	$\delta N/\delta n_C$ [n_C=1.33]	$\delta N/\delta d_{bio}$ [x10^{-6} nm^{-1}]
TE$_{00}$	1.890911	74.95	0.02	53.2
TE$_{10}$	1.570647	120	0.1105	199

3.4.3 Conclusion

Biomolecular interactions must be kept in the range of a few nanometers to hundreds of nanometers close to the core-cladding boundary in the sensing area. As long as the biological linker or bioreceptors ensures to keep these values, excellent surface

sensitivities can be achieved. This is not a problem for most of the biomolecular interactions recorded by a biosensor as any protein or DNA layers will lie in the orders or tens of nanometers. In other hand, during the detection of human growth hormone a theoretical surface coverage of 2.8 fg•mm^{-2} was calculated for a BiMW interferometric biosensor, and an experimental LOD of 3 fg•mL^{-1} of human growth hormone was showed.

3.5 Microfluidics system optimizations

The sample delivery is fundamental when dealing with biosensors. Little amounts of the sample fluid should be delivered to the sensing area while they are interrogated by both modes of the BiMW nanointerferometric biosensor. In order to keep reproducible results, the microfluidic system should ensure the delivery of samples at a constant flow rate, normally between 10 and 50 µL/min.

3.5.1 Theory and design

The three main forces driving the fluids at microscale are shown in Figure 3.21: the electromagnetic forces described by the Maxwell equations, the Flick's law to describe diffusion laws and the Navier-Stokes equations to handle viscous fluids. The current design of the microfluidic cell is 20 mm long by 1 mm width and 0.75 mm height, resulting in a total volume of 15 µL. It seems to be quite large and as previously discussed, the closer the analyte is to the biosensor surface, the less time it will require to diffuse to the bioreceptor improving the sensitivities. First, let us recall the Peclet's number $Pe = Q/WD$, where Q is the velocity flow rate, D is the diffusivity of the target analyte and W is the cell width and the aspect ratio $n = L/H$ where L is the chamber length and H is the height. In order to keep laminar flows the system should comply $Pe>n$ and $Pe >> 1$. By approximating Q ~ 30 µLmin^{-1}, L = 15 mm and W = 50 µm, and with the aim to keep aspects ratios between 120 and 1200, a quick calculation showed that height values H between 12 µm and 125 µm should work. Widths W between 50 and 100 µm could allow visual alignment to the BiMW chips. A reduction of the LOD could be expected thanks to the smaller microfluidic chamber [62].

In order to produce the reduced microfluidic chamber, it was necessary to firstly fabricate a mold which can be further employed for casting of the microfluidic cells. The mold was fabricated using SU-8 at clean room facilities of the ICTS at the Barcelona Institute of Microelectronics (IMB-CNM-CSIC) by employing standard UV photolithographic

techniques and following the protocol showed in Appendix B.1. Then, PDMS casting was performed as described in appendix B.2 and it was finally employed in a microfluidic system as described in section 2.4.4. Figure 3.22 shows a scheme of the PDMS chamber attached to the chip surface.

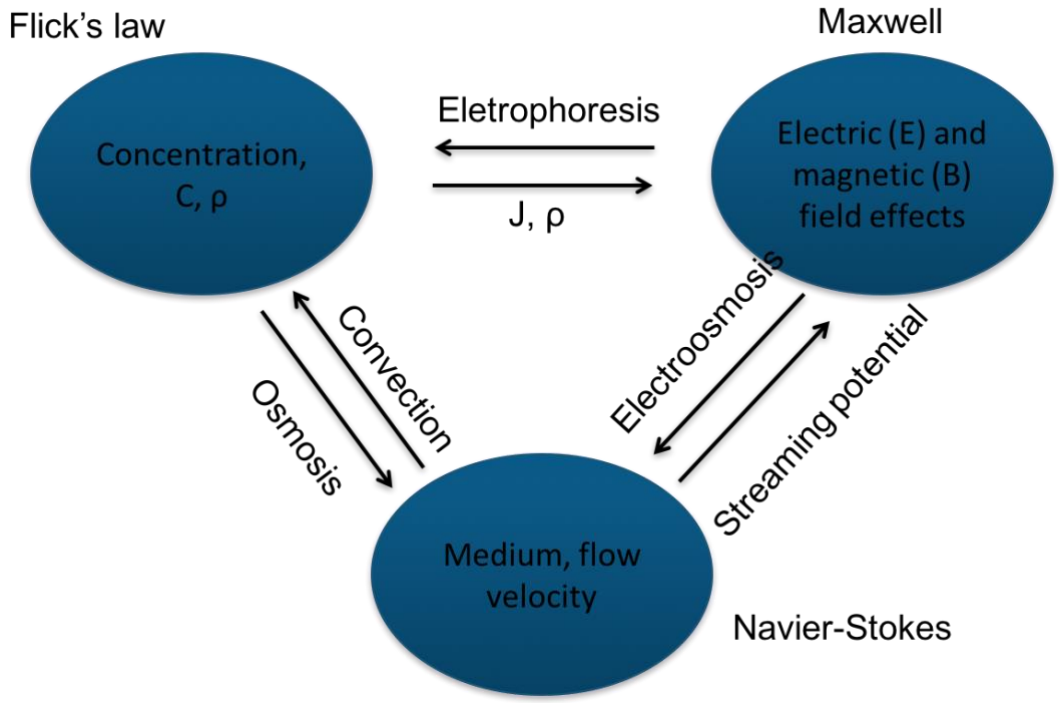

Figure 3.21 Main driving physical forces in microfluidics: electromagnetism, Flick's diffusion laws and Navier-Stokes for viscous flows.

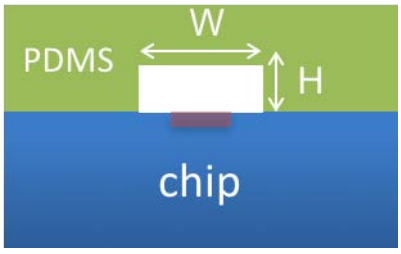

Figure 3.22 Proposed reduction and individualization of microfluidic channels.

Moreover, multiplexed inputs and outputs are desired in order to minimize the number of connectors to macro sources. To do so, it is necessary to start designing the photolithographic masks.

3.6 Fabrication

The photolithographic mask designs were done in Adobe Illustrator™ including curved and multiplexed individualized channels. In order to properly control the width of the channels, a conversion between the line width in the design software and the real value when printed has to be performed (see Table 3.5). The final mask design is showed in Figure 3.23 and the printed one is showed in Figure 3.24.

Table 3.5 Values for drawing in Adobe® Illustrator

Line width	Real width
2 pt	1 mm
1 pt	0.5 mm
0.5 pt	250 µm
0.25 pt	125 µm
0.1 pt	50 µm
0.01 pt	5 µm

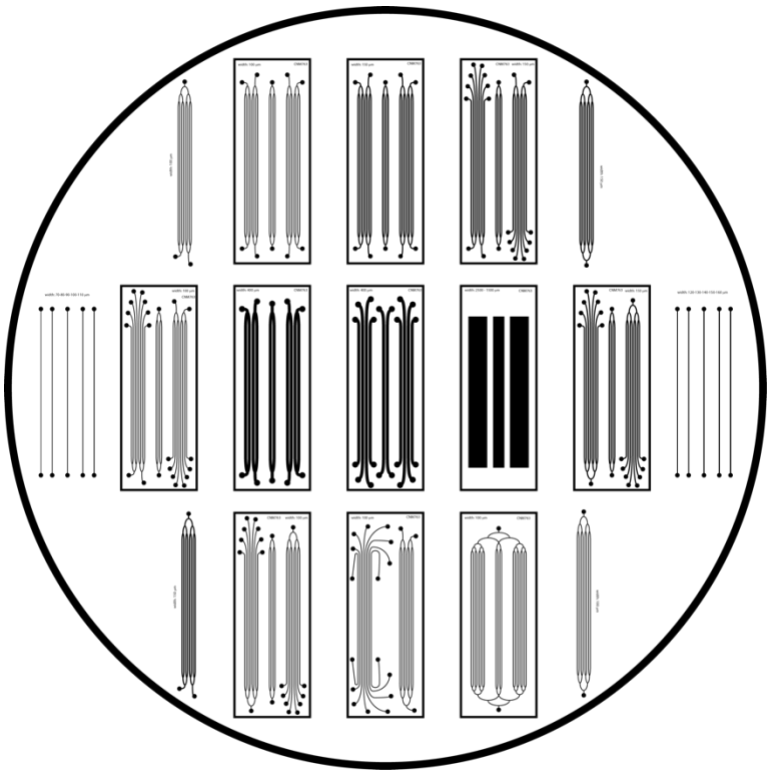

Figure 3.23 Proposed designs of photolithographic masks for building of the SU-8 mould for casting multiplexed, individualized microfluidic cells.

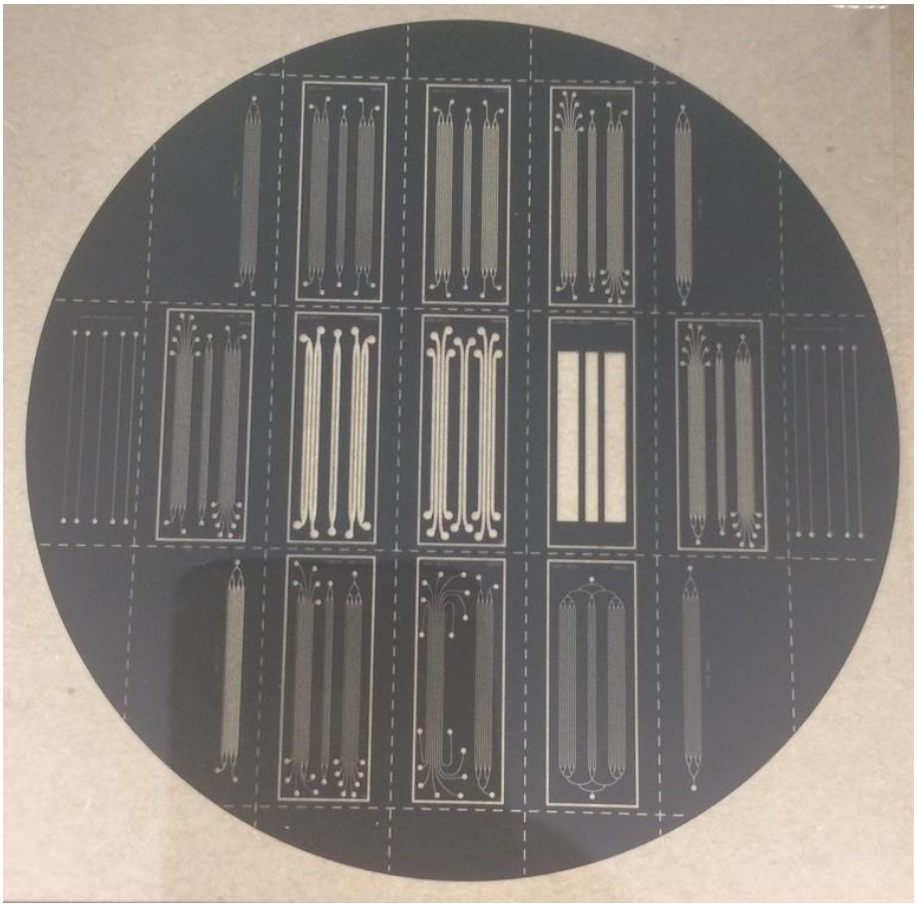

Figure 3.24 Picture of the printed photolithographic mask.

Two sets with different heights were fabricated at clean room facilities of the ICTS at the Barcelona Institute of Microelectronics (IMB-CNM-CSIC) in collaboration with PhD. Isaac Rodríguez-Ruiz from the Chemical Transducers group, following the protocol showed in Appendix B.1. A picture of the fabricated mould is showed in Figure 3.25. After fabricating the SU-8 masters, they were diced in individual chips (see Figure 3.26) with the aim to perform further PDMS (Sylgard 184) casting as required using the protocol showed in Appendix B.2. A picture of the PDMS microfluidic cell fabricated after mold casting is showed in Figure 3.27.

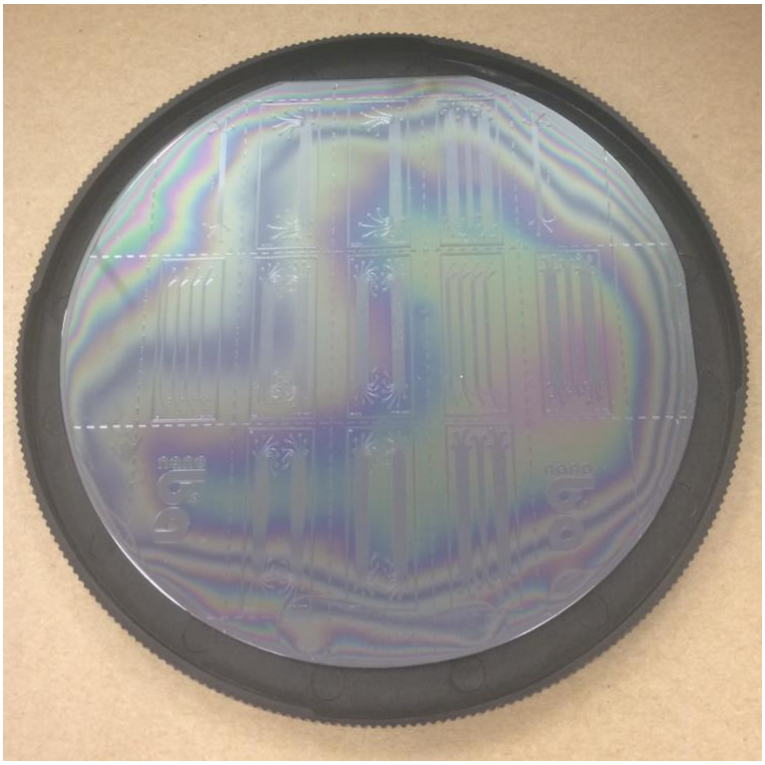

Figure 3.25 Picture of the fabricated microfluidic moulds for future PDMS casting of the microfluidic chamber.

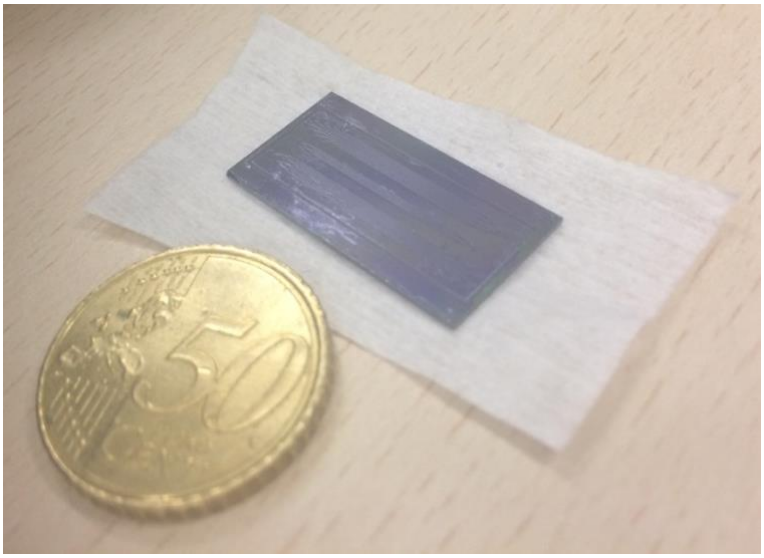

Figure 3.26 Individual chip for patterning in PDMS.

Figure 3.27 PDMS cells obtained after mould casting of the previous SU-8 chips.

3.6.1 Experimental evaluation

The materials used for the microfluidic system are described in section 2.4.4. Due to the small microfluidic cell width (50 µm or 100 µm), an aligner is required to correctly place the microfluidic chamber on top of the BiMW sensing area. Figure 3.28 shows a picture of the individual 100 µm width and 50 µm height microfluidic cell and Figure 3.29 shows the chip and the microfluidic cell (i.e. the cartridge) detached from the setup.

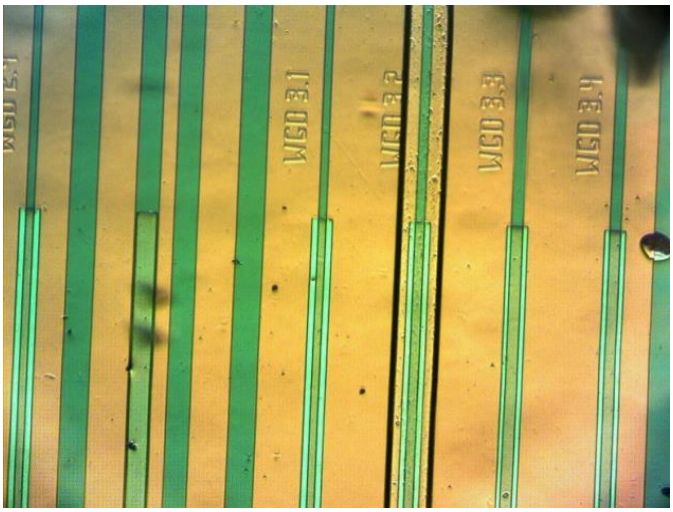

Figure 3.28 Individualized microfluidic cells in the alignment setup.

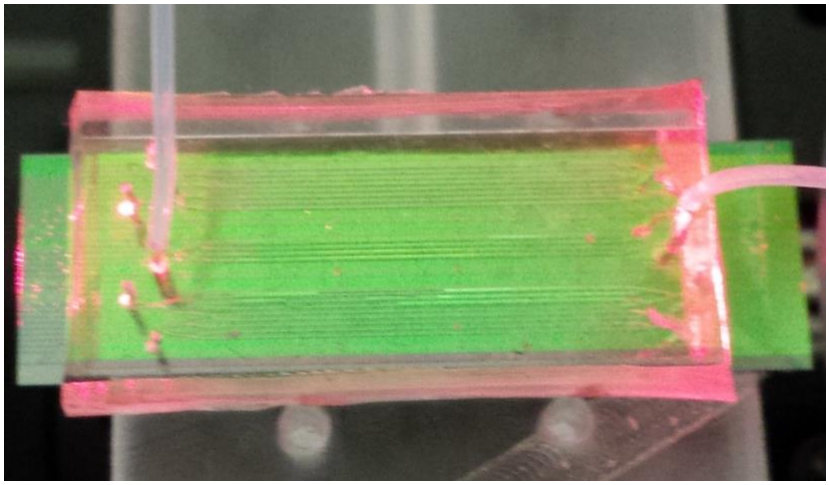

Figure 3.29 Individualized microfluidics placed on chip.

The microfluidic cell was tested as part of the project "Multiplexing detection of tumor-associated autoantibodies for early diagnosis of colorectal cancer using a nanophotonic biosensor" in collaboration with PhD. César S. Huertas. To perform the detection of colorectal cancer (CRC), a BiMW biosensor was functionalized by covalently attaching specific receptors complementary to the CRC autoantibodies as seen in the inset a of Figure 3.30. When the sample with the auto-antibodies is delivered, a specific signal for each antibody will be obtained. Inset b of Figure 3.30 shows a zoom-in of the individual microfluidic channels (100 µm x 50 µm) over the BiMW sensor. As a baseline, a calibration curve using the old microfluidics with h = 500 µm and w = 1000 µm was calculated, obtaining a LOD of 471 ng•mL^{-1} (see inset c of Figure 3.30). In the other hand, when calculating the calibration curve with the same biosensor and with the smaller microfluidic cell (h = 50 µm, w = 100 µm), a value of 3 ng•mL^{-1} was obtained instead. This represents an increment of two orders of magnitude.

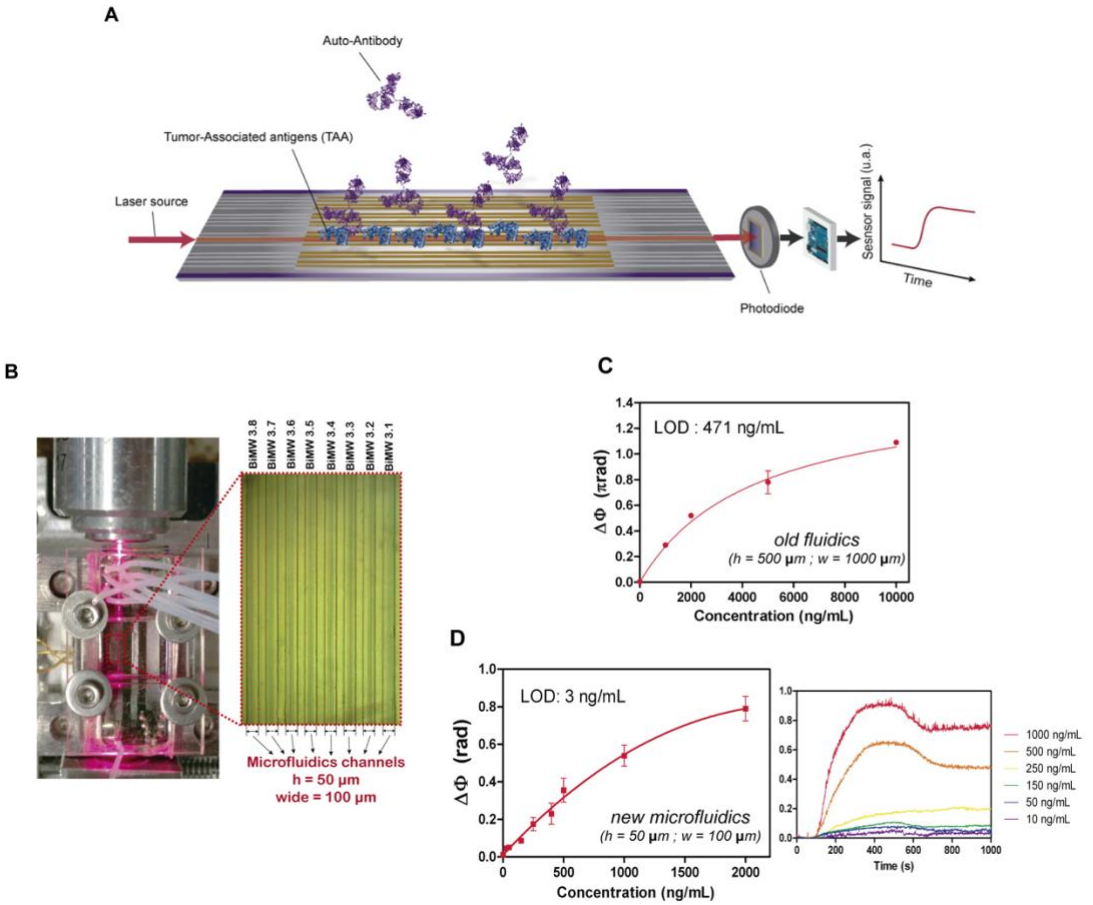

Figure 3.30 Improvement in the LOD when comparing macro and micro fluidic cells. By using an individual microfluidic cell (h = 50 µm, w = 100 µm) the LOD was lowered to 3 ng•mL^{-1} instead of the previous value of 471 ng•mL^{-1} when using the old microfluidic cell (h = 500 µm, w = 1000 µm).

3.6.2 Conclusion

Smaller and individualized microfluidic cells for sample delivery on the BiMW biosensor were designed, fabricated, and characterized. They were fabricated by mold casting of PDMS on SU-8 moulds. The LOD was improved by two orders of magnitude.

3.7 Optical characterization

Using the chips with smaller rib widths and shorter lengths, it is possible to obtain some optical parameters as the numerical aperture and insertion and propagation losses.

3.7.1 Numerical aperture (NA)

Once the rib dimensions have been optimized, we proceed to experimentally evaluate the propagation losses, the NA and the insertion losses. For the calculation of the numerical

aperture, a screen was placed at a distance *f* from the bimodal waveguide output. Since the output is not circular, it was necessary to measure the horizontal axis (*h*) and the vertical axis (*v*) of the spot reflected on the screen. Then, the NA was calculated as: $NA = sin(arctan(h/2f))$ for the horizontal NA and $NA = sin(arctan(v/2f))$ for the vertical NA. The experiment was repeated at two different distances obtaining a final value of:

Horizontal NA: 0.03856 (2.21 degrees)

Vertical NA: 0.85-0.92 (58 to 67 degrees)

As expected, there is a wider NA in the vertical axis thus ensuring that horizontal confinement is being kept. This information can help in the design of a photodiode array to avoid cross-interference between adjacent outputs when exciting multiple waveguides simultaneously (multiplexed BiMW).

3.7.2 Insertion losses

In order to calculate the insertion losses, a TE polarized fiber optic with FC/PC connector was coupled by end-fire to reference single mode and reference bimodal waveguides (i.e. without sensing windows) using PD detection and temperature control. The input power P_{in} without polarization was 1.43 mW, having a TM component power of 50 µW and a TE component of 1.06 mW. For practical purposes, we can consider it as only TE polarized light. In the case of the single mode reference waveguide, the output current as read by the PD (with gain of 0.446 AW^{-1}) was 63.9 µA, thus the output power is P_{outSM} = 63.9 µW. In the case of the bimodal reference waveguide, the current output I_{out} was 26.02 µA, thus P_{outBM} = 58.34 µW. Assuming that the total loss of power is given by,

$Loss_{Total}$ = Waveguide Insertion losses + Propagation losses + PD Insertion Losses,

one could depreciate the insertion losses of the readout device because it remains the same across experiments (the PD was the same) and the propagation losses because the length of the device is small. Thus, the total loss as read at the output would be approximately equal to the insertion loss. Having a P_{in} of 1.06 mW for both reference waveguides, the insertion loss *IL* given by,

$$IL = 10Log_{10}(P_{out}P_{in}^{-1}), \qquad (3.1)$$

the insertion loss of the single mode reference waveguide was 12.19 dB. For the Bimodal reference waveguide, the insertion loss was calculated to be 12.59 dB.

3.7.3 Propagation losses

Propagation losses were calculated using the well-known cut-back method [63]. In this case, while keeping the Insertion losses constant (i.e. using a stable light source like a He-Ne laser and minimizing the mechanical and thermal instabilities) one could assume that the total loss is mainly driven by the propagation losses which will be proportional to the device length. The propagation constant could be then calculated by plotting insertion losses against the device lengths. Single mode reference and bimodal reference waveguides from the same chip were cut with a diamond tip pen for cutting silicon at different lengths (2.65 mm, 12 mm, 3.55 mm and 14.74 mm long). Using a TE polarized He-Ne laser for better spectral stability, the insertion losses were calculated for each chip section by relating the input to output power as showed in equation 3.1. In this case, insertion losses between 26 and 40 dB were calculated and plotted against the length as showed in Figure 3.31. The slope is calculated to be 0.2346 dB/cm for the single mode reference waveguide and 0.2395 dB/cm for the bimodal reference waveguide. These values are in good agreement with the propagation losses calculated in rib waveguides in Si_3N_4 and wavelengths of 633 nm [64].

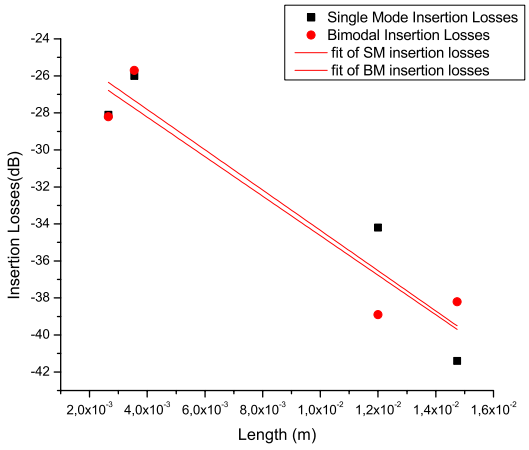

Figure 3.31 Linear fit for the calculation of the propagation losses. A chip with single mode and bimodal reference waveguides was cut with four different lengths. The insertion loss is plotted against the waveguide length and the propagation loss is calculated as the slope of the fitted linear curve (0.2346 dB/cm for the SM and 0.2395 dB/cm for the BM waveguide).

3.8 General conclusion

By analyzing the rib size influence in the modal behavior of the waveguide, it has been determined that rib widths below 3 µm and rib heights below 2 nm are necessary to ensure the single modal behavior in the SMS and the guiding of the fundamental (TX_{00}) and first order mode (TX_{10}) in the BMS, while radiating non-desired modes (TX_{01}, TX_{11}, etc.) ensuring a proper interferometric signal at the output.

The step junction location influence was analyzed theoretically and experimentally and it has been showed that more energy is confined and passed from the fundamental to the first order mode when it is located under the sensing window ($n_{clad} = 1.33$).

Shorter chips were proposed as a way to obtain more chips per wafer thus lowering the cost even further. Firstly, by simulating different lengths, none significant difference was observed in both bulk and surface sensitivity. In a practical manner, a chip was cut down to 2.2 mm length and its bulk sensitivity evaluated, finding no difference between the long and short BiMW sensor chips.

A biolayer thickness working range between 1 and 300 nm has been determined, which is in good agreement with an experimental detection of human growth hormone where a surface LOD of 3 pg•mL^{-1} was achieved.

Additionally, the numerical aperture was experimentally calculated to be .03 and 0.9 for the horizontal and vertical axis respectively. Finally, insertion losses of 12 dB and transmission losses of 0.23 dB/cm were experimentally calculated for both, single and bimodal reference waveguides.

The design of the BiMW nanointerferometric biosensor should include the step junction or modal splitter located 550 µm after the beginning of the sensing window, it must employ fabrication masks with rib widths of 3 µm, it could be as short as 2 cm long, and to ensure the best surface sensitivity, the biolayer thicknesses should be in the range between 1 and 300 nm thick. All these improvements are great and they are fundamental steps towards a completely integrated LOC biosensor, however there is still one main challenge to solve, one problem which has caught the attention of both the telecomm and biotech industries and is the nanometric in-coupling of light.

4 IN-COUPLING MECHANISMS

"A good scientist is a person with original ideas. A good engineer is a person who makes a design that works with as few original ideas as possible. There are no prima donnas in engineering."

- *Freeman Dyson*

This chapter deals with one of the challenges of waveguide based devices with applications in biosensing: the in- and out-coupling of the light from macro sources to micrometric and nanometric structures. This chapter discusses the state-of-the-art solutions and proposes two more: a vertically stacked taper and an inverted one. Their design, simulation, fabrication, optical characterization and comparison are showed as well. Finally, an approach for multiplexed in-coupling is also discussed.

The bimodal waveguide interferometer (BiMW) is one of the most sensitive optical biosensor for label-free detection. However, the waveguides of the BiMW interferometer are designed at nanometric scale in order to properly guide the light at wavelengths in the visible range (λ = 660 nm) while ensuring single mode or bimodal confinement. The rib waveguide used in the bimodal waveguide interferometer (BiMW) with a core of Si_3N_4 (n_{core} =2.00) and cladding of Si_2O (n_{subs} =1.46) has a 3 µm x 150 nm input area [48]. With these dimensions, one of the most complex processes is the efficient coupling of light from a laser source requiring the use of macro elements like lenses, objectives or optical fibres. Moreover, the multiplexed and simultaneous coupling in all the BiMW sensors contained in one chip (from 8 to 20) is a difficult challenge.

4.1 Butt-coupling and end-fire

Historically, common coupling methods have been butt coupling [65] and end-fire [66,67] which are very suitable for laboratory experiments but are far from being useful for combining with compact Lab-on-a-Chip (LOC) platforms. In butt-coupling setups, an objective is used to focus the light at the input of the waveguide. For efficient coupling, it is required that the output field from the fiber matches the mode field of the waveguide. The fiber should be very close to the input face of the waveguide, and the mode fields should be similar in size. Moreover, coupling tolerance to misalignments is minimal

complicating the automation of the in-coupling process. Figure 4.1 shows a typical setup with end-fire in-coupling and PD readout system.

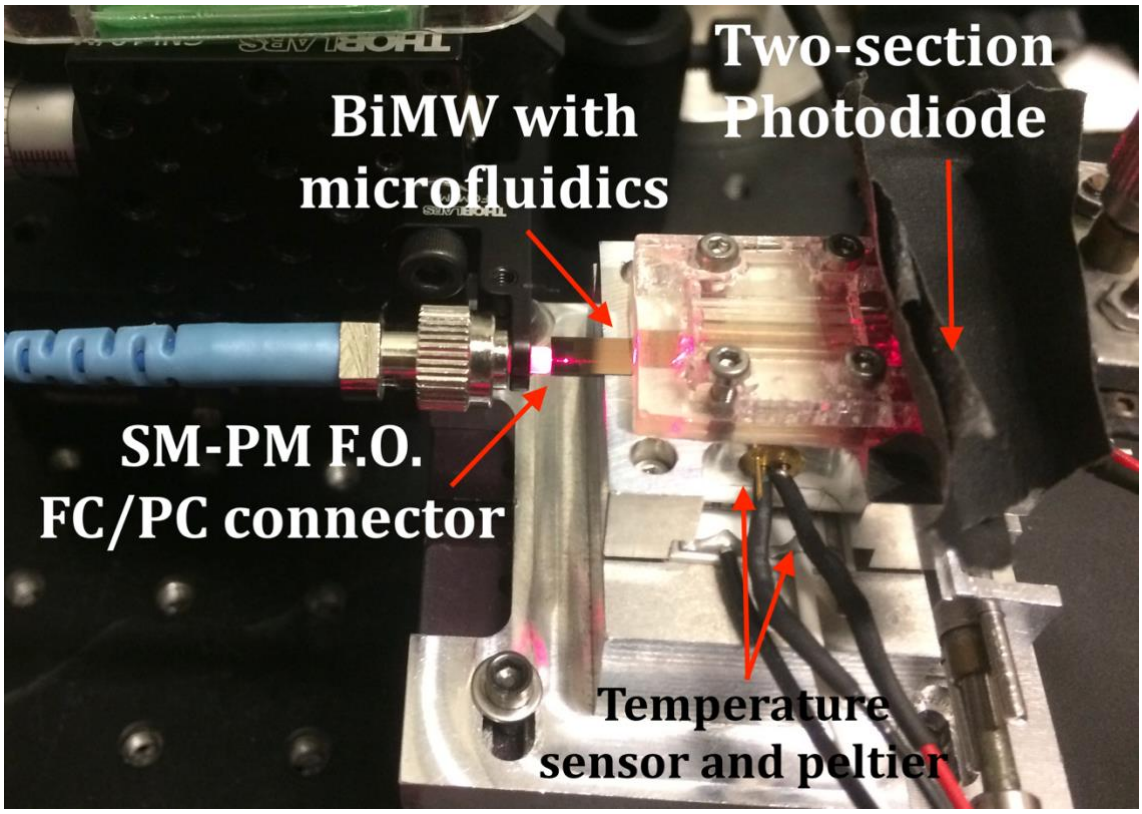

Figure 4.1 End-fire coupled setup with PD detection.

4.2 Grating couplers

Current solutions for light in-coupling are mainly based on grating couplers [68], [69]. In a grating coupler, a periodic structure with a fixed number of rectangular grating teeth is fabricated with duty cycles in the same order of magnitude as the wavelength, and for given combinations of both, light will resonate and will be guided in the waveguide located below the grating. In the literature, there are arrays of waveguide gratings (AWG) [70], subwavelength gratings (SWG) [71–74], achieving good coupling efficiencies, however their fabrication can be problematic. There are gratings in 2D arrays[75], gratings enhanced with polysilicon [76] or mirrors [77], but again, more materials complicate its integration into a LOC and complicate the fabrication. There are gratings built with taper shapes [78], with conical shapes [79], with protuberances [80] or chirped taper gratings [81] also achieving good coupling efficiencies. However, due to the wavelength employed, such gratings usually require e-beam lithography or nanoimprint lithography for the fabrication of duty cycles and deeps in the nanometer scale, increasing the device fabrication cost and time and aggravating its integration at wafer level [82]. In

our group, it has been showed that this approach could work integrated with the BiMW, however, the problem of expensive fabrication costs inherent to grating design requirements for visible light, multiplexing requirements, and small alignment tolerances have thrown back its further development. This is why solutions like the one showed in this Thesis are still required.

4.3 Horizontal tapers

A taper is a device where the width or thickness is gradually diminished. Among their main advantages there is the simpler fabrication employing standard microelectronic techniques, the high coupling efficiency when properly designed, and the integration capability into more complex photonic devices. Multiple taper configurations have been fabricated and studied: horizontal tapers [83], inverted tapers [84],[85], double tip tapers [86] to name a few. Their disadvantages are the large length required to couple enough light and the small entrance area (150 nm height by 50 μm width in our case for a horizontal taper).

4.4 Vertical tapers

As a solution to all the above drawbacks, the fabrication of a two-stage vertically stacked taper (see Figure 4.2) as a cost-effective solution for a future commercial device was proposed. In this case, light is coupled to the input of two tapers vertically stacked. There is an angle difference between both, resulting in light being guided downwards. Then, the bottom taper becomes a rectangular waveguide including an inverted taper buried under it. Light will be coupled into the inverted taper which will in turn become the single mode waveguide at the input of the BiMW sensor. The main conditions for this taper are that it must be compact while it increases the coupling area to facilitate the light entrance and it must be made of a low-cost material with a refractive index between 1.46 and 2.00. Moreover, the taper should be fabricated using standard photolithography techniques at wafer level by slightly modifying our current BiMW fabrication process thus, maintaining the mass production and low-cost requirements.

Although vertical tapers have been previously proposed in the near IR range, its fabrication at wafer level and its integration into a photonic visible biosensor have not been yet reported [87],[88]. Thus, the design, fabrication and characterization of such in-coupling device in the visible range are fundamental steps for the development of nanophotonics biosensors.

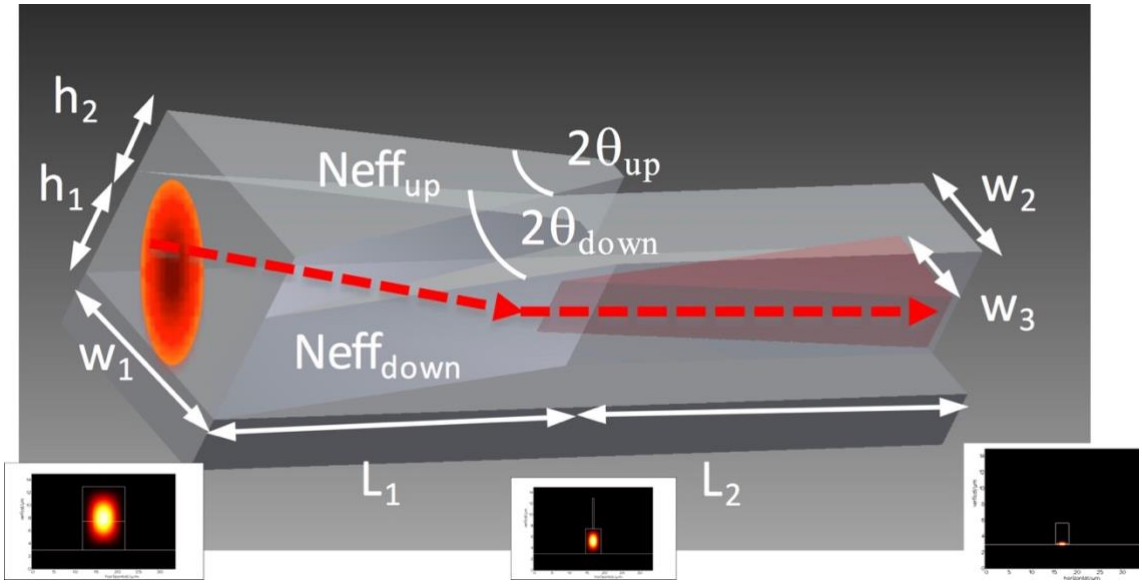

Figure 4.2 Two-staged vertical taper showing intensity distributions at input (*left side*), interface between the two stages (*middle*) and output (*right side*) of the device. Variables used for optimization are showed with their names. Simulations were performed for TE polarization and λ = 660 nm. The inverted taper shown in red will become the bimodal waveguide core. The transparent material should have a transitional refractive index between 1.46 and 2.00.

4.4.1 Vertical taper design and simulation

Recapping Milton and Burst work with tapers, we have the condition:

$$\theta < \frac{\lambda_0}{2Wn_{eff}}, \qquad (4.1)$$

where θ is the half angle of the taper, λ_0 is the light wavelength in the vacuum, W is the taper waist and n_{eff} the effective refractive index [89]. The smaller the angle θ, the higher the effective index will be, thus more light will be guided.

Therefore, we propose a first stage made of two vertically stacked tapers with the angle of the bottom taper smaller than the angle of the upper one, $\theta_{down} < \theta_{up}$ resulting in a larger effective refractive index in the bottom section, $Neff_{down} > Neff_{up}$, thus, guiding light downwards. It is required to use a material with refractive index between the refractive index of the core and the refractive index of the cladding, which we will call transitional material ($n_{subs} < n_{transitional} < n_{core}$). In the second stage, the lower taper becomes a rectangular waveguide incorporating a buried inverted taper which becomes the bimodal waveguide itself. We choose $n_{transitional} = 1.5$ for simulations, anticipating the fabrication

with available low-cost materials. Figure 4.2 shows the proposed device and the parameters used to design it.

4.4.1.1 Parametric design

Knowing that the core diameter of a single mode polarization maintaining fiber optic (SM-PM) is normally 4 μm, we fix w_1 = 5 μm only as a starting point for simulations purposes and subsequently we define width to height relations in a 2D analysis to ensure the light confinement of the fundamental mode: $w_1/(h_1 + h_2)$ for the input or left hand side of stage 1 (LHS1), w_2/h_1 for the boundary between stages (right hand side of stage 1 which becomes the left hand side of stage 2 – RHS1 and LHS2), and w_3=3 μm and height of 150 nm for the output (right hand side 2, these are fixed values to match our existing waveguide interferometer dimensions). Then, a width sweep was performed and total thickness values ($h_1 + h_2$) of 6 and 10 μm were selected since they are feasible to fabricate by doing sequential depositions of 3 or 5 μm layers, and they are already larger than the 4 μm SM-PM fiber core diameter. Stage two has the extra constraint that the final output of the device (right side of the stage two in Figure 4.2) should be 150 nm x 3 μm and the inverted taper should be made of Si_3N_4 (n=2.00), which becomes the core of the sensing waveguide. Figure 4.3 shows the intensity plots of the fundamental mode in TE polarization for all the different 2D models on each of the stages. Figure 4.4 shows the plots of the effective indexes of the first six modes on LHS1 and RHS1 when varying the height and width between 0 and 10 μm. The more modes can be guided, the more energy will be transmitted.

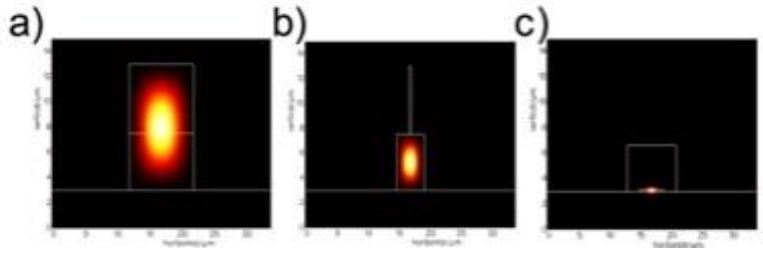

Figure 4.3 Intensity plots of the TE modes in 2D at the input of stage 1 (a), at the output of stage 1/input of stage 2 (b) and at the output of stage 2 (c) of the vertical taper.

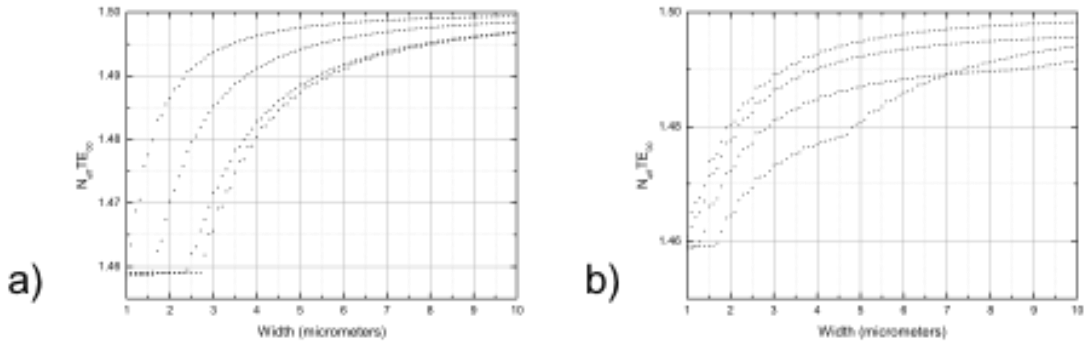

Figure 4.4 Cut-off plots for width sweeps on LHS1 (a) and RHS1 (b) when varying $h_1 = w_1$ between 0 and 10 µm.

The next step is to build the 3D model for the light propagation and then optimize its lengths to keep the maximum energy confined in the shortest possible device. Table 4.1 shows the coupling efficiencies as a function of the length for stage 1. Even if 99% of coupling efficiency could be achieved with lengths L_1 larger than 1900 µm, we want to keep the device as short as possible.

Table 4.1 Coupling efficiency as a function of the length of stage 1 (L1) with h1 = h2 = 3 µm and w1 = 10 µm.

Length [µm]	Coupling efficiency [%]
150	76.1
250	90.3
300	94.5
500	98.3
1500	98.3
1971	99.1

[a)] Refractive Index Units

Once the height and width parameters of stage 1 were defined, an optimization study of the filling factor as a function of the total length $L_{tot} = L_1 + L_2$ was performed. Filling factor values higher than 70% could be achieved with total lengths larger than 1200 µm. Figure 4.5 shows the plot of the filling factor as a function of the total length L_{tot}. The best trade between device length and transmitted energy percentage is obtained with a length of L_1 = 330 µm for the first stage and L_2 = 920 µm for the second stage, respectively. Using these values, an efficiency of 72.25% can be obtained across the complete device (89% for stage 1 and 87% for stage 2). Figure 4.6 and Figure 4.7 show the propagation pattern and the S-matrix coupling coefficient for stage 1. Figure 4.8 and Figure 4.9 do for stage 2 as well.

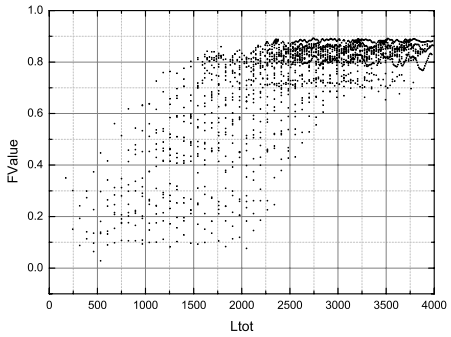

Figure 4.5 Filling factor value as a function of the total length (Ltot) of the whole taper (results of propagation simulations). The filling factor is higher than 70% for total lengths larger than 1200 µm.

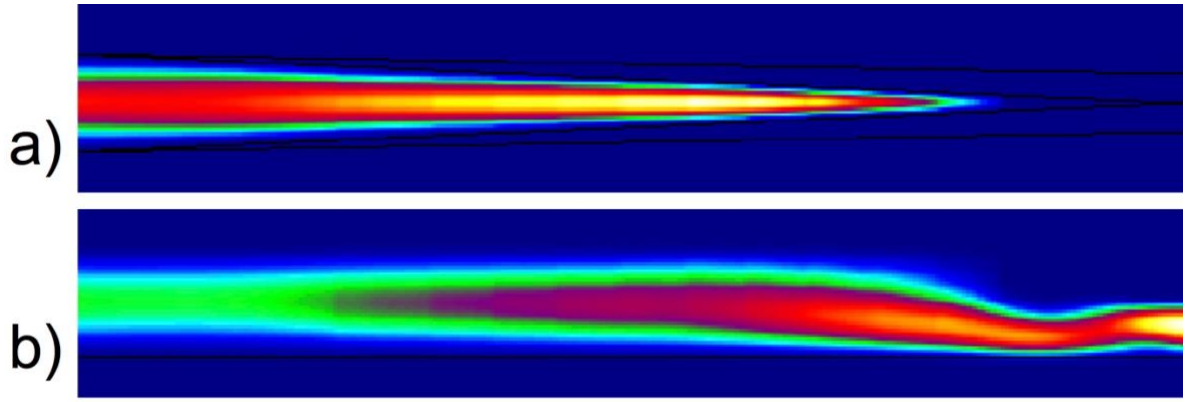

Figure 4.6 Top and lateral view of the propagation of stage 1 using the final dimensions: $h_1 = h_2 = 3$ µm, $w_1 = 10$ µm, $w_2 = 6$ µm, $L_1 = 330$ µm and $L_2 = 920$ µm. Simulations were performed with TE polarization and $\lambda = 660$ nm.

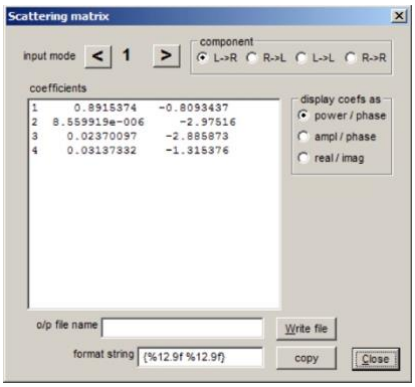

Figure 4.7 Scattering matrix (S-parameters) from left to right propagation of stage 1. A coupling coefficient of 89.15% is achieved for the fundamental mode.

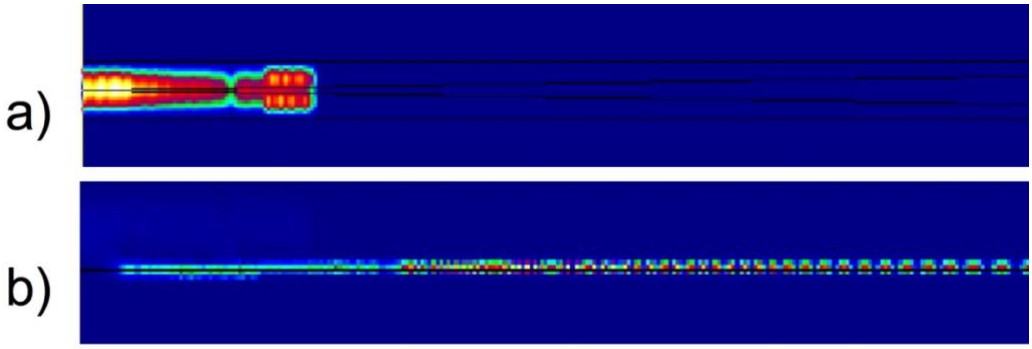

Figure 4.8 Top and lateral view of the propagation of stage 2.

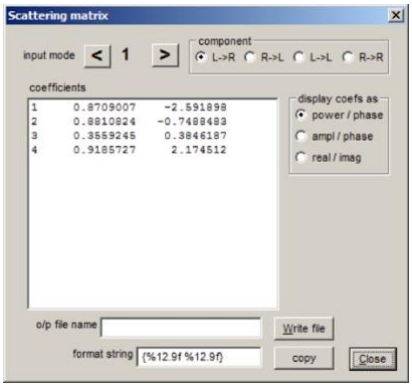

Figure 4.9 Scattering matrix (S-parameters) from left to right propagation of stage 2. A coupling coefficient of 87.09% is achieved for the fundamental mode.

The chosen dimensions are $h_1 = h_2 = 3$ µm, $w_1 = 10$ µm, $w_2 = 6$ µm, $w_3 = 3$ µm, $L_1 = 330$ µm and $L_2 = 920$ µm, obtaining a final in-coupling area of **60 µm²** for the vertical taper input face (w_1 x (h_1+h_2)) instead of the original coupling area of only 0.45 µm² (3 µm x 0.15 µm) corresponding to a single mode waveguide sensor face without any in-coupling element. Figure 4.10 shows the simulated energy confinement for the proposed dimensions.

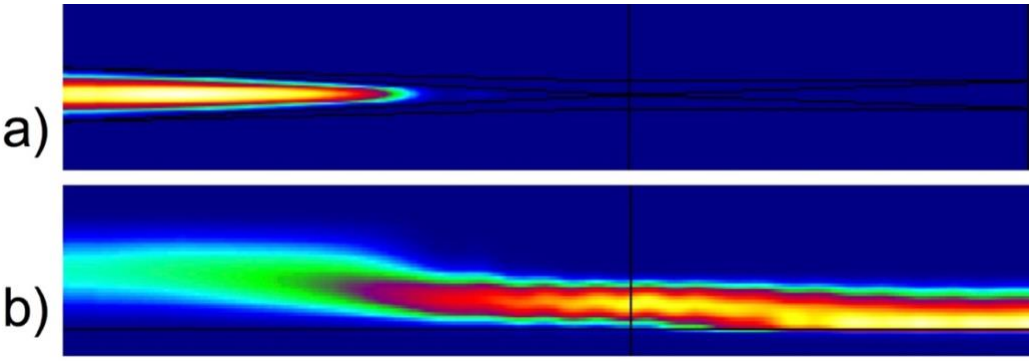

Figure 4.10 Top (a) and lateral (b) view of the proposed vertical taper. All simulations were done with FIMMWAVE ® using a wavelength of 660 nm.

Finally, in order to know the tolerance to refractive index variation of the intermediate material, a study was done varying the refractive index between 1.5 and 2.0 (see Table 4.2), concluding that indexes between 1.5 and 1.7 would work properly.

Table 4.2 Diverse coupling efficiencies for different refractive indexes of materials to be used as intermediary material.

Refractive Index of Transitional Material [R.I.U.] [a)]	Coupling Efficiency [%]
1.5	96.02
1.517	96.14
1.582	97.32
1.657	97.95
1.7	98.47
1.8	NA

[a)] Refractive Index Units

4.4.1.2 Fiber in-coupling simulations

In order to simulate the effects of coupling of the light coming out from a fiber optic being coupled by end-fire to the input and to properly compare the taper coupling losses, all fiber optic specifications were asked to the provider (i.e. Thorlabs ®). The fiber model is a PM630-HP with ceramic ferrule (zirconia) with 125 +-1 μm cladding diameter and 3.5 μm core diameter. The core index is 1.4617 and the cladding index is 1.4571. The $1/e^2$ beam width is 4.2 μm at 630 nm wavelength, and the 1/e beam width is 3.22 μm at 660 nm wavelength. It has a numerical aperture of 0.12, a penetration depth of 14.48 μm and a maximum insertion loss of 1.2 dB. To simulate an input beam in *Photon Design®,* there are three possibilities: a collimated beam, a divergent beam and a convergent beam. The beam incidence plane is focused to the P pivot point (X_p, Y_p, Z_p) with angles V_{tilt} and H_{tilt} for vertical and horizontal tilts respectively as illustrated in Figure 4.11. Positive values of Z_p as illustrated in Figure 4.12, will lead to convergent beams propagating in the waveguide, while negative values of Z_p will lead to divergent beams in the waveguide as showed in Figure 4.13.

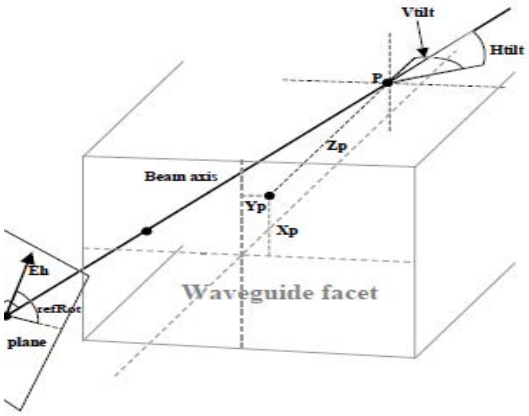

Figure 4.11 Beam plane inciding to the waveguide input facet with pivot point P (X_p, Y_p, Z_p) and V_{tilt} and H_{tilt} incident angles.

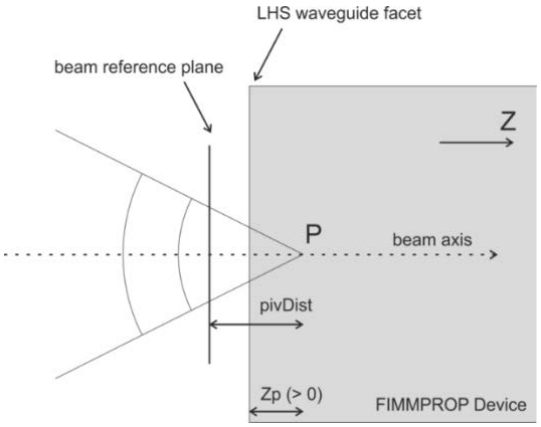

Figure 4.12 Diagram to illustrate the incidence of a convergent beam ($Z_p > 0$). The pivot point P is located at a distance pivDist to the beam reference plane.

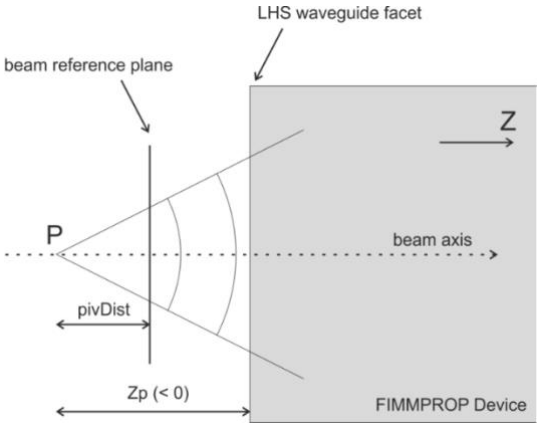

Figure 4.13 Diagram to illustrate the incidence of a divergent beam ($Z_p < 0$). The pivot point P is located at a distance pivDist to the beam reference plane.

4.4.1.3 Simulation of a collimated beam

The first step was to simulate a collimated beam. To do so, Z_p is set to 0, and the beam plane is located 1 µm behind the focal point (pivDist = 1 µm). A Gaussian model with the fiber parameters previously listed was loaded and the beam intensity abs(E_x) is plotted and showed in Figure 4.14.

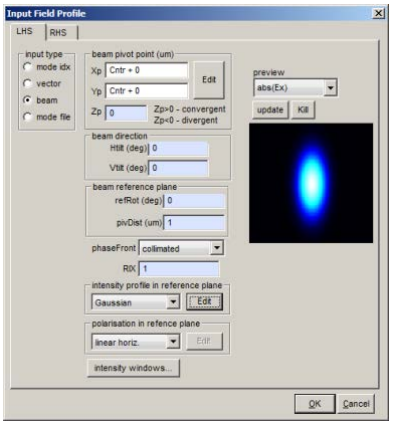

Figure 4.14 Simulated collimated beam for in-coupling. The parameters used were pvdist = 1 µm, Z_p = 0, 1/e beam width= 3.22 µm, Gaussian profile with linear horizontal polarization (TE).

When simulating a single mode reference, *x* and *y* sweeps of the fiber optic position were performed and the output power plotted as a function of such misalignments. Figure 4.15 shows the plots obtained for *x* and *y* offset sweeps. The maximum total output power is 0.078 $J \cdot m^{-2}s^{-1}$ and it has a $1/e^2$ beam width of 6.46 µm at the output facet as showed in Figure 4.15. A similar sweep was performed when having a vertical taper attached to a SM waveguide with the exact same characteristics. A maximum total output power of 0.2274 $J \cdot m^{-2}s^{-1}$ was obtained instead as showed in Figure 4.16. This represents an increment of 2.9 folds of the output power. Even if the waveguide input area has an increment of 133 times when using the vertical taper for in-coupling instead of the single mode waveguide, there is no direct linear relationship to the output power increment (2.9 times). However, we should remember that the increment in the input area will help to automate the in-coupling process for the LOC integration.

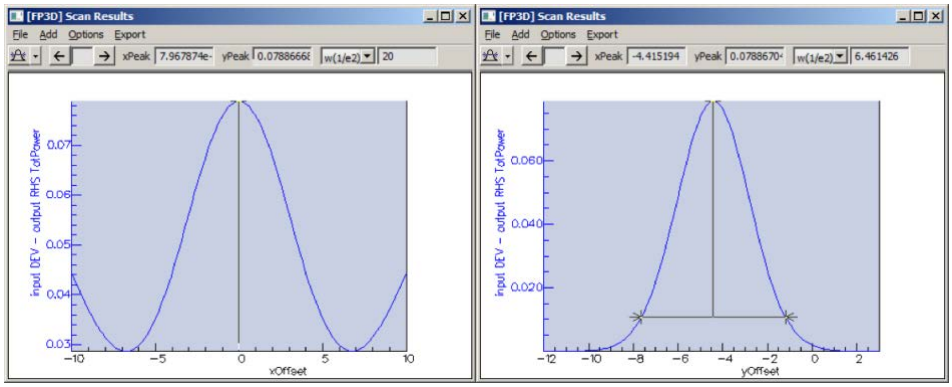

Figure 4.15 Simulated X and Y offset sweeps of a collimated fibre optic beam coupled to a SM reference waveguide with 150 nm core thickness, and a rib size of 1.5 nm and 3 µm width (*total power is given in J•m^{-2}s^{-1} and the x axis in micrometres).*

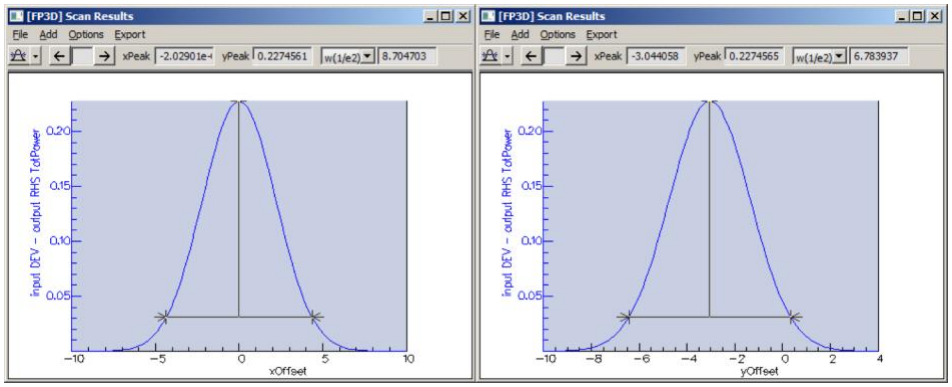

Figure 4.16 Total output power as a function of a x and y offset sweep of a fibre optic collimated beam coupled to the input of a vertical taper and then to a single mode waveguide (*independent axis is in micrometres and the total power is in J•m^{-2}s^{-1}***).**

4.4.1.4 Simulation of a Convergent beam

Similarly, a convergent input beam from a fiber optic was simulated by setting pivDist = 14.48 µm and Z_p = 1.0 µm, using a Gaussian profile with horizontal polarization and a 1/e beam width of 3.22 µm for both horizontal and vertical values. A screenshot of the intensity profile abs(Ex) is showed in Figure 4.17.

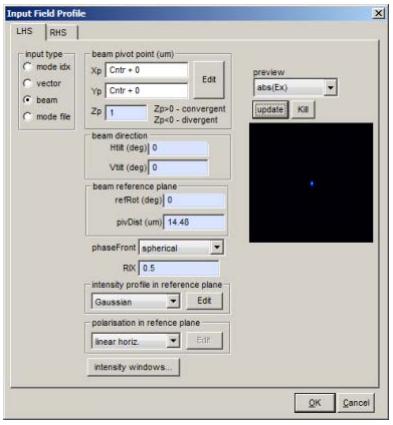

Figure 4.17 Simulated convergent beam with Z_p = 1 µm and pivDist = 14.48 µm.

The peak transmitted total power is 0.099 J•m^{-2}s^{-1} for a single mode reference waveguide (see Figure 4.18) and 0.015 J•m^{-2}s^{-1} when using a vertical taper (see Figure 4.19). It is worth to mention that since it is a convergent beam, the focal point should be located a few nanometers inside the waveguide. In the case of a single mode waveguide, it is practically a butt coupling. However, the vertical taper for in-coupling does not work well in this case as we can observe the loss of one order of magnitude in the total output power. It could be the case that for butt coupling, the insertion losses are practically diminished and it is better to have a focal point in Si_3N_4 (n = 2.0) than SU-8 (n = 1.5).

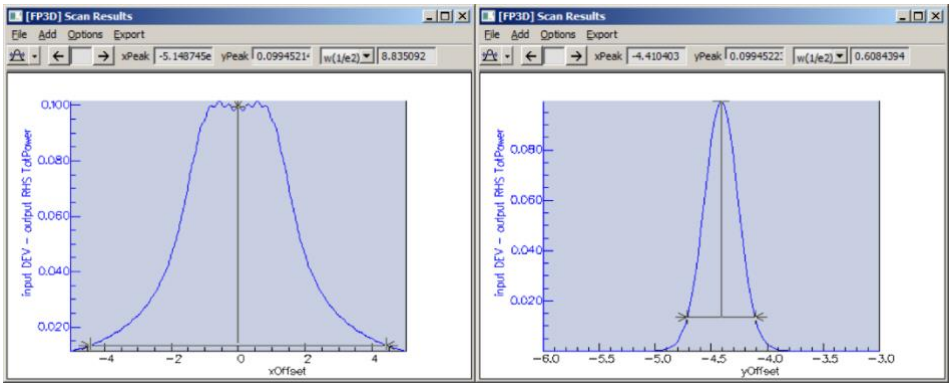

Figure 4.18 Simulated X and Y offset sweeps of a convergent fibre optic beam coupled to a SM reference waveguide (*total power is given in J•m^{-2}s^{-1}*).

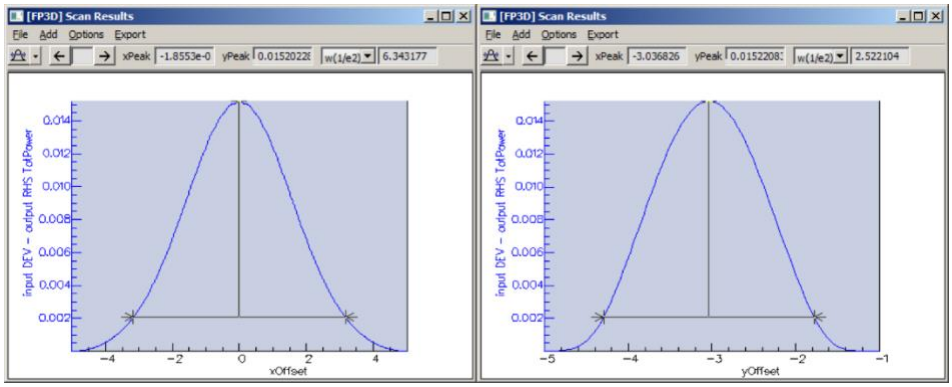

Figure 4.19 Total output power as a function of a x and y offset sweep of a fibre optic convergent beam coupled to the input of a vertical taper and then to a single mode waveguide (*independent axis is in micrometers and the total power is given in* $J \cdot m^{-2}s^{-1}$**).**

4.4.1.5 Simulation of a divergent beam

Finally, in order to simulate a divergent beam incident to the input of both, a SM reference and a vertical taper, parameters are set to Z_p = 14.48 µm and pivDist = 14.48 µm. A plot of the intensity abs(Ex) is showed in Figure 4.20.

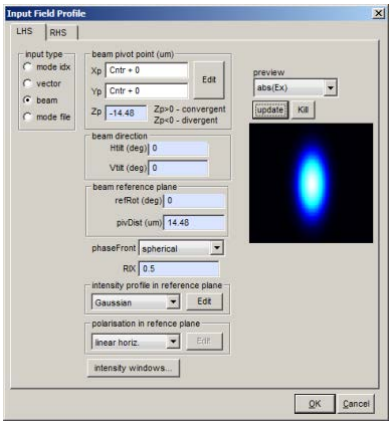

Figure 4.20 Simulated divergent beam for in-coupling. The parameters used were pvdist = 14.48 µm, Z_p **= 1 µm, 1/e beam width= 3.22 µm, Gaussian profile with linear horizontal polarization (TE).**

In the case of coupling a divergent beam as specified to a single mode reference waveguide, the maximum total output power will be 0.0528 $J \cdot m^{-2}s^{-1}$ as showed in Figure 4.21. However, when adding a vertical taper as in-coupling mechanism, a maximum total power of 0.106 J•m-2s-1 is obtained as showed in Figure 4.22. This is a two-fold increment on the total output power.

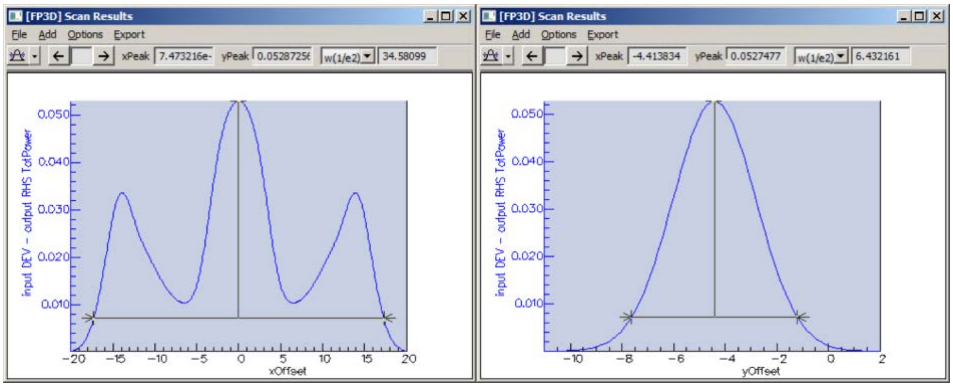

Figure 4.21 Simulated X and Y offset sweeps of a divergent fibre optic beam coupled to a SM reference waveguide (*total power is given in* $J \bullet m^{-2}s^{-1}$**).**

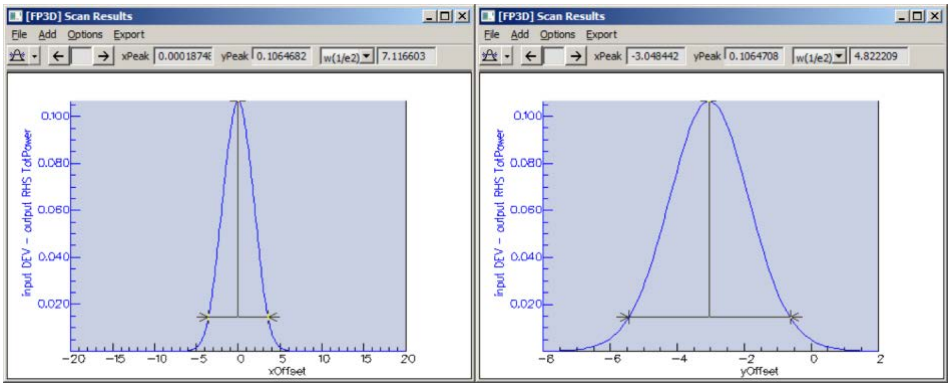

Figure 4.22 Total output power as a function of a x and y offset sweep of a fibre optic divergent beam coupled to the input of a vertical taper and then to a single mode waveguide (*independent axis is in micrometers and the total power is given in* $J \bullet m^{-2}s^{-1}$**).**

It is worth to notice that there is an increment in the coupling tolerance to misalignments, and a larger total transmitted power in the case of divergent and collimated beams. A larger tolerance to input misalignments should be expected. In the case of convergent beams, the proposed vertical taper seems to have similar results as compared to a regular single mode waveguide. In order to experimentally verify these assumptions, the tapers should be fabricated.

4.4.2 Vertical taper fabrication

With the aim to test the proposed vertical taper design, two wafers with 20 chips each one were sent to fabrication at the ICTS clean room facilities of the Microelectronics Institute of Barcelona (IMB-CNM-CSIC). Each chip includes more than one in-coupling element (vertical taper, inverted taper) and reference single mode and bimodal waveguides

completely buried under SiO_2 cladding. But first it is required to define the materials to be employed for fabrication.

4.4.2.1 Fabrication materials

Due to the required taper thicknesses, it could be difficult to employ silicon, polysilicon, silicon nitride or silicon oxide structures without fracturing. We therefore require a material capable of being processed at wafer level in clean room facilities, exhibiting enough mechanical strength, good bonding to silicon oxide and silicon nitride, and with a refractive index between 1.5 and 1.7. Moreover, the material should be processed in layers using standard lithography techniques since two-levels of vertical structures are required. It should provide good resolution and definition of the structures after etching. In other hand, we should be capable of keeping the remaining of the sensor unaffected in order to preserve the sensing window of the BiMW device functional. Polymers are good candidates but it would be necessary to select the right one among the ample available options. SU-8 (SU-8 2005 permanent epoxy negative photoresist, MicroChem®) was selected for the fabrication due to its transitional refractive index and its practicability. It has a refractive index of 1.58 and enough mechanical strength. It is employed at wafer level and its thickness can be controlled and cured in layers thus, after properly developed, it can provide well defined structures without affecting the rest of the sensor.

4.4.2.2 Masks Design

In order to compare the vertical tapers with other coupling structures as horizontal tapers and single mode and bimodal waveguides references, lithographic masks for fabrication were drawn using GDSPy library and object-oriented programming design in Python scripts to obtain a modular approach. Each part of the waveguide and structure was drawn as an object and the GDS mask file generated after executing the script. The final design of the set of masks is showed in Figure 4.23.

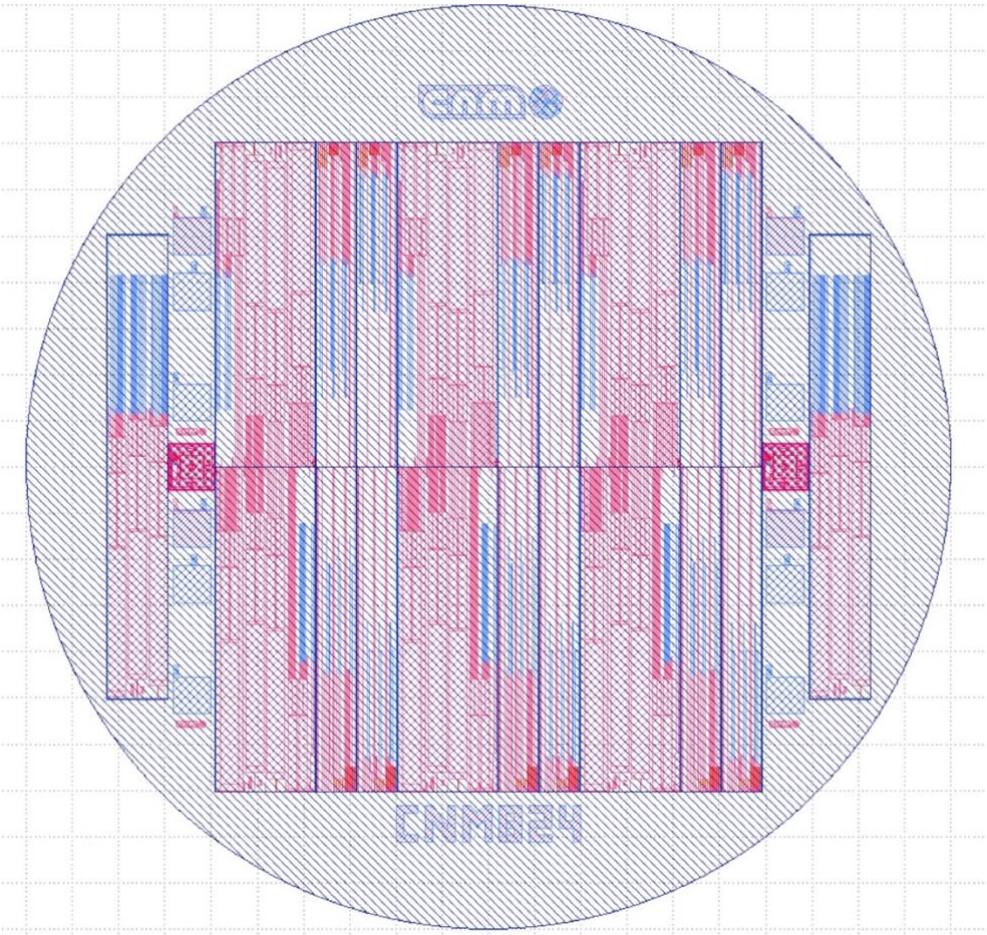

Figure 4.23 Wafer with all the mask levels to be used for fabrication. The outputs of the devices are located facing towards the centre in order to facilitate the cutting with a saw machine without damaging the tapers.

Each one of the designed chips includes three groups with two different in-coupling elements: the first group has horizontal tapers for in-coupling followed by two groups of vertical tapers for in-coupling. Each group is composed of a single mode waveguide, then a single mode and bimodal waveguides without sensing window, then a single mode and bimodal waveguides with a sensing area of 15 mm, then a single mode and bimodal waveguides with a sensing area of 12 mm, and finally, a bimodal waveguide. The same group scheme is repeated using the vertical taper as coupling element for the subsequent groups. The design also includes, in the left side of the chip, a single mode waveguide and a bimodal waveguide to be employed as references. Figure 4.24 shows the distribution as previously detailed. Six mask levels were designed this way: the first mask level (STEP) is used to define the single mode sections where the Si_3N_4 cores are etched from 340 nm to 150 nm. The second level mask (TAPER) is used to delimit the inverted taper by etching another 150 nm of Si_3N_4. The third level mask (MZIN) is used to

delineate the waveguide rib (2 nm height and 3 µm width), the fourth mask (ASEN) is used to open the sensing windows. The fifth level mask (TAPER L1) is used to cure and define the first level of the vertical tapers and the sixth one (TAPER L2) to define the upper one.

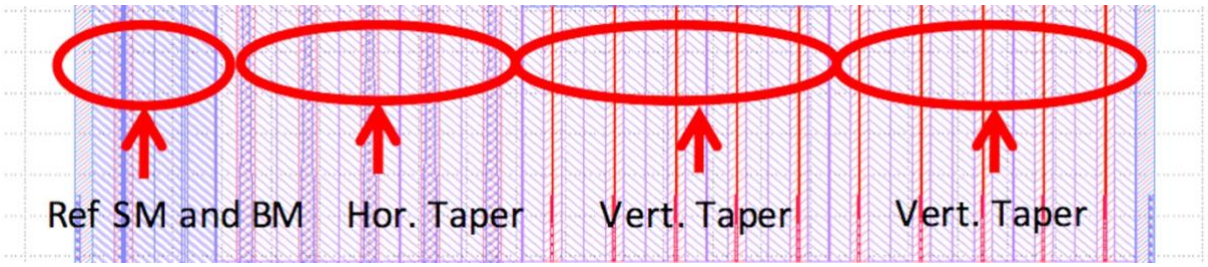

Figure 4.24 Detail of the in-coupling elements. From left to right: single mode reference (SMref), bimodal reference (BMref), horizontal taper plus: single mode, single mode-bimodal, single mode-bimodal-sensing area 1, single mode-bimodal-sensing area 2, and bimodal waveguide, and the same pattern is repeated for two groups of vertical tapers.

4.4.2.3 Fabrication process

Figure 4.25 illustrates the fabrication process. Firstly, a 2 µm silicon oxide layer is thermally grown (Figure 4.25 inset a), followed by 340 nm LPCVD of silicon nitride (Figure 4.25 inset b). Then, the first photolithography step is applied using the STEP mask to reduce the single mode section of Si_3N_4 down to 150 nm (Figure 4.25 inset c). Then a second etching process down to the Si_3N_4 layer (150 nm more) is applied using the TAPER mask to delineate the inverted taper (Figure 4.25 inset d) thus etching the whole Si_3N_4 layer. Next, the third level mask (MZIN) is used to protect and build the rib patterns across the chips (Figure 4.25 inset e) defining a 3.0 µm width and 2.0 nm height rib. Afterwards, 2 µm of silicon oxide is deposited by PECVD (Figure 4.25 inset f) and the sensing regions are defined with RIE using the fourth level of the masks (ASEN) (Figure 4.25 inset g). To fabricate the tapers, two extra steps were employed: deposition of 3 µm of SU-8 (spin-coated at 4500 rpm, pre-baked 1 minute at 95° C in hot-plate, see Figure 4.25 inset h) and curing with the fifth level mask (TAPER L1, 25 s at 365 nm wavelength, i-line, see Figure 4.25 inset i) to immediately deposit a second layer of 3 µm of SU-8 (spin coated at 4500 rpm, pre-baked 1 minute at 95° C in hot-plate, see Figure 4.25 inset j) and curing using the sixth level of the mask set (TAPER L2, 25 seconds at 365 nm wavelength, i-line, see Figure 4.25 inset k). Both layers are finally developed to finalize the process and the wafer was post-baked 2 minutes at 95° C in a hot-plate. All processes

were done at wafer level at the ICTS clean room facilities of the Microelectronics Institute of Barcelona (IMB-CNM-CSIC). Figure 4.26 shows detailed microscopic photos of different parts of the fabricated chips. The SU-8 was removed from some chips in order to expose the fabricated inverted taper. And finally, Figure 4.27 shows a picture of a vertical taper.

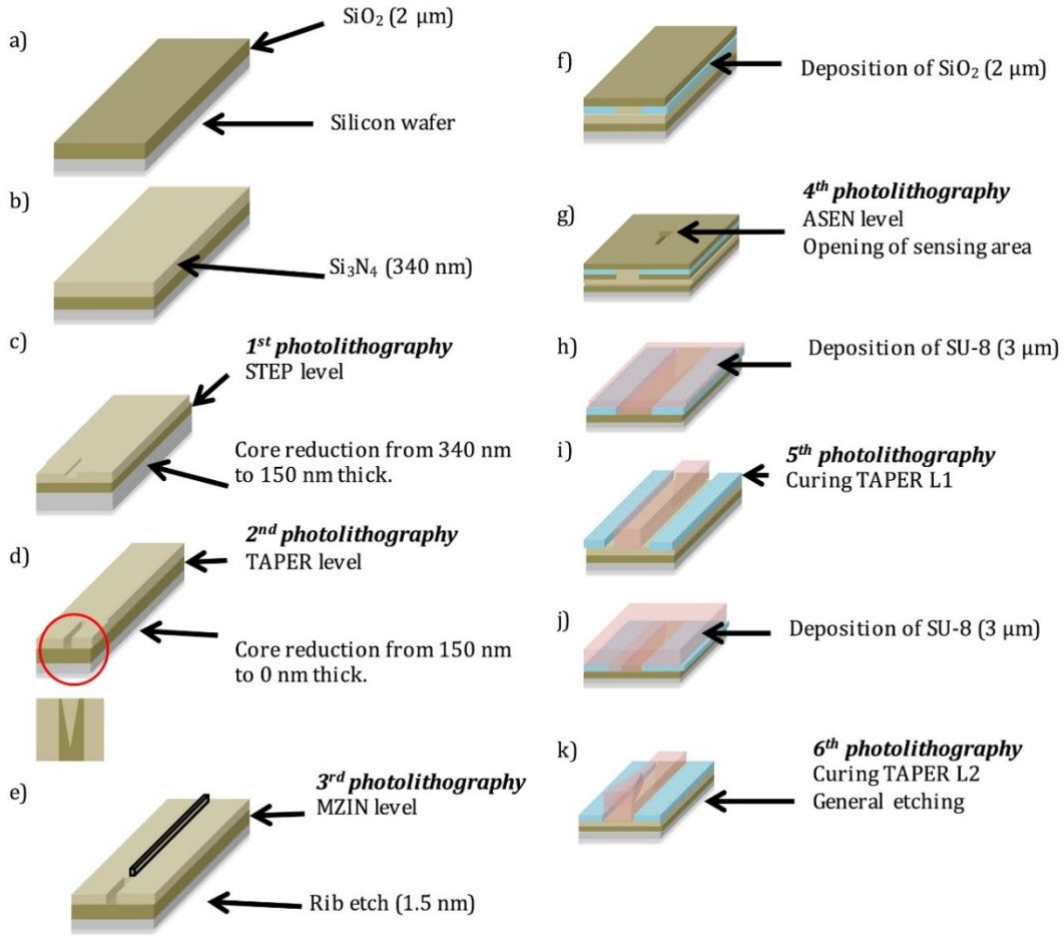

Figure 4.25 Fabrication steps of the BiMW nanointerferometric biosensor chips with vertical tapers for light in-coupling.

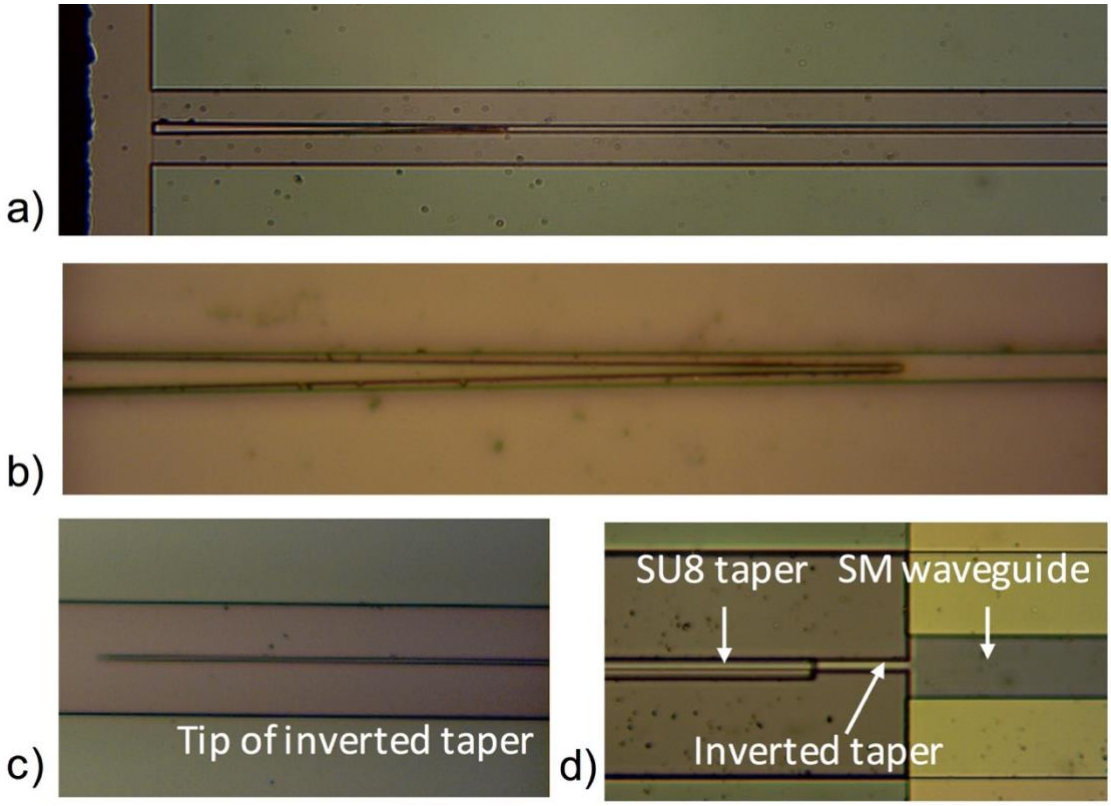

Figure 4.26 Photographs of vertically stacked tapers fabricated with SU-8. The upper photo shows the input of the chip (a). There are 50 µm of separation between the chip edge and the beginning of the taper in order to protect the taper during the cutting process. The sharpness of the edges is critical for the upper section of stage 1; in this case the taper is well defined (b). The SU-8 was removed from some parts of the in-coupling device to show the correct fabrication of the inverted taper: the definition of the tip (c) and the joint with the waveguide (d).

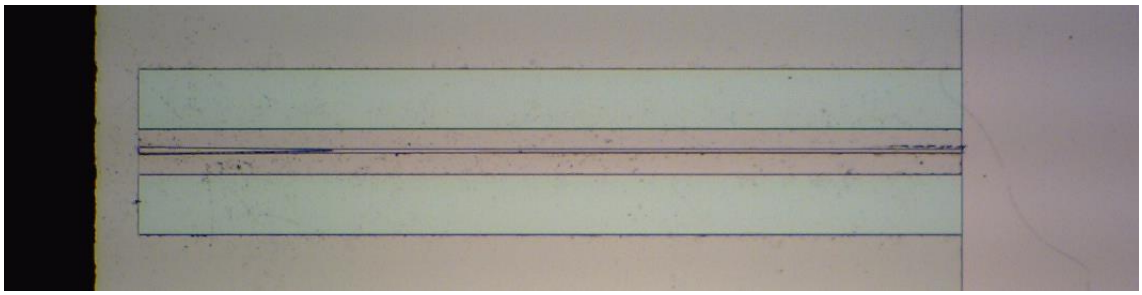

Figure 4.27 Picture of a complete vertical taper. The first stage is 330 µm long and the stage two is 920 µm, adding up a total of 1250 µm long.

4.4.3 Vertical taper experimental evaluation

A schematic representation of the setup employed for the optical characterization of the fabricated tapers is showed in Figure 4.28. A fibered laser diode (LD), LP660-SF60, with a peak wavelength of 658 nm and an optical power of 60 mW controlled with an ITC4005 power source through a TCLDM9 cooled mount for laser diodes (all of them from Thorlabs®) is employed. The single mode (SM) fiber of the LD connects to a 3-paddle polarization controller (Thorlabs® FPC032), which is plugged to a commercial polarization-maintaining single mode optical fiber (P1-630PM-FC-2, FC/PC connectors, 630 nm, PM panda style). The ferrule from the fiber output has been fixed to the fiber holder allowing us to keep a precise control of the polarization orientation with respect to the waveguide plane. Holders and photodiode positioners were made in-house. Figure 4.29 depicts a photograph of the above described setup. When we added the polarization-controller to the optical circuit there was a reduction from 37 mW (using the same commercial PM-SM fiber) to 1.7 mW (including the polarization controller) at the fiber output power. The loss of power could be due to insertion losses between the different elements across the light path, the losses induced by the polarizer, and the losses by scattering showed at the coupling between the fiber and the waveguide input. Nevertheless, this is still power enough to test the devices. Figure 4.30 shows an example of the direct fiber coupling with a vertically stacked taper.

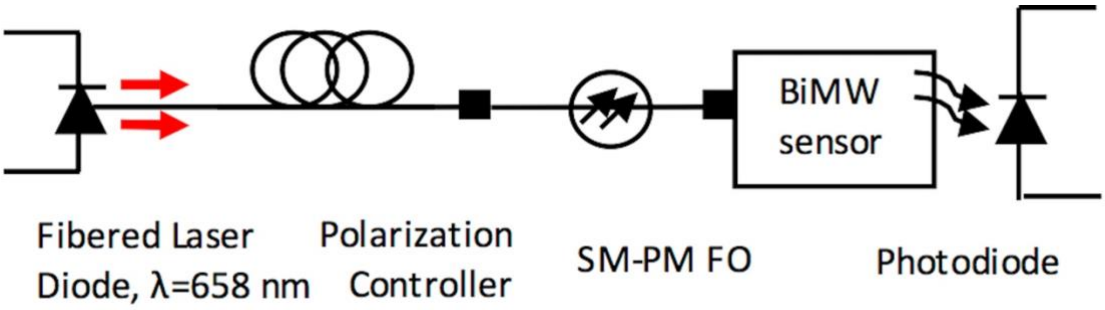

Figure 4.28 Schematic representation of the setup employed for the characterization of the vertical taper.

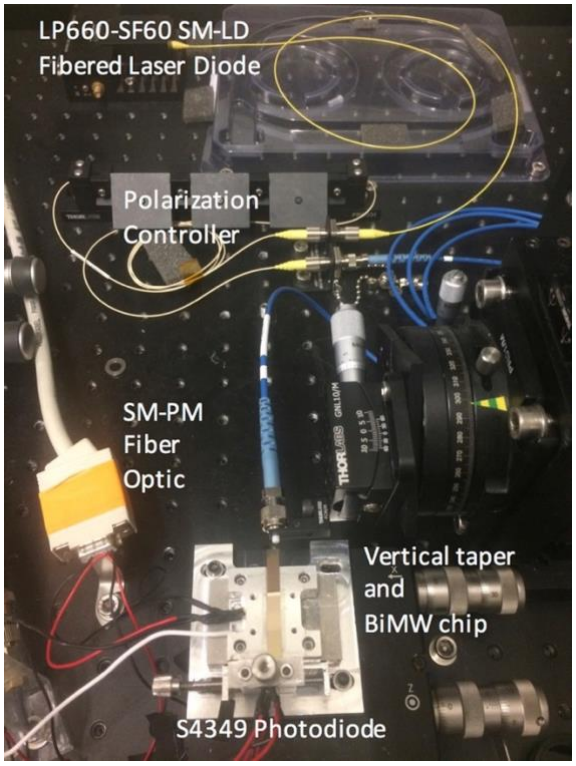

Figure 4.29 Photograph of the setup employed for the characterization of the vertical tapers characterization. The LP660-SF60 fibered laser diode source is showed in yellow (upper part), then light is polarized through the 3-paddle polarization controller and then guided through the P1-630PM-FC-2 single mode polarization maintaining fiber optic showed in blue. It is coupled to the BiMW chip through the vertically stacked taper and finally read with a two-section photodiode.

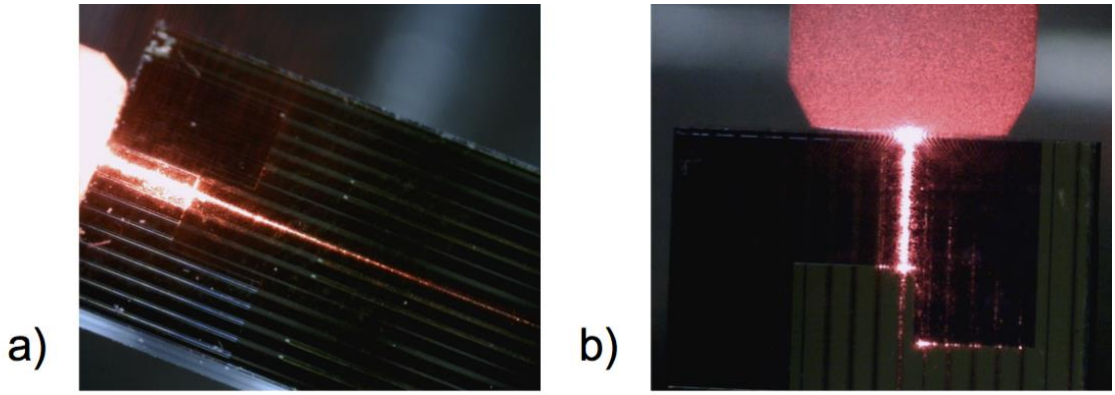

Figure 4.30 Lateral (a) and top (b) photographs of the light in the vertical tapers coupled from a commercial SM-PM fiber.

For the signal read-out, a commercial two-section S4349 photodiode (Hamamatsu®) is connected to a PDA200 amplifier (Thorlabs®), which is in turn digitalized through an USB6361 acquisition card (National Instruments). The employed software for data

acquisition is described in section 2.4.5. A commercial power meter PM120 Thorlabs® is used to experimentally calculate the PD gain.

4.4.3.1 Insertion loss

Knowing the experimental gain of the photodiode (~0.446 AW^{-1}), we have calculated the output power at the exit of the waveguides. By comparing the difference of the output power between the reference single mode waveguide (input power in TE polarization P_{inTE} = 1.13 mW, output power in TE polarization P_{outTE} = 0.246 µW, Insertion Loss = -36.62 dB) and the vertical taper with single mode waveguide (P_{inTE} = 1.13 mW, P_{outTE} = 0.134 µW, Insertion Loss = -39.25 dB), we have obtained a taper insertion loss of 2.63 dB (55%), which is not far from our theoretical calculation of 1.42 dB (72%) performed at the end of section 4.4.1.1. Due to fabrication limitations, the taper structures are not perfectly flat and roughness could play an important role in scattering. Scattering can be observed across the taper as seen in Figure 4.30 inset a; such scattering losses could explain part of the power loss. Additionally, as showed in Figure 4.30 inset b, there is a percentage of scattering at the interface between the vertical taper and the single mode waveguide. Probably, light is being radiated or reflected when passing from the SU-8 rectangular waveguide at the last part of stage 2 of the vertical taper to the SiO_2 and Si_3N_4 waveguide.

4.4.3.2 Coupling tolerance to misalignments

It is remarkable to mention that thanks to the increase in the in-coupling area, the light coupling with the commercial fiber optic was done in a much simpler and faster way as compared to the standard coupling by end-fire. A sweep in the horizontal alignment was performed to experimentally quantify the improvement. The fiber was positioned in the vertical taper in-coupling area where the maximum output power was obtained. From there, one-micrometer steps were taken on each direction while saving the intensity reported by the photodiode current. A similar experiment was performed using a reference single mode waveguide directly coupled by the light from a fiber. Figure 4.31 shows an acceptance waist of 8 µm when coupling to the reference single mode waveguide by end-fire (black dots, i.e. without vertical taper). In other hand, the vertical taper has an acceptance waist of **38 µm** as showed in the red plot in Figure 4.31. This represents an increase of 4.75 times in coupling tolerance to misalignments in the horizontal axis. With these alignment tolerances, it would be possible to automate the in-coupling mechanisms in order to use disposable cartridges. A static fiber source with

polarized light could focus the light to the input of the vertical taper on the chips which in turn could be correctly positioned through alignment marks between the disposable cartridge and the mechanical holder. In other hand, there is no reported improvement in terms of total output power or tolerance to vertical misalignments as observed in Figure 4.32. In this case, a vertical sweep with steps of 1 µm was performed experimentally and the PD current intensity recorded and plotted. Both curves have similar waists and peaks. As showed in the previous simulations, the advantages of the vertical taper could take place when using collimated or divergent beams which is our case.

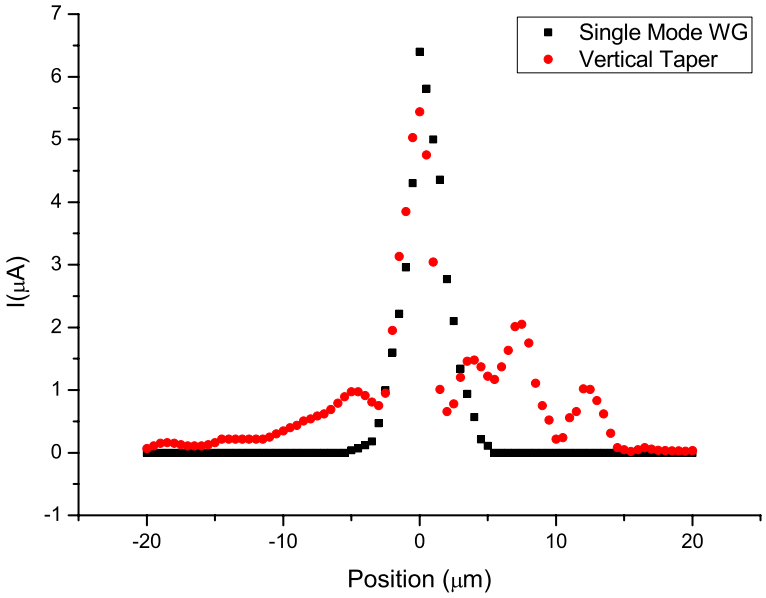

Figure 4.31 Sweep of the intensity output (photodiode current in µA) as a function of the horizontal misalignment between the fiber optic and the reference single mode waveguide *(in black,* coupling waist of 8 µm*)* and between the fiber optic and the vertical taper *(in red,* coupling waist of 38 µm*)*.

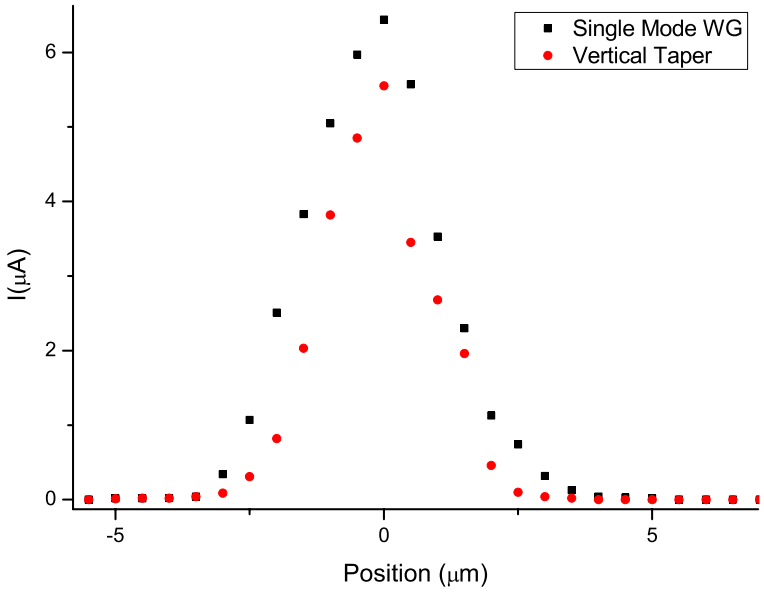

Figure 4.32 Intensity output as a function of the vertical misalignment between the fibre optic and the reference single mode waveguide (*black*, waist of 4 μm) and between the fibre optic and the vertical taper (*in red*, waist of 3 μm).

4.4.3.3 Sensor Calibration

As a proof of concept of the performance of the vertical taper approach, we have done a refractive index calibration of the BiMW sensor device. A calibration curve was calculated using the method described in section 2.5: by injecting four different concentrations of HCl at 30 $\mu Lmin^{-1}$ which correspond to minute variations of the refractive index on the sensing window (see Table 4.3).

Table 4.3 Refractive index difference from deionized water (n_{H2O}=1.3332) to different dilutions of HCl and the corresponding phase shift as measured in the interferometric signal.

HCl Concentration [Molar]	Refractive Index Difference [R.I.U.] [a)]	Phase Shift [2π rad]
0.5	0.051	9.38
0.25	0.00284	4.84
0.15	0.00202	2.60
0.1	0.00154	1.72

[a)] Reffractive Index Units

Computing and plotting the phase shift corresponding to each refractive index difference will provide us the calibration plot. The slope of this plot corresponds to the bulk sensitivity S_{bulk} intrinsic to the sensor, which is 2150•2π $radRIU^{-1}$. A LOD of $2.98•10^{-6}$

RIU is calculated for a system baseline noise of 0.1282% and visibility of 15%. There is a loss of one order of magnitude in the limit of detection when comparing to the BiMW sensor coupled by end-fire as compared to the vertical taper plus BiMW sensor. We attribute this decrease to the presence of SU-8 debris in the sensing window which could diminished the index contrast between the cladding and the core and, consequently, the visibility of both modes. Nevertheless, the LOD is in the same order that reported at the state-of-the-art for most evanescent wave sensors. In other hand, the possibility to use commercial SM-PM fiber optics to couple directly to the BiMW biosensor opens the possibility to automation and further lab-on-a-chip integration for commercialization of this BiMW technology.

4.4.4 Conclusions

A low-cost taper solution made out of SU-8 polymer for coupling visible light into nanometric silicon nitride photonic waveguides has been designed, simulated, fabricated and tested. Via simulations, it was foreseen that the vertical taper solution would be effective when coupling collimated or divergent beams. Besides, an increment of 4.75-fold in the horizontal tolerance to misalignment has been proved paving the way to automated coupling mechanisms. Moreover, SU-8 has been used for its fabrication at wafer level allowing mass production, low cost and fast fabrication, making it practical for the transition of the BiMW biosensor from the lab to be use in a disposable format for real diagnostic applications. As a proof of concept, the calibration curve showed a bulk sensitivity of $2150 \bullet 2\pi \bullet rad.RIU^{-1}$ and a LOD of $2.98 \bullet 10^{-6}$ RIU, which are very competitive values as compared to the state-of-the-art in evanescent wave sensing in a label-free format.

Even if the vertical taper has helped increasing the tolerance to horizontal misalignments, there is the possibility that light is not perpendicularly incident to the BiMW input plane. Light beams could be collimated and with some incidental angle with effects in the total in-coupling. An inverted taper could act as a guiding device while being fabricated following the standard BiMW microfabrication. Moreover, inverted tapers offer the advantage of smaller lengths as compared to other tapered approaches.

4.5 Inverted tapers

To our advantage, an inverted taper was previously designed as part of the stage 2 of the design of the vertical taper. The inverted taper was 920 µm long, 150 nm thick and it has

an output width of 3 µm. The taper will be etched directly in the single mode section so it will be a Si_3N_4 core structure (n_{core} = 2.0) placed on top of SiO_2 substrate (n_{subs} = 1.46) and surrounded by air media (n_{air} = 1.0).

4.5.1 Inverted taper design and simulation

Inverted tapers were simulated with nominal dimensions, however, when using only four modes the coupling efficiency was only 0.8%. It increased to 1% when using 20 modes. Propagation patterns were plotted and simulated as showed in Figure 4.33. The output intensity is plotted as a function of the incidence angle of a fiber optic (V_{tilt} and H_{tilt}) with characteristics discussed in 4.4.1.2, as showed in Figure 4.34. It is interesting to note that the tolerance to the incidence angle is as high as 4 degrees in both axes. All propagation simulations were performed using EME in Photon Design ®.

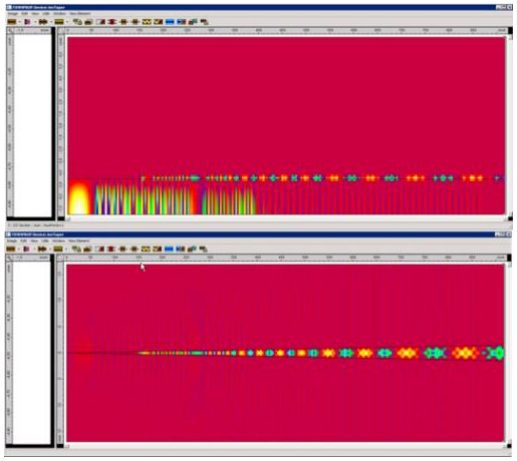

Figure 4.33 Simulated upper and lateral radiation patter of an inverted taper. Coupling efficiencies of 1% were obtained.

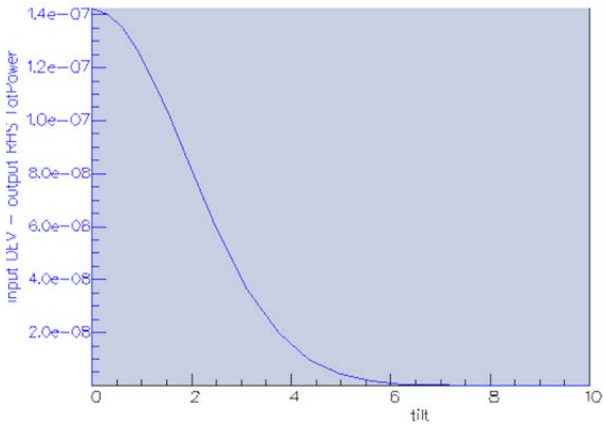

Figure 4.34 Inverted taper output power as a function of the incidence angle variation of a fibre optic beam (*total output power is in* $J \cdot m^{-2}s^{-1}$**).**

4.5.2 Inverted taper fabrication

The fabrication process is similar to the one depicted in Figure 4.25 just avoiding steps concerning the deposition, curing and etching of SU-8 (steps h to k) for the vertical taper. After fabrication, dicing and cleaning of the chips was required. A picture of the fabricated inverted tapers is showed in Figure 4.35.

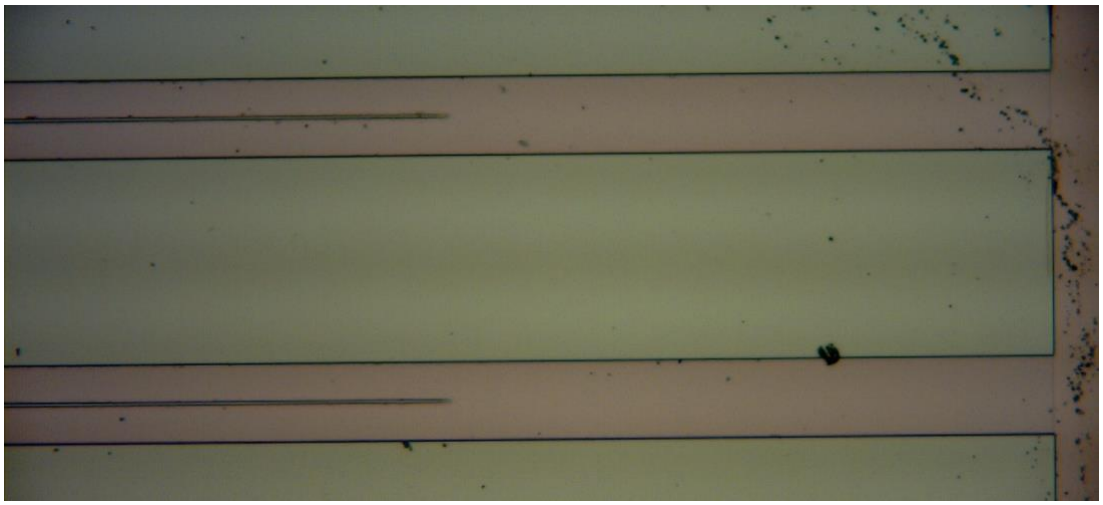

Figure 4.35 Picture of the tips of the Si_3N_4 inverted tapers fabricated on top of a SiO_2 layer.

4.5.3 Experimental evaluation of the inverted tapers

Experimentally, inverted tapers were characterized by end-fire coupling of a fiber optic as showed in section 2.4.3.1.3, with power of 1.41 mW (1.05 mW for TE polarized component and 50 μW for TM) at the input of the inverted taper and the input of a BiMW (without taper). The output power was 3.92 μW (24.3 dB loss) at the output of the BiMW reference and 1.90 μW when adding an inverted taper (27.4 dB loss). By comparing the differences, an insertion loss of 3.14 dB was calculated. Moreover, as a proof of concept, different concentrations of HCl were injected to calculate the calibration curve as showed in Figure 4.36. A bulk sensitivity of $2233 \cdot 2\pi \cdot radsRIU^{-1}$, visibility of 26.01% and a base noise of 0.38% were obtained and a LOD of $4.9x10^{-6}$ RIU was calculated. Again, the worsening of the LOD as compared to our standard BiMW sensors is attributed to the SU-8 debris clotting the sensing area.

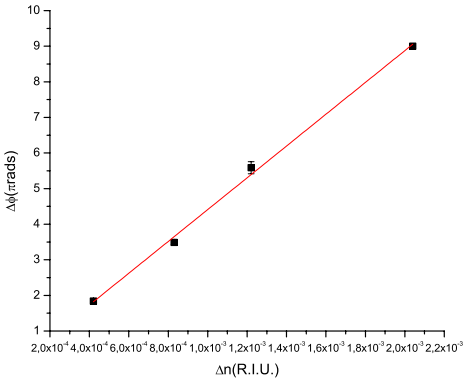

Figure 4.36 Calibration curve of a BiMW nanointerferometric biosensor with an inverted taper as in-coupling device using end-fire coupling and PD readout.

Moreover, a sweep of the incidence angle was performed at two different laser diode current intensities (I_{LD}): 150 mA and 200 mA. The response was similar to the simulated ones in the previous section, showing tolerances to up to 4 degrees as showed in Figure 4.37.

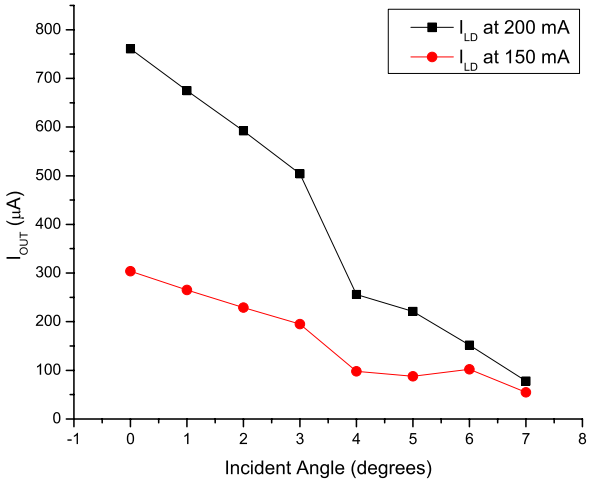

Figure 4.37 Experimental evaluation of the incidence angle tolerance of the inverted taper with two different laser diode driving current intensities, at I_{LD} = 200 mA and I_{LD} = 150 mA.

4.5.4 Conclusion

An inverted taper could increase the in-coupling tolerance to incident angle misalignments of up to 4 degrees. Even if insertion losses of 3 dB are added as compared to direct end-fire coupling of a reference bimodal waveguide, no significant changes in bulk sensitivity and LOD were observed. In other hand, this solution would not require any extra material and only one extra photolithographic mask level for fabrication.

Moreover, since no more SU-8 would be required, the chances of clotting of the sensing window will be reduced.

4.6 Chapter conclusion

A vertically stacked taper has been designed, simulated, fabricated and characterized. It could help increasing the input area to 10 µm x 6 µm instead of the actual 150 nm x 3 µm. The acceptance waist was increased to 38 µm instead of the 8 µm waist of the single mode waveguide. This way, larger macrometric light sources could be easier in-coupled paving the road towards an automated in-coupling mechanism. By simulating divergent, coherent and convergent light beams being coupled to a single mode waveguide and compared when coupled to the vertically stacked taper, it has been observed that the taper could couple more power only in the cases of using coherent and divergent light beams.

Experimental studies showed an insertion loss of 2 dB. In terms of fabrication, the vertically stacked taper was made out of SU-8 with standard CMOS technologies adding three photolithographic mask levels to the actual fabrication process of the BiMW.

In the process, an inverted taper has been also designed, simulated, fabricated and characterized. The advantage of the inverted taper is its wide acceptance angle (~7 degrees in the vertical tilt) while adding only 3 dB of insertion loss. In terms of fabrication, it was only required to add one mask level to the actual fabrication process of the BiMW. Moreover, no extra materials are required.

The LODs and sensitivities are not compromised in any case by showing responses in the typical range of a standard BiMW nanointerferometric biosensor. Once the proper interferometric signals S_R are obtained, it is necessary to quantify the phase shift $\Delta\phi$, however, automatization of the signal extraction would require an extra system, a modulation system.

5 CHIRP MODULATION SYSTEM

"Sheets of sound. Well, that was when I got tired of certain modulation. Like when you want to get back to C, and you've got to go to D and then G and then C. I was fooling around with the piano, and I figured out some other way to do it."

- *John Coltrane*

This chapter provides an introduction to the theory behind the modulation system. Modulation systems are tools to overcome a variety of problems innate to interferometric signals. A comparison with other modulation solutions is provided. Then, the design, simulation, experimental evaluation and advantages of a proposed chirp modulation system is showed.

As discussed in section 1.3.1, due to the periodic nature of interferometric signal, there are challenges to overcome:

Sensitivity fading. Since the sensitivity is a function of the rate of change of the effective refractive index over the rate of change of either the refractive index of the bulk or the thickness of the biological thin layer, the sensitivity will vary along with the measurement, becoming maximum at the quadrature points and minimum at the curve extremes. Thus, different responses will be obtained depending in the initial conditions of the detection.

Directional and fringe order ambiguity. Since the intensity fluctuation is also periodic, it is not possible to determine the direction of the phase change from the final intensity value alone. If only one intensity value is measured, any $\Delta\phi_m' = \Delta\phi_m + 2\pi \bullet k$, with k being an integer number, is a similarly possible solution.

Relative measurement. When a complete period of the interferometric signal is not induced by the refractive index change in the sensing area, a reference is required in order to know the fringe period equivalence to a 2π•rad cycle.

Additionally, a **direct linearization** of the relative phase change would simplify the signal readout facilitating the interpretation of the detection event obtaining plots more similar to the typical sensograms instead of interferograms (see Figure 5.1). This way we are avoiding subjective errors that could occur when manually calculating the phase shift by counting fringes.

Some modulation systems could exploit electro-optic [90], thermo-optic [91], magneto-optics [92], or liquid crystals [93] phenomena but they rely on bulky electronic equipment or complex fabrication processes.

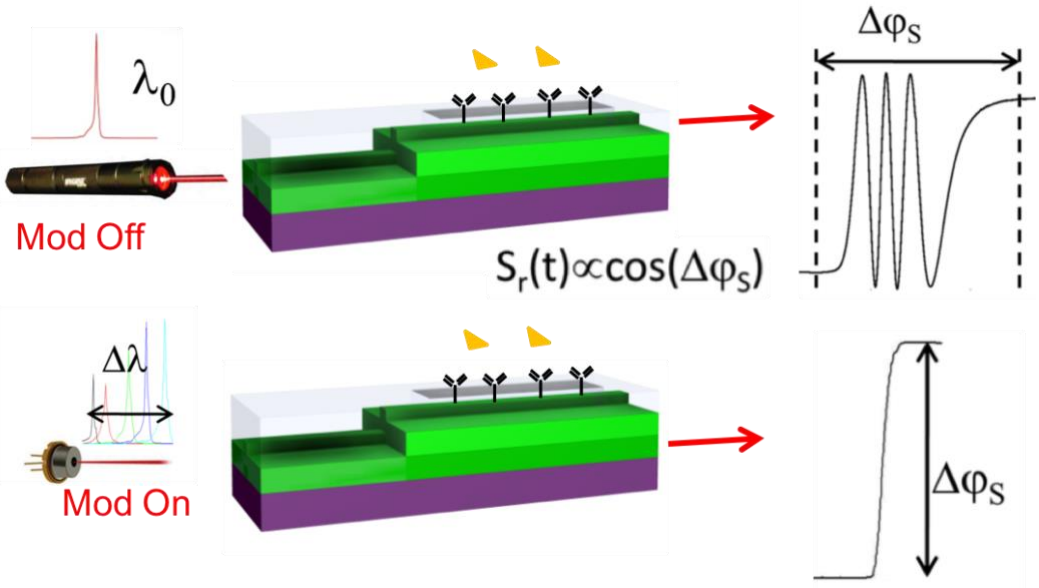

Figure 5.1 Comparison of the linearization of the BiMW nanointerferometric biosensor output signal through the direct phase shift extraction when employing modulation systems (Mod On).

An elegant solution is the excitation of harmonics in the waveguide with the intention to perform a phase extraction through the FFT deconvolution of the n-order Bessel coefficients of the output signal spectra as proposed in our group by Dante et al [55].

In this scheme, a low-cost commercial laser diode (LD) was modulated ±2 nm by controlling its driving current. After finding the correct frequency for the waveguide harmonics excitation, it is necessary to guarantee similar peak intensities of the third and second harmonic. After a Fast Fourier Transform (FFT) deconvolution, the linear

response of the biosensor is obtained. However, this technique required the individual analysis of the visibility (signal amplitude) inherent to each BiMW sensor, previously to any experiment in order to ensure that we can get the maximum sensitivity (relative measurement). Additionally, it requires the completion of at least a whole period of phase shift in order to determine the fringe and direction orders. The sensitivity is related to the initial phase shift between both modes when performing a measurement. The sensitivity is enhanced when the initial phase difference is close to zero, i.e. the output is at the quadrature point [94]. However, thickness variations across chips demand larger wavelength excursions in order to excite the harmonics inside the waveguide, due to the critical effect [59,95]. Wavelength excursions larger than 3 nm will require more expensive and bulky equipment resulting unrealistic for LOC applications. Furthermore, this technique requires the generation of an initial change of the refractive index in the sensing area in order to ensure non-zero sensitivity and to recognize a whole phase period of 2π•rad.

Another alternative is to employ white-light sources to solve the limitations of single-wavelength sensors [96]. The ambiguity and signal fading can be avoided by the use of multiple wavelengths. Each wavelength is affected different by the same refractive index variation. Discrete Fourier Transform Deconvolution was applied to direct and unambiguously retrieve the phase information from the sinusoidal transmission curves for each polarization [97]. This modulation was implemented in an all-silicon monolithic MZI biosensor [98].

We propose a chirp modulation system to overcome the challenges regarding interferometric signals previously mentioned. By modulating the driving current of low-cost LDs, an intensity and wavelength sweep of the output signal could be observed (chirp sweep). If enough wavelengths are injected, some of them will be located at the maximum sensitivity point (quadrature point). Even better, if a whole 2π•rad cycle could be completed, it could provide useful information of the device and no more preliminary changes of the surface refractive index will be required. Moreover, by reading the modulated S_R it is possible to know if the intensity distribution across photodiode sections is even (i.e. the two-sections photodiode is vertically centered). Thus, by adding micrometric positioning of the two-sections photodiode we could ensure a symmetric placement of the read-out photodiode thus obtaining an interferometric signal centred and ensuring the maximum sensitivity. This way, the main problems of sensitivity fading, signal ambiguity and relative measurement could be surpassed.

5.1 Design and simulation

The Bimodal waveguide section has been optimized to ensure the excitation of the fundamental TE_{00} and the first order mode TE_{10}, which has a larger evanescent tail. Both modes will travel with different propagation constants experiencing different phase shifts for the same change of refractive index on the cladding (n_{sens}) of the waveguide. The interferometric phase change is given by

$$\Delta\varphi_S(\lambda, n_{sens}) = \frac{2\pi L}{\lambda}(N_{eff}^S(\lambda, n_{sens}) - N_{eff}^R(\lambda, n_{sens})), \qquad (5.1)$$

where L is the length of the sensing waveguide, λ is the wavelength of the signal guided in the waveguide and N_{eff}^R and N_{eff}^S are the effective refractive index of the fundamental and first order mode (reference and sensing respectively). Since equation 5.1 is a function of the wavelength, each wavelength will experience a different phase shift due to different effective refractive indexes. The interferometric signal S_R will be given by

$$S_R(t) = \frac{I_{up} - I_{down}}{I_{up} + I_{down}} \approx Vcos(\Delta\varphi_S(t)), \qquad (5.2)$$

where V is the fringes amplitude (visibility factor) and I_{up} and I_{down} are the currents measured by the upper and lower sections of a two-section photodiode. Since S_R is normalized to the total intensity propagating across the device, it will result in shielding to input intensity variations due to laser driving current fluctuations or mechanical instabilities. The bulk sensitivity S_{bulk} understood as the change rate of S_R per change of n_{sens}, would be given by

$$S_{bulk} = \frac{\partial S_R}{\partial n_{sens}} = \frac{\partial S_R}{\partial \Delta\varphi}\frac{\partial \Delta\varphi}{\partial n_{sens}}. \qquad (5.3)$$

As explained, sensitivity suffers of periodic fluctuations due to the sinusoidal nature of S_R becoming maximum at the quadrature point and minimum at the curve extremes. Multiple wavelengths will be periodically swept with the anticipation that some of them will be at the quadrature point. If enough wavelengths are swept, it should be possible to observe a whole period of 2π letting us to overcome the signal ambiguity. For simulation purposes, the self-consistency transcendental equation has been numerically solved using scripts in iPython Jupyter Notebook. In order to validate this assumption, we start with computational studies to numerically solve the self-consistency condition for TE polarization:

$$tan\left(\pi\frac{d}{\lambda}sin\,\theta_m - m\frac{\pi}{2}\right) = \sqrt{\left(\frac{sin^2\bar{\theta}_c}{sin^2\theta_m} - 1\right)}, \qquad (5.4)$$

where d is the waveguide thickness, λ is the wavelength, θ_c is the critical angle and θ_m is the bouncing angle of the rays being guided if $\theta_m < \theta_c$ of the m mode. We can then calculate the propagation constant $\beta_m = n_1 k_0 \cos\theta_m$, where n_1 is the core refractive index, and finally calculate N_{eff}^R and N_{eff}^S for different wavelengths in iPython Notebook as well by numerically calculating the minimum square error of numerical approximations to solutions of the self-consistency condition. With the aim to validate the software, we start computing the energy distribution across a 1 µm width waveguide (to properly visualize the interfering modes) and λ of 660 nm, as showed in Figure 5.2.

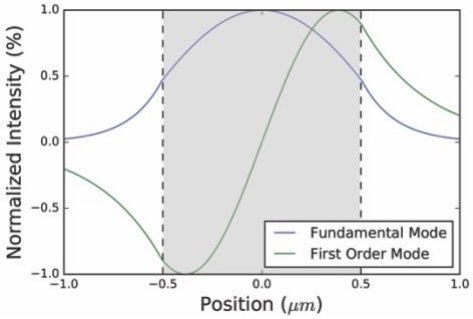

Figure 5.2 Normalized intensity distribution of the first order and the fundamental mode of light at 660 nm wavelength in a simulated waveguide of 1 µm width.

Three different wavelengths were simulated: 659.5 nm, 660 nm and 660.5 nm. Each wavelength will show a different phase shift according to the position (or length) of the optical path (L = 15 mm, plus the length increment). Figure 5.3 shows the plot of the interferometric signal as a function of the optical path length increment for the three mentioned wavelengths. Each one of them has a different phase shift at similar locations of optical lengths. Thus, some of them will be in the maximum, others in the minima and to our advantage, others will be in the quadrature point maximizing the sensitivity. In this case, 1 nm wavelength excursion seems to produce a blue shift close to π•rad. Wavelengths excursions of 2 or 3 nm should be enough to cover a whole 2π•rad.

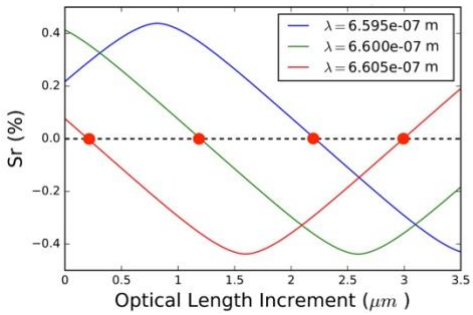

Figure 5.3 Simulated interferometric signal in percentage as a function of the position at the end of the optical path (i.e. optical length) for 0.5 nm wavelength excursion around 660 nm. Quadrature points where sensitivity is maxima are showed in red.

Firstly, it is worth to mention that the first simulations were run with the aim to validate the assumption of the shift of the interferometric signal S_R as a function of changes of the optical path. The optical path as given by equation 5.1, is a function of the length of the biosensing waveguide L, the refractive index of the sensing area and the wavelength of the employed signal. All these parameters are physically permanent except the signal wavelength. But, what if we could employ the defect of some low-cost laser diodes (LD) in order to generate multiple wavelengths? Some of these wavelengths would be located at local maxima, others at local minima and some of them would be in the quadrature point. But firstly, it would be required to implement the setup and characterize some of these LDs.

5.2 Implementation

5.2.1 Laser Diode Characterization

Some Fabry-Perot laser diodes can exhibit the defect of wavelength excursions of a few nanometers as a function of the variation of the diode driving current (I_{LD}). Thus, while varying (modulating) the I_{LD} we can obtain a wavelength and intensity sweep. The spectra as a function of I_{LD} variations of 1 mA between 80 and 200 mA were performed in a LP642 LD (Figure 5.4), in a LP660 LD (Figure 5.5) both of them from Thorlabs®, and a ML101J27 LD from Mitsubishi® (Figure 5.6). All of them boxed in a TCLDM9 cooled mount for LDs and controlled by an ITC4005 laser controller by Thorlabs®. Meanwhile, the spectra were acquired and saved in separated files using the spectrometer FLMT01692

(FLAME-S-VIS-NIR-ES) from Ocean optics. The data was post-processed using scripts developed in iPython Notebook.

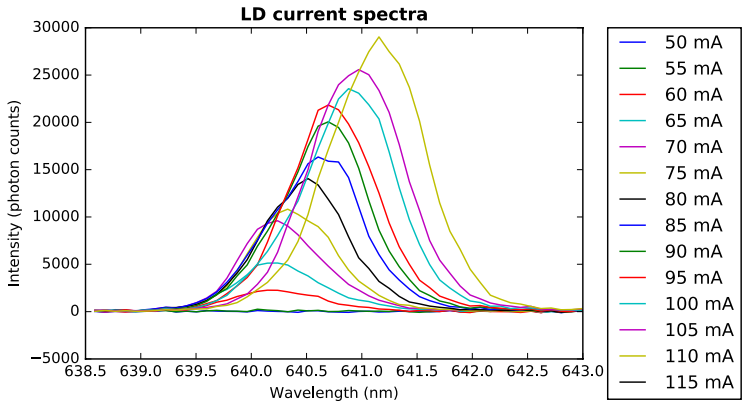

Figure 5.4 Emission spectra of a LP642 laser diode from Thorlabs ® as the driving current is varied between 80 and 200 mA.

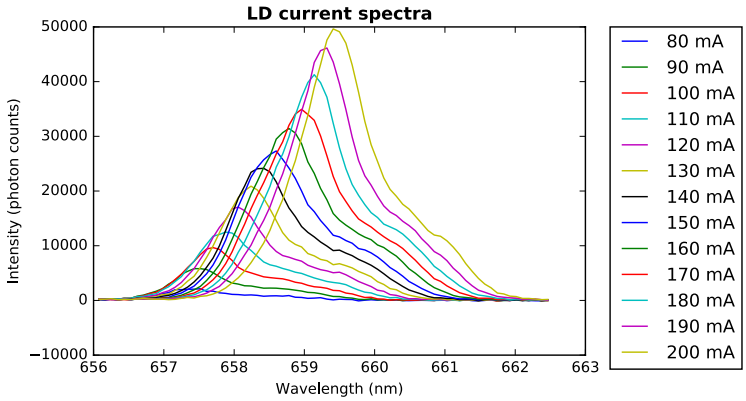

Figure 5.5 Emission spectra of a LP660 laser diode as the driving current is varied between 80 and 200 mA.

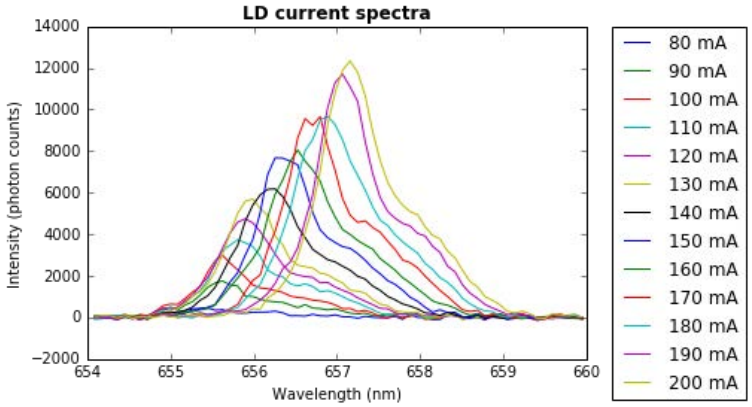

Figure 5.6 Emission spectra of a Mitsubishi® ML101 J27 laser diode as the driving current is varied between 80 and 200 mA.

A 1 nm wavelength excursion was observed in the spectra of LP642 and ML101J27, while 2 nm were observed in the spectra of LP660.

In order to test the proposed chirp modulation, an optical setup using butt-coupling and PD readout as depicted in Figure 5.7 was employed. The Laser Diode ML101J27 from Mitsubishi® is boxed in a TCLDM9 cooled mount for laser diodes controlled by a ITC4005 laser diode controller, all of them from Thorlabs®. The collimator lens is an aspheric lens with NA=0.5 and f = 8.0 mm (C240TME-B) embedded in a CXY1 micrometric positioner and the polarization dependent isolator is the model IO-3D-660-VLP. The polarizer is an LPVISB050-MP from Thorlabs. Finally, a 40X objective from Achro® is used to butt-couple the light into the waveguide. A temperature control system as described in section 2.4.2 is employed. Figure 5.8 shows a photograph of the implemented setup.

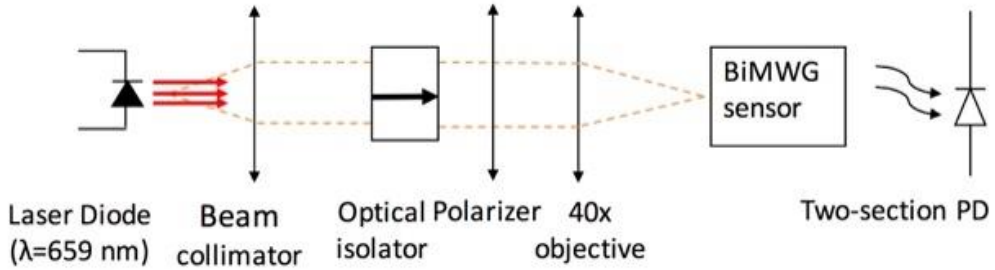

Figure 5.7 Optical setup for chirp modulation evaluation of BiMW sensors.

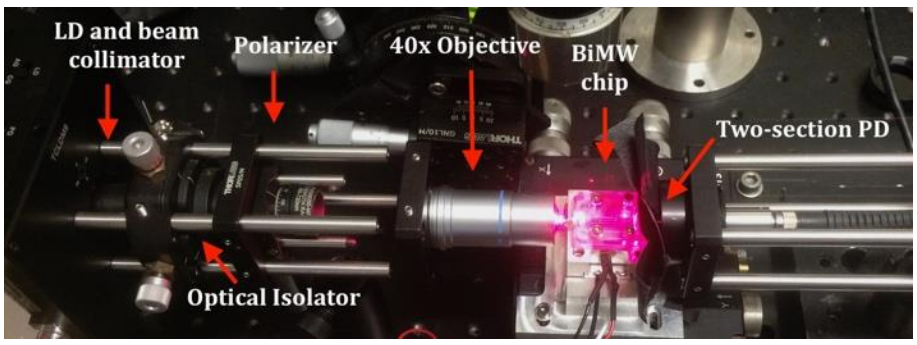

Figure 5.8 Photograph of the optical setup for evaluation of the chirp modulation in BiMW sensors.

Labview 2014® and an acquisition card USB6361 from National Instruments were employed to custom-made an application to control the waveform, frequency, amplitude and offset of the modulation signal generated by software ($I_{LD} = I_{base} + I_{mod}$). The software architecture has been described in section 2.4.5. The modulated driving current I_{mod}

generated in the card is sent to the modulation input of the ITC4005 LD controller allowing us to send a feedback loop reading the actual I_{LD} in the same card. Simultaneously, we acquire I_{up} and I_{down} amplified by a PDA200C from Thorlabs® from the PD (S4349 from Hamamatsu®) connected to the USB6361 acquisition card. All post processing was done in iPython Jupyter Notebooks for further and more detailed investigation of the data.

5.3 Experimental results

Firstly, different waveforms, frequencies, amplitudes and offsets were evaluated. We start trying with modulations of 30 Hz, 10 Hz, 5 Hz, 1 Hz, 0.5 Hz, 0.1 Hz since the biomolecular interactions in biosensing are in the order of seconds, slow frequencies can be employed. The modulated I_{LD} should cover the whole working range of the LD with the aim to generate the wavelength sweep of 2 or 3 nm, in the case of the ML101J27, from 80 to 210 mA, having less noise in the region between 100 and 200 mA since it is defined as the optimal working range in the manufacturer specifications. The offset parameter might help to increase or decrease the DC component of the modulated current. Concerning the waveforms, sinusoidal, sawtooth and triangle waveforms were tested, being sawtooth and triangle the preferred waveforms in order to facilitate the data post-processing. Figure 5.9 shows a picture of the implemented chirp modulation system in a BiMW sensor. We are using a PD with micrometric positioning as described in section 2.4.1 to obtain an even intensity distribution between I_{up} and I_{down}. A screenshot of one sawtooth cycle of 0.5 Hz between 80 and 200 mA and without offset can be seen in Figure 5.10.

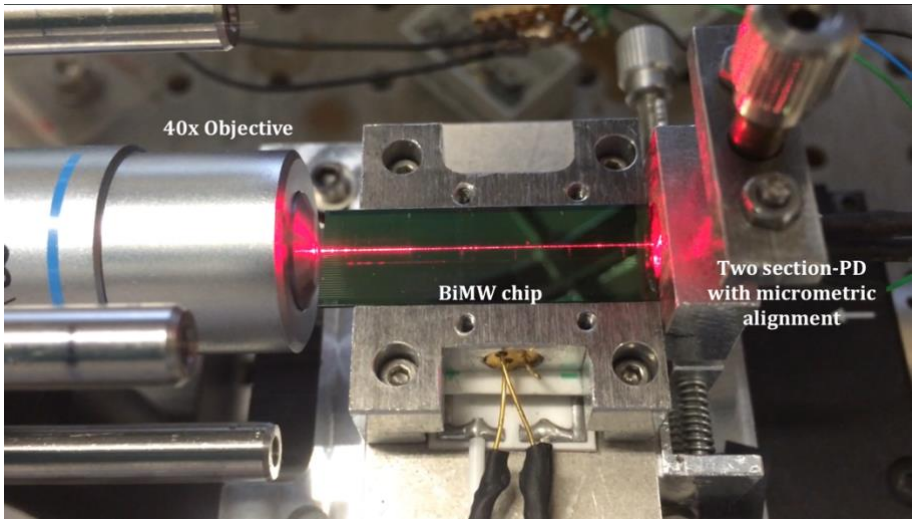

Figure 5.9 Coupled chip with chirp modulation.

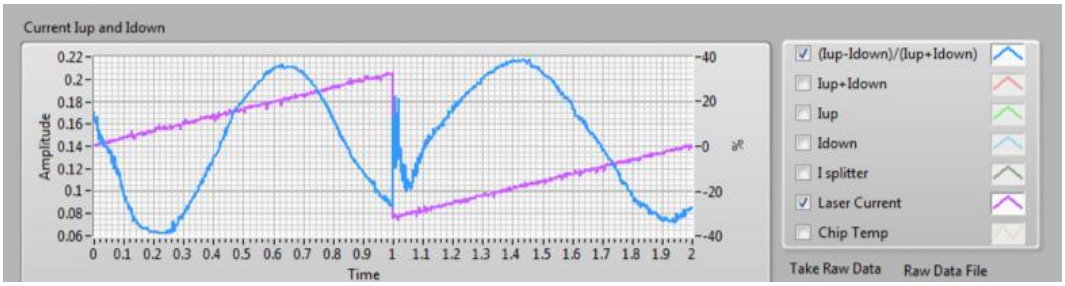

Figure 5.10 Software implemented in Labview 2014® to control the laser diode driving current and calculation of the S_R (blue line) as function of the I_{up} and I_{down} read in the PD. The purple line is the laser diode driving current I_{LD} being sweep with a sawtooth waveform at 0.5 Hz, from 80 mA to 200 mA.

5.3.1 Evaluations as a biosensor

For calibration purposes, four concentrations of HCl were injected following the process described in section 2.5. For comparison, a series of successive injections was performed without using modulation and counting fringes manually; and a second series of injections was performed using modulation. Post-processing the data in iPython notebook allowed us to choose which index (1024 samples per second) to use for plotting the S_R over time, being able to choose the maximum or minimum sensitivity point. Table 5.1 shows the refractive index of the four concentrations injected and the phase shifts obtained when situated in the Q-point and when using a manual approach without modulation. By plotting phase shift as a function of the refractive index difference between running water and the HCl solution, a calibration curve is calculated. Its slope corresponds to the S_{bulk} intrinsic to each sensor.

Table 5.1 Phase shift corresponding to different changes of refractive index.

HCl Concentration [Molar]	Refractive Index Difference [R.I.U.] [a)]	Phase Shift without Modulation [π rad]	Phase Shift with Q point [π rad]
0.5	0.00510	8.60186	9.115
0.25	0.00284	4.75293	4.82125
0.15	0.00202	3.12785	2.96715
0.10	0.00154	2.55445	2.39075

a. Refractive Index Units. Measured with Rudolph refractometer J57.

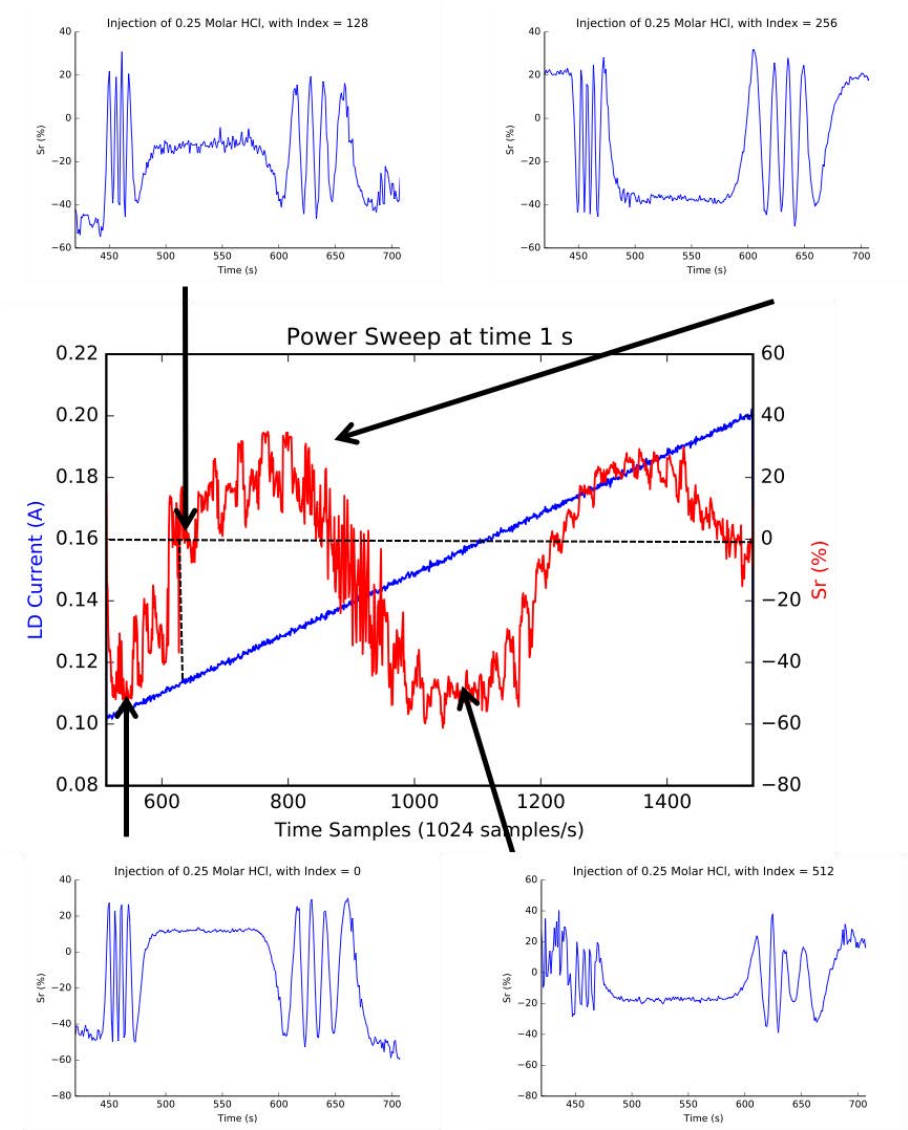

Figure 5.11 Injection of 0.25 M HCl. The central plot shows the interferometric signal S_R (right axis) and the modulated laser driving current I_{LD} (left axis) as a time snapshot collecting 1024 samples per second. Then, by choosing a given index, the S_R can be reconstructed as located in a point of maximum or minimum sensitivity.

Without modulation, a bulk sensitivity S_{bulk} of $1726 \cdot 2\pi radRIU^{-1}$ was calculated. However, when choosing only the data points where the sensitivity is maxima, i.e. the quadrature point, a S_{bulk} of $1926 \cdot 2\pi radRIU^{-1}$ was calculated instead, representing an improvement of 11.58% in terms of bulk sensitivity and a LOD of 2.98×10^{-6} RIU.

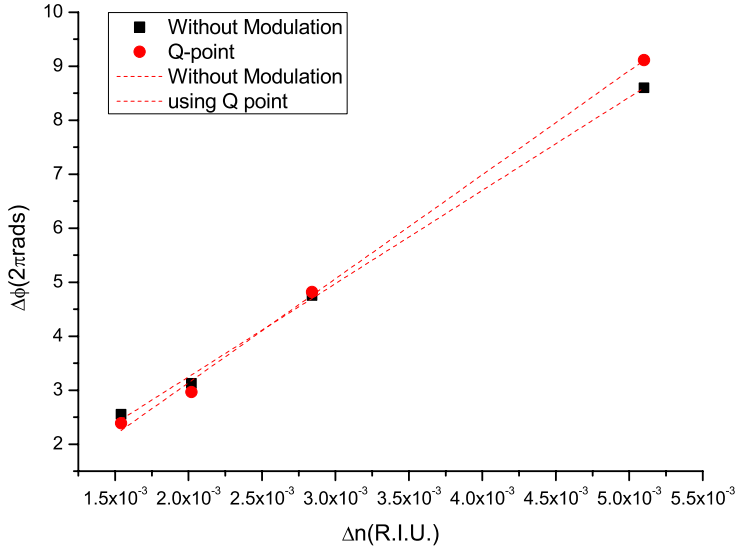

Figure 5.12 Comparison of both calibration curves when using a regular approach and when situated in the Q-point.

It is worth to mention that the SNR is proportional to the LD current, resulting in better interferometric signals when situated in the right side. The important thing to notice here, is not the amount of increase in terms of bulk sensitivity (12%), but the fact that, it was achieved only by carefully choosing data to be post-processed when employing this modulation.

5.3.2 Direction and Fringes Ambiguity.

With the aim to test different statistical solutions, all data was post-processed using iPython Notebooks. The first algorithm is a correlation between the initial interferometric signal S_{R0} and the consecutive read signals. The phase difference between both is plotted over time. The second statistical approach is the direct extraction of the angle in radians between two signals with similar frequencies:

$$\Delta\varphi = cos^{-1}\frac{S_R \bullet S_{R0}}{|S_R|\,|S_{R0}|}, \qquad (5.5)$$

where S_{R0} is the interferometric signal previous to the change of the refractive index in the sensing area (green fitted line in Figure 5.16). The blue or red shift can be observed in real time. Since the length of a period of the S_R is already known, the phase shift in relation to the initial state S_{R0} can be computed and plotted. This shift can be below 2π•rad, overcoming the problem of relative measurement, fringes and direction

ambiguities related to interferometric signals. Figure 5.16 shows the evolution of the S_R over time.

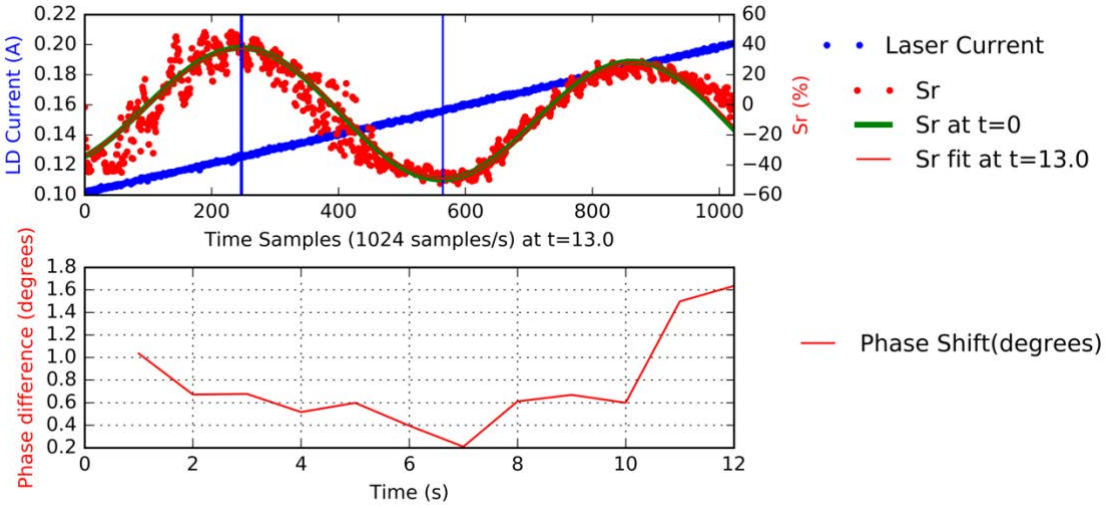

Figure 5.13 Phase extraction of a modulated S_R. The green solid line corresponds to S_{R0}, while the red dots are real time data. The I_{LD} is showed in blue varying from 100 to 200 mA. The phase shift is plotted below as a function of time. The red line shows the angle difference between S_R and S_{R0}. This is a screenshot at time t =13 s after the injection of a 0.05 M HCl solution.

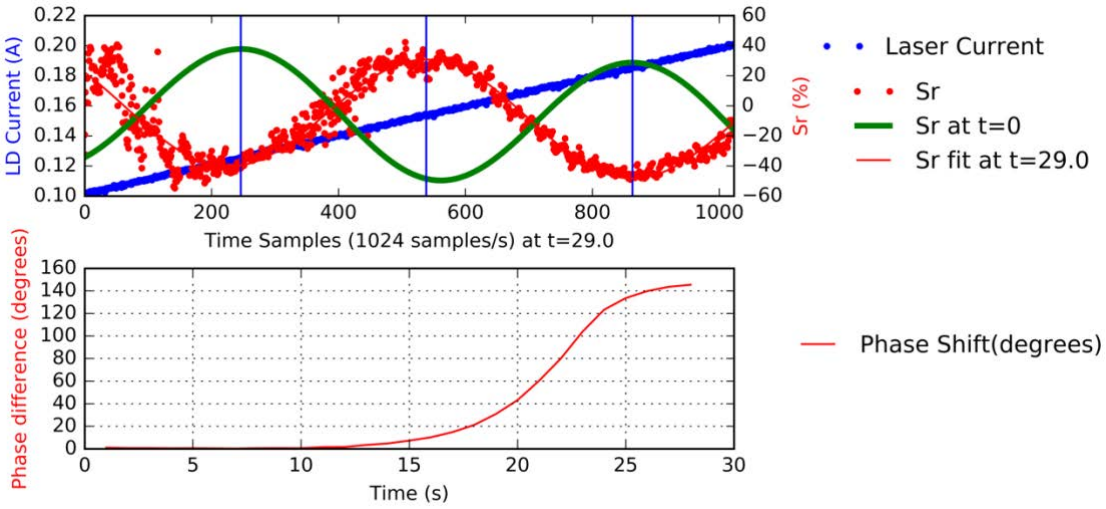

Figure 5.14 Screenshot of the phase extraction of a chirp modulated BiMW interferometer at t = 29 s after the injection of 0.05 M HCl solution.

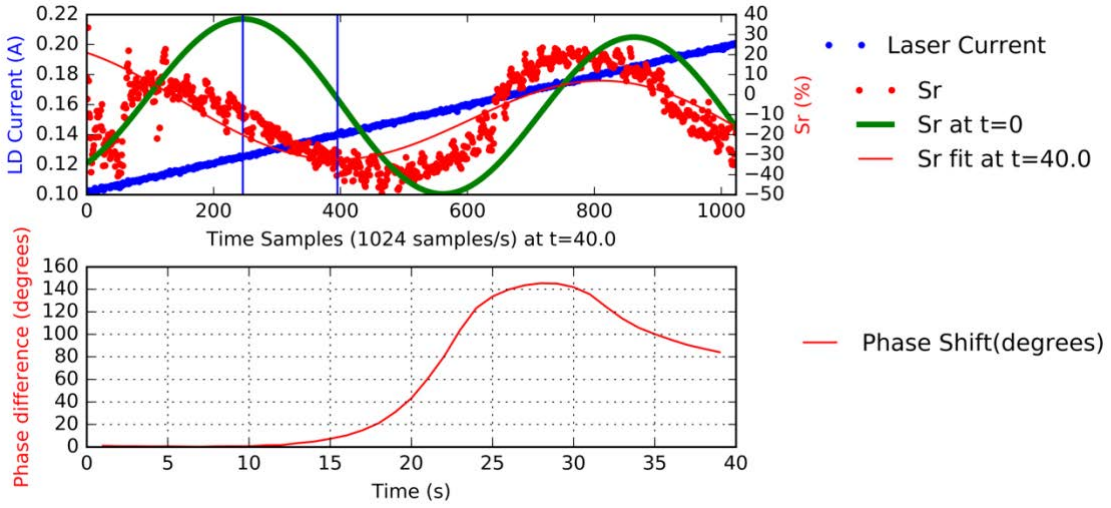

Figure 5.15 Screenshot of the phase extraction of a chirp modulated BiMW interferometer at t = 40 s after the injection of 0.05 M HCl solution.

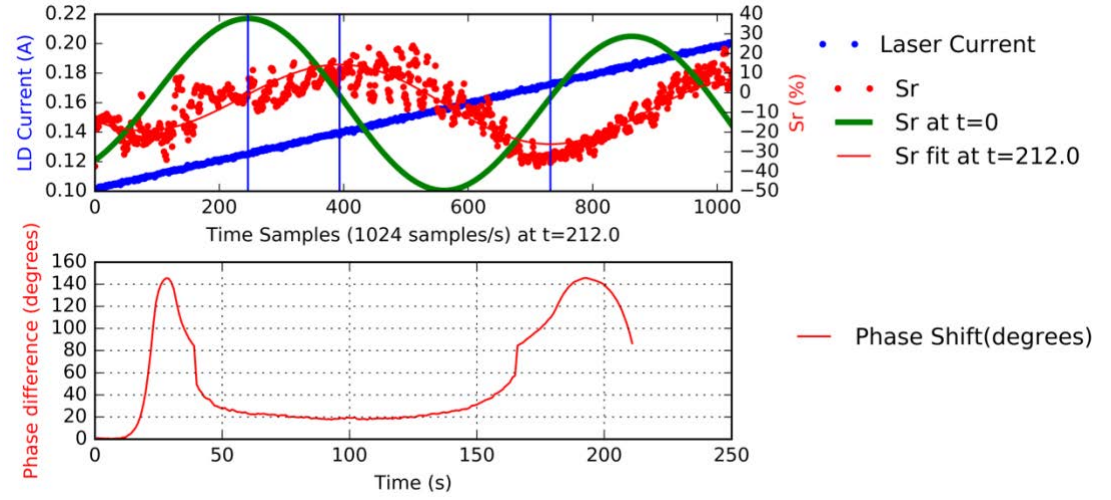

Figure 5.16 Screenshot of the phase extraction of a chirp modulated BiMW interferometer at t = 29 s after the injection of 0.05 M HCl solution.

Among the advantages of this method are: the blue or red shift can be observed in real time; knowing the peak-to-peak separation of the fitted Sr at t = 0, it could be possible to perform detections below π•rad and the noise reduction due to the number of adjustment points.

5.4 Conclusion

A chirp modulation system has been implemented for BiMW biosensors. The visibility inherent to each bimodal waveguide biosensor can be estimated without varying the refractive index on the sensing area, i.e. without injecting any sample.

This exploration with multiple wavelengths will provide useful information as the visibility factor, the period length and the S_R frequency. It was possible to only use data obtained from the Q point to reconstruct the S_R obtaining a 11.58% bulk sensitivity enhancement. In other hand, relative measurement problems are surpassed by implementing the chirp modulation allowing us to perform measurements below a complete 2π•rad period.

Thus, the sensitivity fading has been solved by selecting only data from the Q point to reconstruct the S_R.

It is worth to mention that the software has been implemented in such a way that both, the all-optical phase modulation previously implemented in our group can actually coexist with the new chirp modulation system. This will help to directly measure low concentrations but for real life applications, multiple biomarkers are required to be simultaneously read.

6 MULTIPLEXED BIOSENSING

"Opportunities multiply as they are seized."

- *Du Mu*

This chapter provides an introduction to the multiplexing requirements for biosensing. Moreover, different possible solutions are simulated in order to finally select one for its fabrication and experimental evaluation. Read-out mechanisms are a challenge for multiplexed detections. A proposed software-based readout mechanism is described, characterized and compared with other readout systems. Finally, an experimental demonstration of multiplexed capabilities is presented.

In the case of clinical diagnostic, multiple biomarkers are required as vectors or indicators of particular diseases in order to effectively diagnose some complex illnesses. Even if screening of multiple biomarkers could be done employing detection arrays as described in Figure 6.1, some diseases biomarkers require very low LODs. Even worst, the sample analysis time and complexity increases as the number of biomarkers does as well.

Thus, taking advantage of the high sensitivity and easiness of fabrication of the BiMW nanointerferometric biosensor, it is desired to add multiplexing on-chip capabilities. As a first option, a commercial 1x8 splitter chip used to in-couple a regular BiMW chip group to an 8 waveguide biosensors group with the aim to test the resolution of the system, and the feasibility of the approach. With the goal of simultaneously detect 8 BiMW biosensors, a software for multiplexed CCD detection is implemented in Labview® as described in section 2.4.5. Since the selected readout method is the CCD detection, its validation by comparing calibrations of the same BiMW nanointerferometric biosensor against PD detections are showed. Then, due to the success, it is decided to incorporate the splitting devices to the standard chips by fabricating them in one single chip at ICTS clean room facilities of the Microelectronics Institute of Barcelona (IMB-CNM-CSIC), but previously, IO beam splitters must be designed, simulated and after choosing the most suitable to our needs, fabricated and characterized.

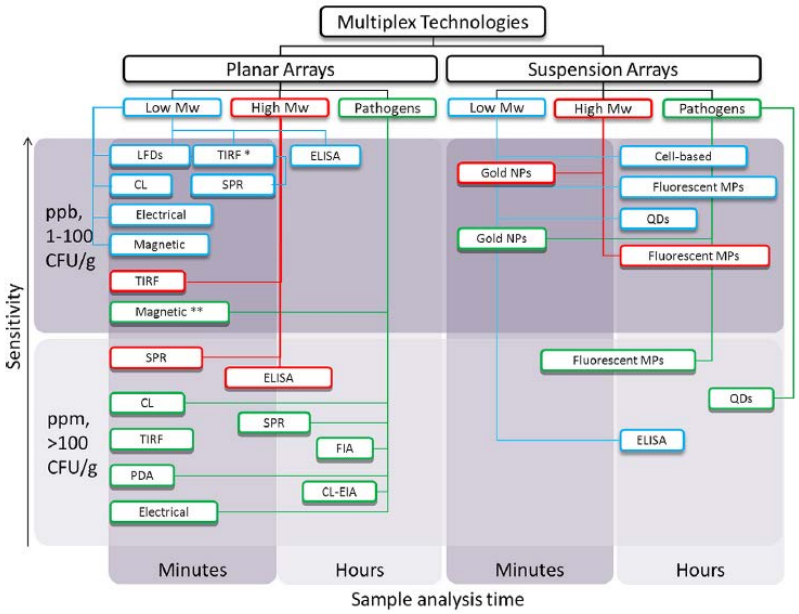

Figure 6.1 Multiplex bioanalytical methods for clinical monitoring using array techniques [99]**.**

As mentioned, we started by coupling a commercial chip to a regular BiMW nanointerferometric biosensor group with 8 biosensors as a first approach. Commercial multiplexers are available in the telecom industry. The only problem is that the majority of them are out of the visible range. *XioPhotonics* (now *Lionix*™) has commercialized 1 to 8 splitters in the VIS-range sold as "Broadband Splitter and Fringe Pattern Generator". Figure 6.2 shows a picture of a commercial splitter.

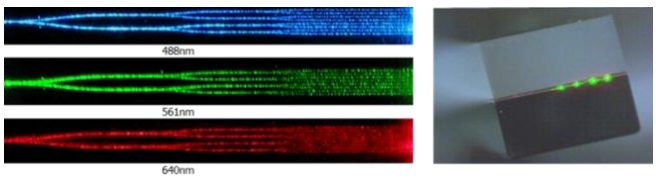

Figure 6.2 Commercial 1 to 8 splitter by Xio Photonics (now Lionix™).

With the intention to perform a simultaneous calibration of all sensors, it is required to develop a CCD multiplexed readout method based in the one described in section 2.4.3.2.3 and then integrating it to the architecture of the general software as described in section 2.4.5.

6.1 Validation of software for multiplexed CCD detection

As it has been previously explained in section 2.4.3.2.3, an algorithm for multiplexed detection using CCD has been implemented. In order to validate the software for

multiplexed CCD detection and to ensure that no significant loss of resolution is added to the system, a sensor calibration of a single regular BiMW nanointerferometric biosensor was performed using a fibered LD end-fire in-coupling, while testing the readout mechanisms: a single PD detection, CCD detection with 40X objective and CCD with 10X objective. The CCD camera required in order to include all 8 outputs with a 10X objective at the same time must have a dimension of 3" (CCD model DCU224M from Thorlabs®, 1280x1024 pixels, pixel size of 4.65 µm x 4.65 µm).

6.1.1 Photodiode readout

In order to perform a bulk calibration of the sensor, four different concentrations of HCl solutions (0.5 M, 0.25 M, 0.15 M, 0.10 M) were successively injected by triplicate as described in 2.5. A bulk sensitivity of 2460•2π•radRIU^{-1} was calculated and a LOD of 5.75x10^{-7} RIU was estimated with a visibility value of 36.85% and a base noise of 0.069%. Figure 6.3 shows the estimated calibration curve with PD detection.

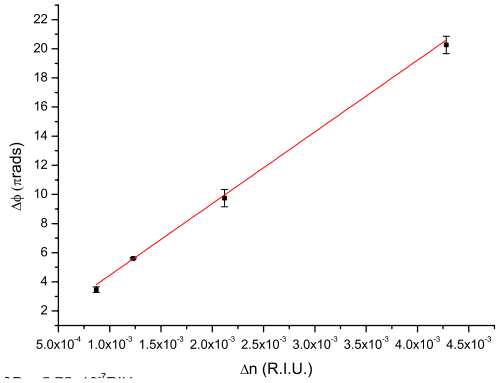

Figure 6.3 Calibration curve with analogue PD obtaining a LOD of 5.75x10^{-7} RIU.

6.1.2 CCD with 40x objective

By swapping the PD holder with the 40x objective + ND filter + CCD, up to two spots are visible as showed in Figure 6.4. The spot size is large enough and two ROIs per spot can be defined. Even if the noise increases, the visibility does as well. A bulk sensitivity was calculated to be 2407•2π•radRIU^{-1} as plotted in Figure 6.5. The visibility of 40.11% with a system noise of 0.124%, yields to a LOD of 1.01x10^{-7} RIU which is in good agreement with the values obtained via PD readout.

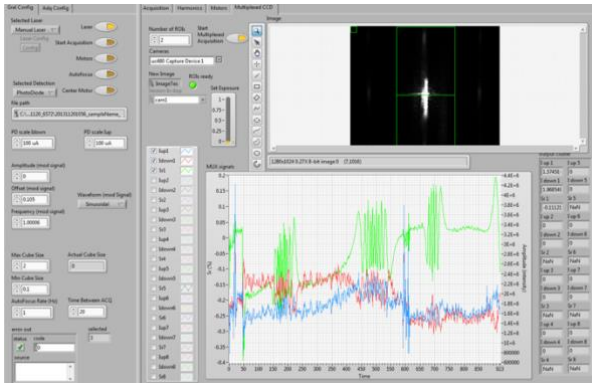

Figure 6.4 Software for calibration with CCD and 40x objective of a BiMW biosensor.

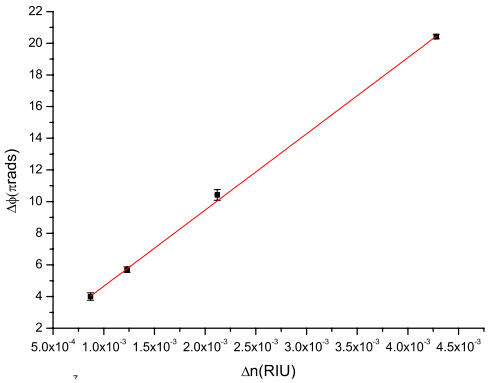

Figure 6.5 Calibration curve with 40X objective and CCD obtaining a LOD of 1.01x10^{-7} RIU.

6.1.3 CCD with 10X objective

Similarly, the 40x objective was replaced with a 10X one and a series of four different concentrations of HCl were injected (0.5 M, 0.25 M, 0.15 M and 0.10 M). The software with the successive injections is showed in Figure 6.6. The calibration curve is plotted in Figure 6.7 with a sensitivity of 2453•2π•radRIU^{-1}. A visibility of 43.66% with a noise of 0.107% yields to a LOD of 7.49x10^{-7} RIU.

As conclusion, there are no loss increases in terms of bulk sensitivity or LOD when comparing an analogue PD detection with digital methods employing CCD detection. Thus, the software for multiplexed CCD detection has been validated with 40x and 10x objectives against the same detection using two-section PDs.

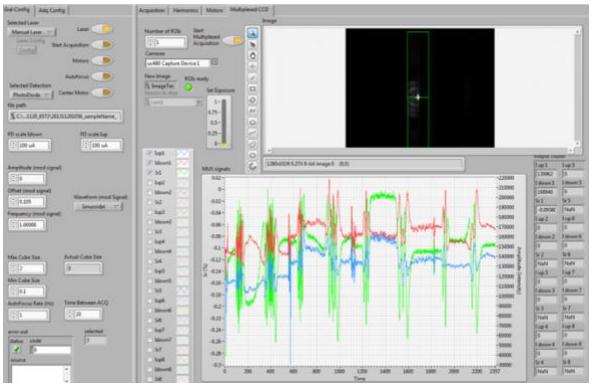

Figure 6.6 Software for calibration with 10X objective and CCD of a single BiMW biosensor.

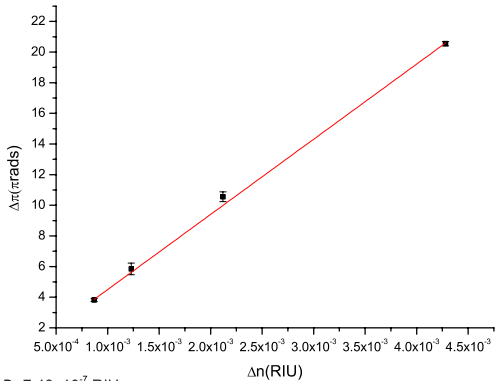

Figure 6.7 Calibration curve with 10X objective and CCD obtaining a LOD of $7.49x10^{-7}$ RIU.

Once the CCD detection has been proved to properly work with a single BiMW biosensor and no losses of sensitivity are observed, it is desired to extend the software application to include up to 8 waveguides simultaneously and test it using a commercial chip to chip coupling.

6.2 Experimental setup of multiplexed

Using a 1x8 splitter from *XioPhotonics* directly glued to a zirconia ferrule attached to a LP660 LD for in-coupling, a regular chip with 8 BiMW biosensors was calibrated. In order to do so, CCD detection with a 10X objective and a ND filter of 1.0 was employed. Successive solutions of HCl with different concentrations were injected (0.5, 0.25, 0.10 and 0.05 M) as explained in section 2.5 obtaining phase shifts as listed in Table 6.1. Figure 6.8 shows a screenshot of the simultaneous detection employing 16 ROIs (2 per BiMW) and post-processing and visualizing the interferometric signal S_R for each biosensor (1 to 7, BiMW8 seems to be clog or broken). The microfluidic cell covers the whole group of

8 biosensors delivering the sample simultaneously to all biosensors. The S_R simultaneous responses of all BiMW for each injection are plotted in Figure 6.9 to Figure 6.12. Finally, the LODs are listed in Table 6.2 and the plots of all the calibration curves is showed in Figure 6.13.

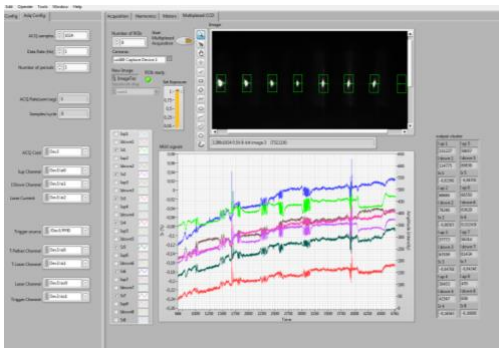

Figure 6.8 Screenshot of a multiplexed bulk calibration of 8 BiMW biosensors. The interferometric response S_R is plotted in the lower part for each biosensor.

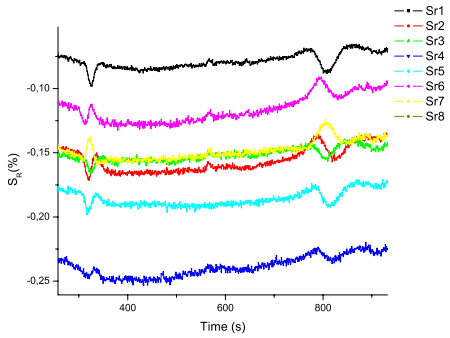

Figure 6.9 S_R response of 8 BiMW biosensors after the injection of 0.05 M HCl.

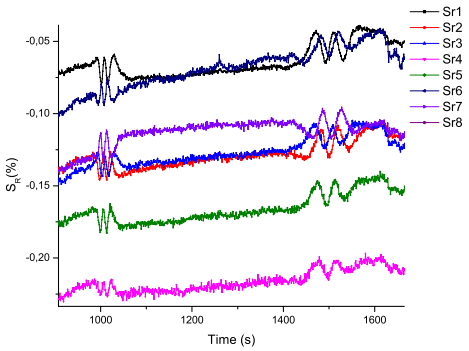

Figure 6.10 S_R response of 8 BiMW biosensors after the injection of 0.10 M HCl.

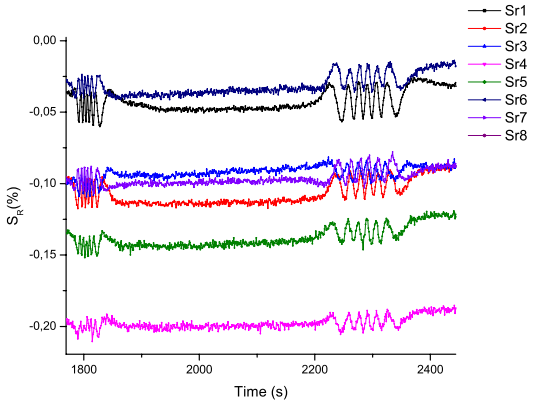

Figure 6.11 S_R response of 8 BiMW biosensors after the injection of 0.25 M HCl.

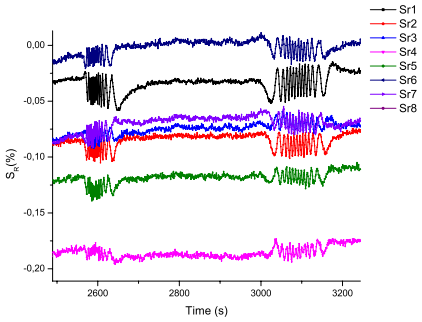

Figure 6.12 S_R response of 8 BiMW biosensors after the injection of 0.50 M HCl.

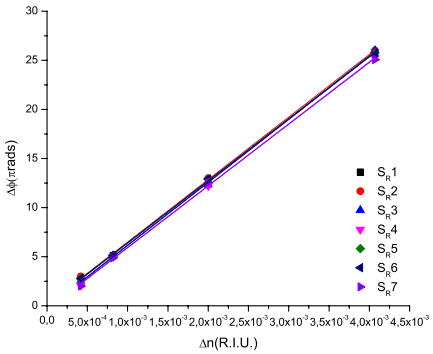

Figure 6.13 Calibration curves of BiMW1 to 7 after the series of successive injections of 0.5 M, 0.25 M, 0.10 M and 0.05 M HCl solutions. The bulk sensitivity for all BiMW biosensors is in the range of 3142 to 3215•2πradRIU^{-1} and the limits of detection in the range of ~10^{-6} RIU.

Even if the bulk sensitivities are good enough, the low visibility has affected the final calculation of the LOD for all BiMWsensors.

Table 6.1 Phase shift changes per concentration variation.

HCl [Molar]	Δn [RIU]	ΔØ1 [πrad]	ΔØ2 [πrad]	ΔØ3 [πrad]	ΔØ4 [πrds]	ΔØ5 [πrad]	ΔØ6 [πrad]	ΔØ7 [πrad]
0.50	$4.07x10^{-3}$	25.6800	26.0000	26.0000	25.5000	26.0000	25.6040	25.5200
0.25	$2.00x10^{-3}$	12.3790	13.0000	12.4190	12.4000	12.8550	12.8390	12.4560
0.10	$8.20x10^{-4}$	5.2666	5.0000	5.2390	5.0000	5.0000	5.2173	4.7849
0.05	$4.20x10^{-4}$	2.0000	3.0000	2.3930	2.0000	2.5570	3.0000	2.0000

Table 6.2 Bulk sensitivities and LODs of the multiplexed sensor.

Sensor [number]	Visibility [%]	Noise [%]	S_{bulk} [πradRIU^{-1}]	LOD [RIU]
BiMW1	0.03281	0.00099	6408	7.06E-06
BiMW2	0.02400	0.00123	6367	1.21E-05
BiMW3	0.01851	0.00129	6429	1.63E-05
BiMW4	0.01500	0.00161	6298	2.56E-05
BiMW5	0.01800	0.00135	6338	1.78E-05
BiMW6	0.01300	0.00139	6311	2.54E-05
BiMW7	0.02481	0.00139	6284	1.34E-05

Since the results are promising, we decide that we want to integrated the splitters on-chip, so we proceed with the design and simulation of beam splitters.

6.3 Design and simulation of IO beam splitters

The design of the next version of the BiMW sensor must include multiplexing capabilities. In order to implement a single input, multiple output device, a beam splitter could be built in the same chip. A quick research of photonic beam splitters or multiplexers implemented in telecomm industry shows different technologies such as MMIs, MZI, Y-junctions, curved junctions, prisms, photonic crystals, etc. It would be interesting to study the coupling losses of different configurations in order to obtain the most efficient splitter for our purposes. It is desired to have a compact splitter with the lowest splitting losses, and provide an even power distribution across outputs. Moreover, it is necessary to keep a spacing of 250 μm between waveguides to avoid cross-talking between sensors and maintaining the compatibility with standard photonics industry arrays. We initially proposed to study curved Y junctions, regular Y junctions, MMI and U junctions. Directional couplers were omitted because they will require a long coupling distance. Photonic crystals have been reported to provide splitting losses of 1 dB with very short lengths, however, such technology is out of the scope of this study due to the

required e-beam or nanoimprint lithography. The employed 3D model is showed in Figure 6.14. It is desired to keep d = 250 µm and to minimize the lengths of *L* and *W*.

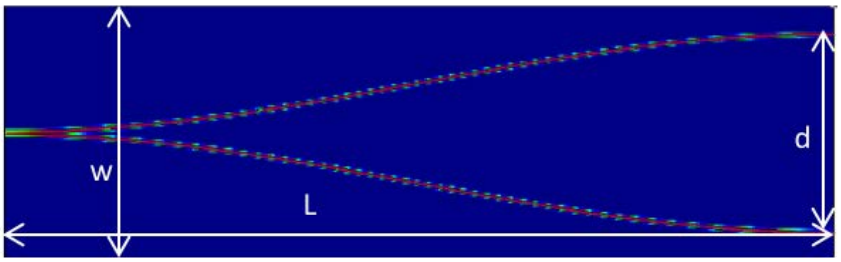

Figure 6.14 Variables employed for the simulated multiplexers. It is desirable to keep the separation between branches d = 250 µm so the industrial standards can be maintained and the cross-talk avoided. The length *L* and the width *w* should be as short as possible.

6.3.1 Multimode interferometers

Multimode interferometers (MMIs) are widely employed in the telecommunications industry and they have their origin in the observations of Talbot in 1836. He noticed that a monochromatic optical plane wave incident in a periodic grating would repeat itself at a given distance. In a MMI, there are multiple modes simultaneously interfering in a wide waveguide. If the output ports are placed at a spot where the interference is maximizing the intensity, then the MMI would act as a beam splitter. In our case, the MMI was simulated having a single mode rib waveguide of n_{core} = 2.0 and n_{clad} = 1.46 at the input and output with rib dimensions of 3 µm x 2 nm and core thickness of 150 nm. The spacing of 250 µm between waveguides at the output is maintained. A coupling efficiency of 38.2% per branch was calculated. The main drawback of MMI is its intolerance to fabrication errors especially in length, since small variations in the location of the output ports could affect the total output power on each arm.

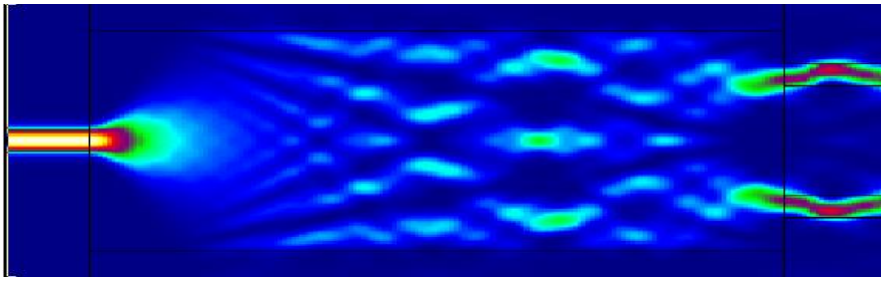

Figure 6.15 Radiation pattern of a simulated MMI. The total length is 2800 µm and the coupling coefficients are 38.2% per branch.

6.3.2 U-junction

A variation of the Y-junction is the U-junction where the U curve can be modelled as a quadratic or an exponential function. This solution is more feasible to fabricate however, no separations larger than 21 μm were achievable.

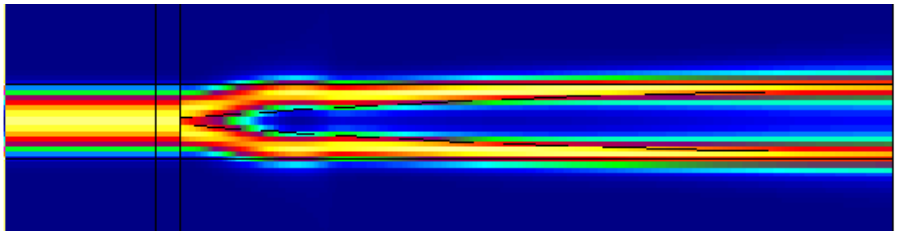

Figure 6.16 Radiation pattern of a U-junction (quadratic) splitter simulated in Photon Design.

6.3.3 S-shaped

S-shaped splitters are smooth versions of a Y-junction splitter, however, by avoiding abrupt changes in the waveguide and by keeping a 1 degree separation between arms, the light can travel longer and well-guided. Figure 6.17 shows an upper view of the radiation pattern of a S-shaped splitter made out of a single mode rib waveguide (H_{rib} = 2 nm, W_{rib} = 3 μm, core thickness of 150 nm) with core refractive index of 2.0 and cladding and substrate refractive indexes of 1.46. A coupling efficiency of 39.2% was evenly achieved between branches and a separation of d = 250 μm was also kept.

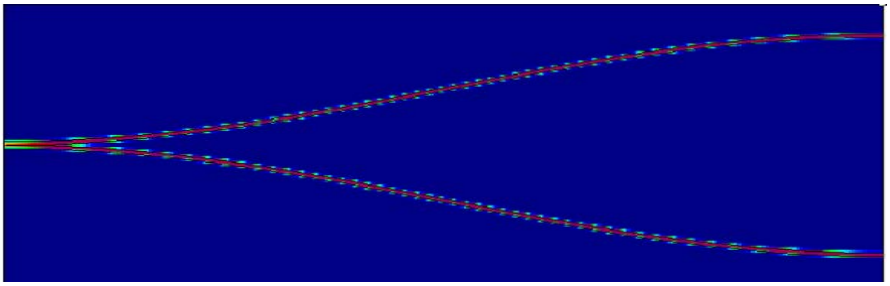

Figure 6.17 Radiation pattern simulated of a S-shapped splitter. Total length of 3840 μm is employed in order to keep the 250 μm spacing between branches. A coupling coefficient of 39.2% was evenly achieved in both branches.

All results for the different splitters are listed in Table 6.3. The inconvenience of Y-junctions, MMI couplers and V or U-shaped splitters is that such devices are very sensitive to errors in the dimension fabrication. Our group has previously fabricated S-shaped rib waveguide splitters for Mach-Zehnder Interferometer sensors. They are

tolerant enough to fabrication errors. The disadvantage of such S-shaped splitters is that they can be long while trying to maintain angles smaller than 1 degree. The length will depend on the number of required outputs (i.e. 2, 4 or 8 outputs). We have decided finally to use the S-shaped splitters despite their long dimension but we are ensuring the light guiding even with fabrication errors while keeping a 250 µm spacing between guides and an even power distribution across branches.

Table 6.3 Different splitter configurations and their coupling coefficients. S1 and S2 are the S-matrix parameters of coupling efficiencies.

Splitter	L (µm)	w(µm)	d(µm)	S1 (%)	S2 (%)
S-shape junction	7780	320	250	39.5	39.2
S-shape junction	3840	320	250	39.5	39.2
MMI	2800	50	24	38.2	38.2
Y junction	1500	90	60	44.9	44.9
U junction (quadratic)	1500	90	12	43.7	43.7
U junction (exponential)	1500	90	21	40.4	40.4

6.4 Fabrication of multiplexed BiMW nanointerferometric biosensors

Different splitter configurations were designed and fabricated: 1x2, 1x4 and 1x8. The photolithographic masks were done in a modular approach using GDSPY library. The fabrication process is the same as described in section 4.4.2.3 with the only distinction that the photolithographic masks used in the steps where the single mode sections and the rib is defined, will include the S-shaped splitting branches. Moreover, vertical tapers were chosen as coupling elements and intercalated across different models as detailed in Figure 6.18.

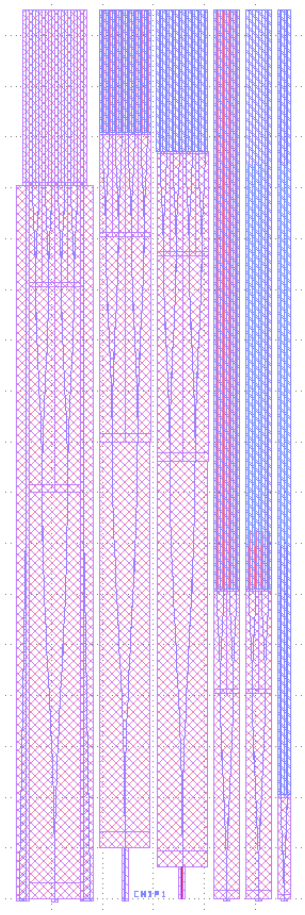

Figure 6.18 Chip with multiplexed BiMW sensors includes (from left to right) a reference single mode waveguide with vertical taper for in-coupling, then a 1x8 splitter without any in-coupling element, next a 1x8 splitter with vertical taper, subsequently a 1x4 splitter with bimodal waveguides, followed by a 1x4 splitter with bimodal waveguides with sensing areas and finally a 1x2 splitter without sensing window.

As previously discussed in 2.4.3.2, there are three possible read-out methods, but not all of them are suitable for simultaneous multiplexed detection. For example, a two-section PD will transduce the output intensity from all excited waveguides making impossible to distinguish across sensors. In other hand, as there are no commercial PD arrays available, a custom design and fabrication is very expensive (in the order of tens of thousands of euros as negotiated with Hammamatsu) since they require a tailored prototyping in terms of dimensions, wavelengths, materials and packaging. CCD detection is the most suitable readout mechanism for multiplexed detection readout.

6.5 Initial screening of chips: experimental results

A setup with a ML101J27 laser diode from Mitsubishi and CCD (DCU224M by Thorlabs®) detection mechanism was build. An ND filter of 0.5 was added to lower the output intensity and diminish the noise. An in-house fabricated holder with temperature control was used to grasp the chip while doing the measurements. Figure 6.19 shows the scheme of the experimental set-up employed for this characterization. We have chosen to characterize with the laser diode because it has stronger optical power than the fiber optic. Microfluidic cells could be designed as individualized channels attached each one to a BMSsa as showed in section 0. The other possibility is to use a larger cell that could cover a whole group of up to 8 waveguides simultaneously. But first, it is necessary to make a selection of the best chips fabricated.

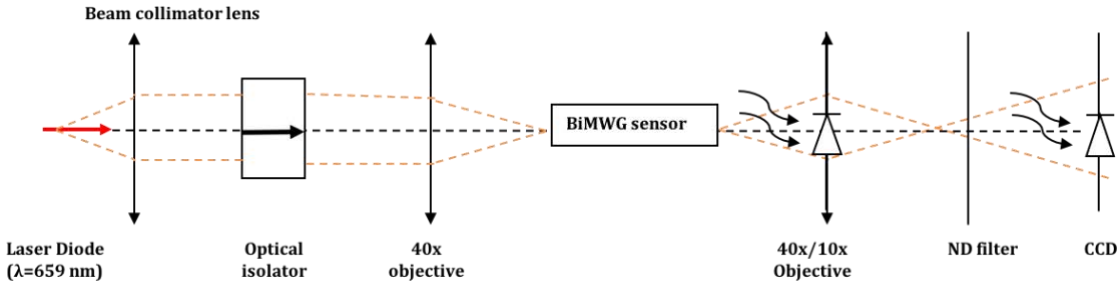

Figure 6.19 Optical setup for characterization of the multiplexed BiMW sensors using CCD readout and butt-coupling.

6.5.1 Screening of 1x4 splitters

Some splitters could have fabrication errors that could stop or diminish the light transmission across the waveguides. Therefore, as a first approach, we want to ensure that the fabricated waveguides are guiding the light properly. We start by a quick screening and we look for the chips with the most intense and evenly distributed outputs.

The next set of pictures show the in-coupling on the left side and the CCD image obtained at the output of the chip. We are using a 10X objective in order to see all the outputs at the same time, but it is worthy to notice that the spots are small and pixels are so big that quantifiable values calculated via image processing algorithms could be too far from the real ones. It would be possible to change the 10X objective for another with higher amplification in order to obtain a more detailed image, with higher resolution, thus, lower noise and a possible detection. Nevertheless, as a firs proof of concept we have validated 1x4 splitters without tapers and the output spots are showed in Figure 6.20.

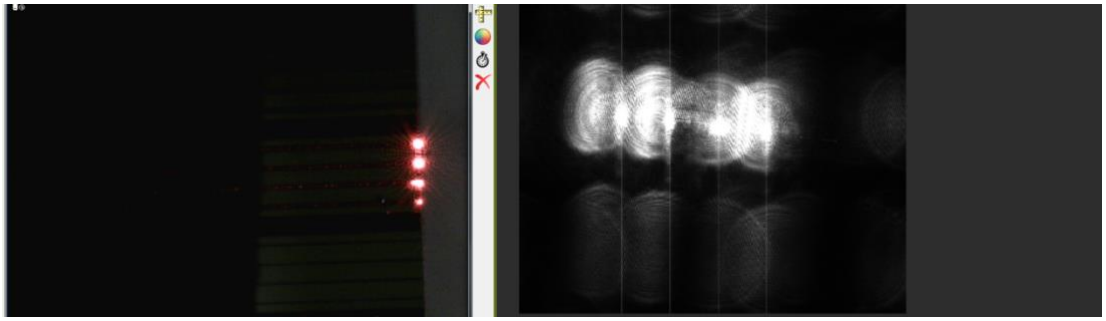

Figure 6.20 Splitter built without in-coupling elements and without sensing area opened. The four outputs vary their intensity depending on the in-coupling position. The left image shows the output at naked-eye scale.

6.5.2 Screening of 1x8 splitters

Similarly, we want to compare the output of 1x8 splitters. Figure 6.21 shows the output of the 1x8 splitter with a vertical taper. It seems that the vertical taper is enhancing the light in-coupling thus, providing better optical outputs at the 1x8 rib waveguide splitter.

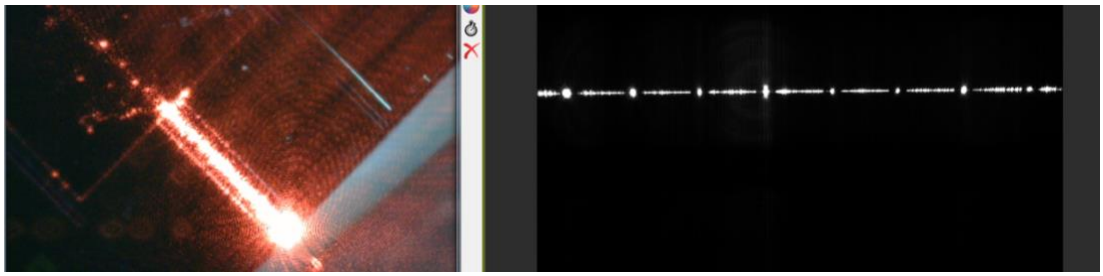

Figure 6.21 Vertical taper in-coupling of a 1x8 splitter (left) and its output. The crosstalk noise seems to decrease and the bimodal waveguide spots are individually defined. Light is coming out of plane as observed in the horizontal line at the output, however, by incorporating ND optical filters it is possible to properly visualize the output spots only.

Once the chips with the most intense and even distributed outputs are selected, it is necessary to work in the software implementation for the simultaneous, real-time, multiplexed detection.

Figure 6.22 shows a screenshot of the evaluation of 8 BiMW biosensors after injecting 0.5 M HCl solution simultaneously in all sensors employing a CCD detection. However, due to the presence of SU-8 debris in the sensing area, the interferometric response was almost null. It is not possible to perform a decent calibration under these conditions. A different approach would be required in order to validate the multiplexing system.

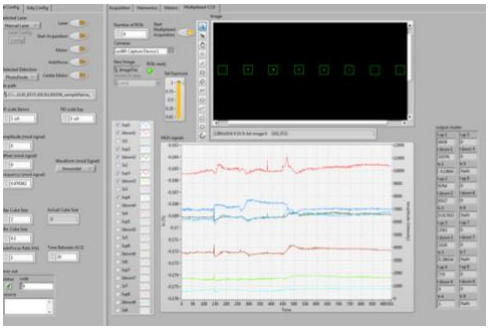

Figure 6.22 Simultaneous evaluation of 8 waveguides in order to test the software response.

6.6 Conclusion

The multiplex CCD software for detection was developed, incorporated to the main software, and validated against PD detection by performing calibrations of the same biosensor. Moreover, 10X and 40X objectives were also validated observing no loss of sensitivity or increments on the LOD.

As a first approach to the multiplexed detection, a commercial 1x8 splitter (TM polarized) was coupled to a regular BiMW nanointerferometric biosensor chip and a simultaneous multiplexed bulk calibration was performed. The obtained LODs are in good agreement with the previous reported LODs.

IO beam splitters were designed and simulated while keeping the restriction that they should be fabricated only with standard microelectronic techniques, their design dimensions should be achievable through photolithographic processes and they must ensure an even distribution of output intensities. After selecting S-shaped splitters for in-house fabrication, the photolithographic masks for 1x8 BiMW nanointerferometric biosensor were designed and fabricated. However, the fabricated multiplexed chips incorporating in-coupling elements were clotted at the sensing area diminishing the visibility of the sensor and making impossible the simultaneous calibration. Nevertheless, future fabrications could incorporate multiplexed sensors with better sensitivities by avoiding the SU-8 clotting.

7 GENERAL CONCLUSIONS AND FUTURE WORK

"One never notices what has been done; one can only see what remains to be done"

- *Marie Curie*

This chapter provides the Thesis conclusions, discussing the challenges ahead and the work to be done in order to achieve a complete LOC platform integration, including the implementation of the temperature compensation by waveguides reference, the re-design of the mechanics, electronics, optics and software systems, and the final design of the BiMW nanointerferometric biosensor.

Optical biosensors based in interferometry offer the most sensitive devices and lowest limits of detection. It has been showed that the BiMW nanointerferometric biosensor is one of the most sensitive label-free, IO biosensors. It offers the sensibility inherent to interferometers but its fabrication is simpler since it does not require curves or bended paths. Even if the sensor works properly achieving LODs in the order of ~10^{-7} RIU, there could be some room for optimizations. In that sense, the BiMW biosensor has been designed to work in the visible range, with a Si_3N_4 core, on a SiO_2 substrate. The core thickness has been previously optimized for maximum sensitivity while ensuring modal interferometric behaviour of both TE and TM polarizations. Similarly, the rib height and width have been studied and a range of values delimited to ensure the proper guiding of only the fundamental mode in the single mode section and to ensure the propagation of only the fundamental and first order mode in the bimodal section. The location of the step junction where the first order mode is excited has been also studied, showing more energy transfer across modes when it is located under the sensing window (with water media instead of SiO_2) thus increasing the sensitivity. The length of the chip could be reduced without compromising sensitivity while gaining in chip density per wafer instead. It has been experimentally probed that a smaller chip with two thirds of the actual size would work with similar sensitivities and LODs. Finally, an optimal sensitivity working range of biolayer thicknesses was determined to be between 1 and 300 nm. Detection of the

human growth hormone directly in urine was done, showing that SAMs are being formed within these values. The BiMW was optically characterized calculating its insertion losses, numerical aperture and propagation constant.

However, challenges remain on its way towards a full integrated LOC platform. A LOC system should harmoniously orchestrate several sub-systems like mechanical, thermal, optical, microfluidic, electronics and software for data acquisition, and biological systems. Each one of them has unique challenges to overcome depending on the required conditions of the assay (i.e. access to electrical energy, regeneration or not of the bioreceptors, analyte media, and so on).

In that sense, new models of chip holders and PD micro-positioning magnetic holders were designed, 3D printed for quick prototyping and finally CNC milled in aluminium. Similarly, new microfluidic cells with smaller dimensions were designed. The moulds were fabricated on SU-8 in clean room facilities and the final microfluidic cell casted in PDMS. Such smaller cells provided an enhancement of two orders of magnitude in the LOD.

In terms of electronics and software, several models of National Instruments® acquisition cards were tested including the generation of the modulation signal. The architecture of the software is OOLV based on interruptions, maintaining a close loop and a parallel thread for data processing, storage and visualization. Again, the implementation of OOLV in a modular way allowed us to finally use a single software to control all different models of acquisition cards and laser controllers making it transparent to the final user. The CCD detection algorithm was tested and compared with a typical PD analogue detection obtaining good results and added to the production branch of the software. Multiplexing capabilities were also added to the software and experimentally demonstrated. The possibility to choose between modulation schemes is also included while the software generates the modulation signal to be injected to the laser controller.

In the optical subsystem, several laser sources were tested and optically characterized. Using a modular approach, it was possible to swap between butt-coupled LDs, fibre optics or HeNe laser sources, and to change the PD micro-positioning holder for a CCD in case of required multiplexed detection.

In-coupling mechanisms were designed, simulated, fabricated, characterized and compared. This work focused in a vertically stacked taper and an inverted taper. The first one requires the addition of two more photolithographic mask levels and the structures

are made out of SU-8 at clean room facilities using standard techniques. A bulk calibration was performed to ensure that no losses to the bulk sensitivity were added. It was optically characterized obtaining a 2.6 dB insertion loss. The LOD was calculated to be ~10^{-6} RIU. This could be due to the presence of SU-8 debris in the sensing area affecting the interference between both modes and the sensing media. The second in-coupling device proposed was an inverted taper. Its simpler fabrication is its main advantage. Only one photolithographic mask level was added and no extra material is required. It shows a nice acceptance angle of up to 7 degrees in the vertical tilt. Moreover, a calibration curve was performed achieving a LOD of $4.9x10^{-6}$, again, the variation could be due to the presence of SU-8 debris.

A chirp modulation system was implemented by taking advantage of the defect of some LDs. Varying the laser diode driving current will cause a spectral shift of 1 or 2 nm in diodes like the ML101J27 from Mitsubishi or the LP660 from Thorlabs®. Each wavelength will experience a different optical path, thus different sensitivities are obtained. By choosing the wavelengths located in the Q-point, it is possible to enhance the sensitivity up to 12%. Moreover, if this spectral shift is sufficient to inject enough wavelengths to complete a whole cycle of the interferometric signal, the problem of fringe and direction ambiguities is overcome. It has been showed that this is our case. The post-processing was performed in iPython Notebook by testing and comparing two different statistical methods for phase extraction.

In the case of multiplexing, two approaches were taken: the first one is to use a commercial 1-to-8 splitter to simultaneously excite 8 BiMW sensors and the second one is to fabricate ourselves the 1-to-8 splitter on-chip. The first option was done and simultaneous bulk calibrations were performed achieving LODs in the order of ~10^{-7} RIU. For the second approach, different multiplexing structures were studied finally selecting the S-shaped bend. Splitters were designed and its photolithographic masks built in a modular approach using GDSPY. The designs included 1x2, 1x4 and 1x8 splitters and in-coupling elements were also added. They were fabricated in clean room facilities employing standard CMOS technologies. The multiplexed BiMW was tested but due to the presence of SU-8 debris in the sensing window, the response was not as expected. Nevertheless, the power splitting across branches seemed to be even.

As future work on the road towards a fully commercial LOC BiMW biosensor, it would be required to migrate all the software and algorithms previously implemented to a more

reliable software development platform (i.e. Python, JS node, etc.). It would be interesting to study the optical bandwidth of the BiMW.

With the aim to minimize the use of sub-systems, a thermal compensation could be done by using a reference BiMW instead of the TEC, sensor and temperature controller. A new chip design including all the proposed improvements. Inverted tapers are a good candidate for in-coupling. future designs should include them *a priori*. The chirp modulation system and its statistical methods for phase extraction should be also implemented in the next version of the software. The individualized microfluidic channels should be used instead of the macro cells. It is necessary to work in the design of the final system which would include 8 polarized light sources (perhaps via a 1-to-8 splitter), the electronics, mechanical and CCD detection sub-systems. It will be then ready to look for commercial user cases.

8 REFERENCES

[1] Lederberg J 2000 Infectious History *Science.* **288** 287–93

[2] Kanchi S, Sabela M I, Mdluli P S, Inamuddin and Bisetty K 2018 Smartphone based bioanalytical and diagnosis applications: A review *Biosens. Bioelectron.* **102** 136–49

[3] Wu T F, Chen Y C, Wang W C, Kucknoor A S, Lin C J, Lo Y H, Yao C W and Lian I 2017 Rapid waterborne pathogen detection with mobile electronics *Sensors* **17** 1–11

[4] Long K D, Woodburn E V., Le H M, Shah U K, Lumetta S S and Cunningham B T 2017 Multimode smartphone biosensing: the transmission, reflection, and intensity spectral (TRI)-analyzer *Lab Chip* **17** 3246–57

[5] Mudanyali O, Dimitrov S, Sikora U, Padmanabhan S, Navruz I and Ozcan A 2012 Integrated rapid-diagnostic-test reader platform on a cellphone. *Lab Chip* **12** 2678–86

[6] Laksanasopin T, Guo T W, Nayak S, Sridhara A A, Xie S, Olowookere O O, Cadinu P, Meng F, Chee N H, Kim J, Chin C D, Munyazesa E, Mugwaneza P, Rai A J, Mugisha V, Castro A R, Steinmiller D, Linder V, Justman J E, Nsanzimana S and Sia S K 2015 A smartphone dongle for diagnosis of infectious diseases at the point of care *Sci. Transl. Med.* **7** 273re1-273re1

[7] Ganguli A, Ornob A, Yu H, Damhorst G L, Chen W, Sun F, Bhuiya A, Cunningham B T and Bashir R 2017 Hands-free smartphone-based diagnostics for simultaneous detection of Zika, Chikungunya, and Dengue at point-of-care *Biomed. Microdevices* **19** 1–13

[8] Caliendo A M, Gilbert D N, Ginocchio C C, Hanson K E, May L, Quinn T C, Tenover F C, Alland D, Blaschke A J, Bonomo R A, Carroll K C, Ferraro M J, Hirschhorn L R, Joseph W P, Karchmer T, MacIntyre A T, Reller L B and Jackson A F 2013 Better Tests, Better Care: Improved Diagnostics for Infectious Diseases *Clin. Infect. Dis.* **57** S139–70

[9] Ligler F S 2009 Perspective on Optical Biosensors and Integrated Sensor Systems *Anal. Chem.* **81** 519–26

[10] Chin C D, Linder V and Sia S K 2012 Commercialization of microfluidic point-of-care diagnostic devices *Lab Chip* **12** 2118–34

[11] Lechuga L M 2005 Biosensors and Modern Biospecific Analytical Techniques *Comprehensive Analytical Chemistry* vol 44, ed L Gorton (Elsevier) pp 209–50

[12] Estevez M C, Alvarez M and Lechuga L M 2012 Integrated optical devices for lab-on-a-chip biosensing applications *Laser Photon. Rev.* **6** 463–87

[13] Fan X, White I M, Shopova S I, Zhu H, Suter J D and Sun Y 2008 Sensitive optical biosensors for unlabeled targets: a review *Anal Chim Acta* **620** 8–26

[14] White I M and Fan X 2008 On the performance quantification of resonant refractive index sensors *Opt. Express* **16** 1020–8

[15] Marcatili E A J 1969 Dielectric Rectangular Waveguide and Directional Coupler for Integrated Optics *Bell Syst. Tech. J.* **48** 2071–102

[16] Miller S E 1969 Integrated Optics: An Introduction *Bell Syst. Tech. J.* **48** 2059–69

[17] Savchenkov A A, Ilchenko V S, Matsko A B and Maleki L 2004 Kilohertz optical

resonances in dielectric crystal cavities *Phys. Rev. A - At. Mol. Opt. Phys.* **70** 1–4

[18] Iqbal M, Gleeson M A, Spaugh B, Tybor F, Gunn W G, Hochberg M, Baehr-Jones T, Bailey R C and Gunn L C 2010 Label-free biosensor arrays based on silicon ring resonators and high-speed optical scanning instrumentation *IEEE J. Sel. Top. Quantum Electron.* **16** 654–61

[19] Barrios C A 2012 Integrated microring resonator sensor arrays for labs-on-chips *Anal. Bioanal. Chem.* **403** 1467–75

[20] Jiang X, Ye J, Zou J, Li M and He J-J 2013 Cascaded silicon-on-insulator double-ring sensors operating in high-sensitivity transverse-magnetic mode *Opt. Lett.* **38** 1349–51

[21] Garcia J R, Granda M G, Gavela A F, Presa S A, Lastra M R and Fernández S F 2012 Electromagnetic Waves Scattering At interfaces Between Dielectric Waveguides: a Review on Analysis and Applications *Prog. Electromagn. Res. B* **37** 103–24

[22] Dorfner D F, Hürlimann T, Zabel T, Frandsen L H, Abstreiter G and Finley J J 2008 Silicon photonic crystal nanostructures for refractive index sensing *Appl. Phys. Lett.* **93** 2006–9

[23] Kang C, Phare C T, Vlasov Y A, Assefa S and Weiss S M 2010 Photonic crystal slab sensor with enhanced surface area *Opt. Express* **18** 27930–7

[24] Yan H, Zou Y, Chakravarty S, Yang C-J, Wang Z, Tang N, Fan D and Chen R T 2015 Silicon on-chip bandpass filters for the multiplexing of high sensitivity photonic crystal microcavity biosensors *Appl. Phys. Lett.* **106** 121103

[25] Abramovici A, Althouse W E, Drever R W P, Gürsel Y, Kawamura S, Raab F J, Shoemaker D, Sievers L, Spero R E, Thorne K S, Vogt R E, Weiss R, Whitcomb S E and Zucker M E 1992 LIGO: The Laser Interferometer Gravitational-Wave Observatory *Source Sci. New Ser. Astrophys. J. Annu. Rev. Astron. Astrophys. Sp. Sci. Rev. B. Madore R. B. Tully, Eds* **256** 325–33

[26] Heideman R G, Kooyman R P H and Greve J 1991 Development of an optical waveguide interferometric immunosensor *Sensors Actuators B Chem.* **4** 297–9

[27] Lechuga L M, Lenferink A T M, Kooyman R P H and Greve J 1995 Feasibility of evanescent wave interferometer immunosensors for pesticide detection: chemical aspects *Sensors Actuators B. Chem.* **25** 762–5

[28] Schipper E F, Brugman A M, Dominguez C, Lechuga L M, Kooyman R P H and Greve J 1997 The realization of an integrated Mach-Zehnder waveguide immunosensor in silicon technology *Sensors Actuators, B Chem.* **40** 147–53

[29] Prieto F, Sepúlveda B, Calle A, Llobera A, Domínguez C and Lechuga L . 2003 Integrated Mach–Zehnder interferometer based on ARROW structures for biosensor applications *Sensors Actuators B Chem.* **92** 151–8

[30] Zinoviev K, Carrascosa L G, Sánchez del Río J, Sepúlveda B, Domínguez C and Lechuga L M 2008 Silicon Photonic Biosensors for Lab-on-a-Chip Applications *Adv. Opt. Technol.* **2008** 1–6

[31] Densmore A, Xu D, Waldron P, Janz S, Cheben P, Lapointe J, Delâge A, Lamontagne B, Schmid J H and Post E 2006 A Silicon-on-Insulator Photonic Wire Based Evanescent Field Sensor *IEEE Photonics Technol. Lett.* **18** 2520–2

[32] Densmore A, Vachon M, Xu D-X, Janz S, Ma R, Li Y-H, Lopinski G, Delâge A, Lapointe J, Luebbert C C, Liu Q Y, Cheben P and Schmid J H 2009 Silicon photonic wire biosensor array for multiplexed real-time and label-free molecular detection. *Opt. Lett.* **34** 3598–600

[33] Crespi A, Gu Y, Ngamsom B, Hoekstra H J W M, Dongre C, Pollnau M, Ramponi R, van den Vlekkert H H, Watts P, Cerullo G and Osellame R 2010 Three-dimensional Mach-Zehnder interferometer in a microfluidic chip for spatially-

resolved label-free detection. *Lab Chip* **10** 1167–73
[34] Mathesz A, Fábián L, Valkai S, Alexandre D, Marques P V S, Ormos P, Wolff E K and Dér A 2013 High-speed integrated optical logic based on the protein bacteriorhodopsin *Biosens. Bioelectron.* **46** 48–52
[35] Choo S J, Lee B-C, Lee S-M, Park J H and Shin H-J 2009 Optimization of silicon oxynitrides by plasma-enhanced chemical vapor deposition for an interferometric biosensor *J. Micromechanics Microengineering* **19** 095007
[36] Choo S J, Kim J, Lee K W, Lee D H, Shin H J and Park J H 2014 An integrated Mach-Zehnder interferometric biosensor with a silicon oxynitride waveguide by plasma-enhanced chemical vapor deposition *Curr. Appl. Phys.* **14** 954–9
[37] Duval D, Osmond J, Dante S, Dominguez C and Lechuga L M 2013 Grating couplers integrated on Mach-Zehnder interferometric biosensors operating in the visible range *IEEE Photonics J.* **5** 3700108
[38] Estevez M C, Alvarez M and Lechuga L M 2012 Integrated optical devices for lab-on-a-chip biosensing applications *Laser Photon. Rev.* **6** 463–87
[39] Brandenburg A and Henninger R 1994 Integrated optical Young interferometer *Appl. Opt.* **33** 5941–7
[40] Brandenburg A, Krauter R, Künzel C, Stefan M and Schulte H 2000 Interferometric sensor for detection of surface-bound bioreactions *Appl. Opt.* **39** 6396–405
[41] Brynda E, Houska M, Brandenburg A and Wikerstål A 2002 Optical biosensors for real-time measurement of analytes in blood plasma *Biosens. Bioelectron.* **17** 665–75
[42] Ymeti A, Kanger J S, Greve J, Lambeck P V, Wijn R and Heideman R G 2003 Realization of a multichannel integrated Young interferometer chemical sensor. *Appl. Opt.* **42** 5649–60
[43] Ymeti A, Greve J, Lambeck P V., Wink T, Van Novell S W F M, Beumer T A M, Wijn R R, Heideman R G, Subramaniam V and Kanger J S 2007 Fast, ultrasensitive virus detection using a young interferometer sensor *Nano Lett.* **7** 394–7
[44] Mulder H K P, Ymeti A, Subramaniam V and Kanger J S 2012 Size-selective detection in integrated optical interferometric biosensors *Opt. Express* **20** 20934–50
[45] Schmitt K, Schirmer B and Brandenburg A 2005 Label-free detection of biomolecules by waveguide interferometry *17th International Conference on Optical Fibre Sensors* vol 5855, ed M Voet, R Willsch, W Ecke, J Jones and B Culshaw (Bellingham, WA: Proceedings of SPIE) pp 459–62
[46] Schmitt K, Schirmer B, Hoffmann C, Brandenburg A and Meyrueis P 2007 Interferometric biosensor based on planar optical waveguide sensor chips for label-free detection of surface bound bioreactions *Biosens. Bioelectron.* **22** 2591–7
[47] Cross G H, Reeves A a., Brand S, Popplewell J F, Peel L L, Swann M J and Freeman N J 2003 A new quantitative optical biosensor for protein characterisation *Biosens. Bioelectron.* **19** 383–90
[48] Zinoviev K E, González-Guerrero A B, Domínguez C and Lechuga L M 2011 Integrated bimodal waveguide interferometric biosensor for label-free analysis *J. Light. Technol.* **29** 1926–30
[49] Kunz R E and Cottier K 2006 Optimizing integrated optical chips for label-free (bio-)chemical sensing. *Anal. Bioanal. Chem.* **384** 180–90
[50] Lifante G 2003 *Theory of Integrated Optic Waveguides* vol 1 (Chichester, UK: John Wiley & Sons, Ltd)
[51] Chang W S C 2005 *Principles of lasers and optics* vol 9780521642 (Cambridge

University Press)
[52] Sudbo A S 1993 Film mode matching: a versatile numerical method for vector mode field calculations in dielectric waveguides *Pure Appl. Opt. J. Eur. Opt. Soc.* **2** 211–33
[53] Prieto F, Sepúlveda B, Calle A, Llobera A, Domínguez C, Abad A, Montoya A and Lechuga L M 2003 An integrated optical interferometric nanodevice based on silicon technology for biosensor applications *Nanotechnology* **14** 907–12
[54] Dante S 2014 *All-optical phase modulation for advanced interferometric point-of-care biosensors* (Doctoral Thesis. Autonomous University of Barcelona)
[55] Dante S, Duval D, Sepúlveda B, González-Guerrero A B, Sendra J R and Lechuga L M 2012 All-optical phase modulation for integrated interferometric biosensors *Opt. Express* **20** 7195
[56] Prieto F, Lechuga L M, Calle A, Llobera A and Domínguez C 2001 Optimized Silicon Antiresonant Reflecting Optical Waveguides for Sensing Applications *J. Light. Technol.* **19** 75–83
[57] Photon Design 2009 FIMMPROP manual Version 5.2 © 1997-2009 33–4
[58] Bañuls M J, Puchades R and Maquieira Á 2013 Chemical surface modifications for the development of silicon-based label-free integrated optical (IO) biosensors: A review *Anal. Chim. Acta* **777** 1–16
[59] Levy R and Ruschin S 2008 Critical sensitivity in hetero-modal interferometric sensor using spectral interrogation *Opt. Express* **16** 20516–21
[60] González-Guerrero A B, Maldonado J, Dante S, Grajales D and Lechuga L M 2017 Direct and label-free detection of the human growth hormone in urine by an ultrasensitive bimodal waveguide biosensor *J. Biophotonics* **10** 61–7
[61] Lukosz W 1991 Principles and sensitivities of integrated optical and surface plasmon sensors for direct affinity sensing and immunosensing *Biosens. Bioelectron.* **6** 215–25
[62] Lynn N S, Šípová H, Adam P and Homola J 2013 Enhancement of affinity-based biosensors: effect of sensing chamber geometry on sensitivity. *Lab Chip* **13** 1413–21
[63] Daldosso N, Melchiorri M, Riboli F, Girardini M, Pucker G, Crivellari M, Bellutti P, Lui A and Pavesi L 2004 Comparison Among Various Si3N4 Waveguide Geometries Grown Within a CMOS Fabrication Pilot Line *J. Light. Technol.* **22** 1734–40
[64] Sanchez del Rio J and Lechuga L M 2004 *Development of a high sensitive photonic biosensor based on Mach-Zehnder interferometers integrated in silicon microelectronics technology (in Spanish).* (Doctoral Thesis. Autonomous University of Madrid)
[65] Karioja P and Howe D 1996 Diode-laser-to-waveguide butt coupling *Appl. Opt.* **35** 404–16
[66] Burns W K and Hocker G B 1977 End fire coupling between optical fibers and diffused channel waveguides *Appl. Opt.* **16** 2048–50
[67] Fisher C, Botten L C, Poulton C G, McPhedran R C and de Sterke C M 2015 Efficient end-fire coupling of surface plasmons in a metal waveguide *J. Opt. Soc. Am. B* **32** 412–25
[68] Duval D, González-Guerrero A B, Dante S, Osmond J, Monge R, Fernández L J, Zinoviev K E, Domínguez C and Lechuga L M 2012 Nanophotonic lab-on-a-chip platforms including novel bimodal interferometers, microfluidics and grating couplers *Lab Chip* **12** 1987–94
[69] Vermeulen D, Selvaraja S, Verheyen P, Lepage G, Bogaerts W, Absil P, Van Thourhout D and Roelkens G 2010 High-efficiency fiber-to-chip grating couplers

realized using an advanced CMOS-compatible Silicon-On-Insulator platform *Opt. Express* **18** 18278–83

[70] Muñoz P, Pastor D and Capmany J 2002 Modeling and design of arrayed waveguide gratings *J. Light. Technol.* **20** 661–74

[71] Cheben P, Xu D-X, Janz S and Densmore A 2006 Subwavelength waveguide grating for mode conversion and light coupling in integrated optics *Opt. Express* **14** 4695–702

[72] Bock P J, Cheben P, Schmid J H, Lapointe J, Janz S, Xu D-X, Densmore A, Delage A, Lamontagne B and Hall T J 2010 Subwavelength grating: A new type of microphotonic waveguide and implementations to fiber-chip coupling, waveguide crossing and refractive index engineering *7th IEEE International Conference on Group IV Photonics* (Beijing, China: IEEE) pp 31–3

[73] Flueckiger J, Schmidt S, Donzella V, Sherwali A, Ratner D M, Chrostowski L and Cheung K C 2016 Sub-wavelength grating for enhanced ring resonator biosensor *Opt. Express* **24** 15672–86

[74] Zhu L, Yang W and Chang-Hasnain C 2017 Very high efficiency optical coupler for silicon nanophotonic waveguide and single mode optical fiber. *Opt. Express* **25** 18462–73

[75] Taillaert D, Chong H, Borel P I, Frandsen L H, De La Rue R M and Baets R 2003 A compact two-dimensional grating coupler used as a polarization splitter *IEEE Photonics Technol. Lett.* **15** 1249–51

[76] Andonegui I, Calvo I and Garcia-Adeva A J 2015 Coupling light into photonic integrated circuits using non-periodic surfaces *2015 17th International Conference on Transparent Optical Networks (ICTON)* (Budapest, Hungary: IEEE) pp 1–4

[77] Orobtchouk R, Layadi A, Gualous H, Pascal D, Koster A and Laval S 2000 High-efficiency light coupling in a submicrometric silicon-on-insulator waveguide *Appl. Opt.* **39** 5773–7

[78] Markov P, Valentine J G and Weiss S M 2012 Fiber-to-chip coupler designed using an optical transformation *Opt. Express* **20** 14705–13

[79] Ropers C, Neacsu C C, Elsaesser T, Albrecht M, Raschke M B and Lienau C 2007 Grating-Coupling of Surface Plasmons onto Metallic Tips: A Nanoconfined Light Source *Nano Lett.* **7** 2784–8

[80] Chen B, Wood A, Pathak A, Mathai J, Bok S, Zheng H, Hamm S, Basuray S, Grant S, Gangopadhyay K, Cornish P V. and Gangopadhyay S 2016 Plasmonic gratings with nano-protrusions made by glancing angle deposition for single-molecule super-resolution imaging *Nanoscale* **8** 12189–201

[81] Triggs G J, Wang Y, Reardon C P, Fischer M, Evans G J O and Krauss T F 2017 Chirped guided-mode resonance biosensor *Optica* **4** 229–34

[82] Gili-de-Villasante O, Tcheg P, Wang B, Suna A, Giannoulis G, Lazarou I, Apostolopoulos D, Avramopoulos H, Pleros N, Baus M, Karl M and Tekin T 2012 Design, fabrication, and characterisation of fully etched TM grating coupler for photonic integrated system-in-package *Proc. SPIE 8431, Silicon Photonics and Photonic Integrated Circuits III* vol 8431, ed L Vivien, S Honkanen, L Pavesi and S Pelli (Brussels, Belgium) p 84310G–84310G–8

[83] Modak S, Patil A, Patil R, Garde C S, Purandare R G, Vengurlekar A S and Gopal A V 2011 Silicon based taper waveguides for near field coupling *IEEE Photonic Society 24th Annual Meeting, PHO 2011* vol 2 (Arlington, VA, United States of America.) pp 463–4

[84] Porte H, Ben Bakir B and Bernabe S 2011 Epoxy free butt coupling between a lensed fiber and a silicon nanowire waveguide with an inverted taper configuration *8th IEEE International Conference on Group IV Photonics* (The Royal Society,

London, UK: IEEE) pp 386–8
[85] Pu M, Liu L, Ou H, Yvind K and Hvam J M 2010 Ultra-low-loss inverted taper coupler for silicon-on-insulator ridge waveguide *Opt. Commun.* **283** 3678–82
[86] Tao S H, Song J, Fang Q, Yu M B, Lo G Q and Kwong D L 2008 Improving coupling efficiency of fiber-waveguide coupling with a double-tip coupler. *Opt. Express* **16** 20803–8
[87] Fu Y, Ye T, Tang W and Chu T 2014 Efficient adiabatic silicon-on-insulator waveguide taper *Photonics Res.* **2** A41
[88] Khilo A, Popović M A, Araghchini M and Kärtner F X 2010 Efficient planar fiber-to-chip coupler based on two-stage adiabatic evolution. *Opt. Express* **18** 15790–806
[89] Milton A and Burns W 1977 Mode coupling in optical waveguide horns *IEEE J. Quantum Electron.* **13** 828–35
[90] Lambeck P V. 1999 Remote opto-chemical sensing with extreme sensitivity: Design, fabrication and performance of a pigtailed integrated optical phase-modulated Mach-Zehnder interferometer system *Sensors Actuators, B Chem.* **61** 100–27
[91] Dumais P, Callender C L, Noad J P and Ledderhof C J 2008 Integrated optical sensor using a liquid-core waveguide in a Mach-Zehnder interferometer. *Opt. Express* **16** 18164–72
[92] Sepúlveda B, Armelles G and Lechuga L M 2007 Magneto-optical phase modulation in integrated Mach-Zehnder interferometric sensors *Sensors Actuators, A Phys.* **134** 339–47
[93] Kozma P, Hamori A, Cottier K, Kurunczi S and Horvath R 2009 Grating coupled interferometry for optical sensing *Appl. Phys. B Lasers Opt.* **97** 5–8
[94] Dante S, Duval D, Fariña D, González-Guerrero A B and Lechuga L M 2015 Linear readout of integrated interferometric biosensors using a periodic wavelength modulation *Laser Photonics Rev.* **9** 248–55
[95] Levy R, Ruschin S and Goldring D 2009 Critical sensitivity effect in an interferometer sensor. *Opt. Lett.* **34** 3023–5
[96] Kitsara M, Misiakos K, Raptis I and Makarona E 2010 Integrated optical frequency-resolved Mach-Zehnder interferometers for label-free affinity sensing. *Opt. Express* **18** 8193–206
[97] Misiakos K, Raptis I, Salapatas A, Makarona E, Botsialas A, Hoekman M, Stoffer R and Jobst G 2014 Broad-band Mach-Zehnder interferometers as high performance refractive index sensors: Theory and monolithic implementation *Opt. Express* **22** 8856–70
[98] Misiakos K, Raptis I, Makarona E, Botsialas A, Salapatas A, Oikonomou P, Psarouli A, Petrou P S, Kakabakos S E, Tukkiniemi K, Sopanen M and Jobst G 2014 All-silicon monolithic Mach-Zehnder interferometer as a refractive index and bio-chemical sensor *Opt. Express* **22** 26803–13
[99] Raz S R and Haasnoot W 2011 Multiplex bioanalytical methods for food and environmental monitoring *Trends Anal. Chem.* **30** 1526–37

9 APPENDICES

APPENDIX A

Table 9.1. Coupling coefficients for different lengths of the single mode and bimodal sections when the step junction is located in the sensing window using a λ of 633 nm.

Mode	L_{SMS} (μm)	L_{SMSSA} (μm)	L_{BMSSA} (μm)	L_{BMS} (μm)	η_{00}	η_{10}	Radiation pattern
TE	186.17	2500.5	8611.5	186.17	0.6167	0.2805	
TM	186.17	2500.5	8611.5	186.17	0.6863	0.1913	
TE (nom)	6500	550	14450	8550	0.6183	0.2786	
TM (nom)	6500	550	14450	8550	0.6394	0.2439	
TE	1029	550	15000	655	0.6277	0.2683	
TM	1029	550	15000	655	0.6294	0.2550	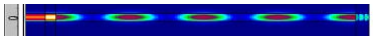
TE	1029	550	14450	655	0.6183	0.2786	
TM	1029	550	14450	655	0.6394	0.2439	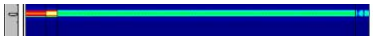
TE	1600	550	14450	550	0.6183	0.2786	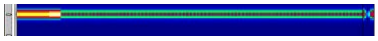
TM	1600	550	14450	550	0.6394	0.2439	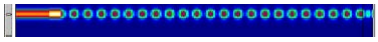
TE	650	550	14450	550	0.6183	0.2786	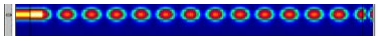
TM	650	550	14450	550	0.6394	0.2439	

Table 9.2. Coupling coefficients for different lengths of the single mode and bimodal sections when the step junction is located in the sensing window using a λ of 660 nm.

Mode	L_{SMS} (μm)	L_{SMSSA} (μm)	L_{BMSSA} (μm)	L_{BMS} (μm)	η_{00}	η_{10}	Radiation pattern
TE	186.17	2500.5	8611.5	186.17	0.6294	0.2661	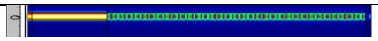
TM	186.17	2500.5	8611.5	186.17	0.6920	0.1737	
TE (nom)	6500	550	14450	8550	0.6294	0.2661	
TM (nom)	6500	550	14450	8550	0.6569	0.2142	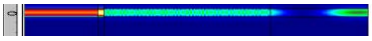
TE	1029	550	15000	655	0.6539	0.2391	
TM	1029	550	15000	655	0.6634	0.2068	
TE	1600	550	14450	550	0.6294	0.2661	
TM	1600	550	14450	550	0.6569	0.2142	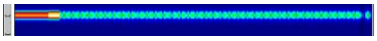
TE	650	550	14450	550	0.6294	0.2661	
TM	650	550	14450	550	0.6569	0.2142	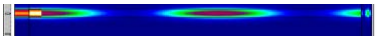

APPENDIX B

B.1 Protocol for fabrication of Microfluidic molds in SU-8.

The SU-8 molds were fabricated in clean room facilities, following the next protocol over 5 inches wafers. The selected material is SU-8 2005 from Microchem.

1. 3' Wafer dehydration, 20 minutes at 200° C.
2. O2 plasma activation, 18 seconds at 500 W.
3. Spin coating of a SU-8 2005 seed at 3000 rpm. 30 seconds.
4. Soft-bake to solidify and eliminate the solvent leftovers. 65 C to 95° C in 10'

NOTE: gradual cooling to avoid thermal stress.

5. UV curing by 9" at 11 $mWcm^{-2}$
6. Gradual cooling, 10' at 65°-95° C.
7. Deposition of 50 μm thick in wafers A and B: spin coating of SU-8 at 3000 rpm.
8. Deposition of 100 μm in wafers C and D: 1200 rpm SU-8-2050 (25').
9. Soft bake of 50 μm wafers (A and B) 1 hour and cooling.
10. Soft bake of 100 μm wafers (C and D), one and a half hour and then cooling.
11. Develop with 1-Methyl 2-Propil Acetate.
12. With hard develop for wafers A and B.
13. With soft develop for wafers C and D (100 μm).
14. Hard Bake. 1h 30'. From 65 to 120° C. Use N_2 atmosphere after 95° C.

B.2 Protocol of microfluidic cells fabrication in PDMS.

After fabrication and dicing of the SU-8 chips molds, the fluidic headers were fabricated in PDMS following the next protocol over individual chips with the SU-8 microfluidic patterns.

1. Firstly, it is necessary to uniformly stir a ratio of PDMS 1:10 (polymer/curing agent).
2. Place in the vacuum chamber until air bubbles are gone.
3. Bake one hour at 75° C in the oven.
4. Clean any organic debris by O_2 plasma (99% power, 45 SCCM), 90 seconds
5. Add PEG200 (1:1) in water: 100 µL total to enhance the chamber walls hydrophobicity.
6. Bake 25 minutes at 150° C in the oven, then rinse with ethanol.
7. Place tubes and PMMA holder.
8. Clean with SDS 0.5%, HCl 0.1 M and water when removing from setup.

PUBLICATIONS RELATED TO THIS DOCTORAL THESIS

1. ***"Direct and label-free hormone detection in urine by an ultrasensitive Bimodal Waveguide biosensor"***. A. B. González-Guerrero, J. Maldonado, S. Dante, D. Grajales and L. M. Lechuga. J. Biophotonics 1-7. **2016**. (IF: 3.8).

2. ***"Last Advances in Silicon-Based Optical Biosensors"***. A. Fernández Gavela, D. Grajales, J.C. Ramírez and L.M. Lechuga, *Sensors* 16, 285. **2016** (IF: 2.033)

3. ***"Optical Chirp Modulation of Bimodal Interferometric Waveguide Biosensors for Sensitivity and Readout Enhancements".*** D. Grajales, A. Fernández Gavela, J.R. Sendra and L. M. Lechuga. Submitted (2018)

4. ***"Low-cost Taper for high efficient light in-coupling in Bimodal Interferometric Waveguide Biosensors"***. D. Grajales, A. Fernández Gavela, C. Vilà, C. Domínguez, J.R. Sendra and L. M. Lechuga. Submitted to IOP Journal of Physics Photonics (2018)

5. ***"Optimization Study of Bimodal Waveguide Interferometric Biosensors"***. D. Grajales and L.M. Lechuga, Proceedings of the European Conference on Lasers and Electro-Optics 2015. (p. JSII_1a_2). Optical Society of America. Munich, Germany. **2015**.

6. ***"Simulation and Experimental Evaluation of Optical Chirp Modulation for Bimodal Waveguide Interferometer Biosensors"***. D. Grajales, J.R. Sendra and L.M. Lechuga, Proceedings of the European Conference on Integrated Optics Eindhoven, Netherlands. **2017**.

7. ***"Vertical adiabatic taper for efficient in-coupling in nano-interferometric waveguide biosensors"***. D. Grajales, A. Fernández Gavela, C. Domínguez and L.M. Lechuga, In Proceedings of the European Conference on Lasers and Electro-Optics 2017. (p. CL_4_1). Optical Society of America. Munich, Germany. **2017**.

CONFERENCES RELATED TO THIS DOCTORAL THESIS

1. ***"Implementation of a multiplexed Mach-Zehnder Interferometer Device for Biosensing Applications".*** **D. Grajales**. FAB10: Fab Festival Bio Hacking Panel and round table at FABLAB 10th congress. Moderated by Dr. Cristina Pujades. Barcelona, Spain. July 5th **2014**.
2. ***"Optimization Study of Bimodal Waveguide Interferometric Biosensor"*** **D. Grajales** and L. M. Lechuga. Oral presentation at the European Conference on Lasers and Electro-optics – European Quantum Electronics Conference. Optical Society of America. Munich, Germany. June 21st **2015**.
3. ***"Simulation and experimental evaluation of optical chirp modulation for bimodal waveguide interferometer biosensor"***. **D. Grajales**, J.R. Sendra and L. M. Lechuga. Poster presentation at European Conference on Integrated Optics. Eindhoven, Netherlands. April 3rd to 6th **2017. Best Poster Award** by OCLARO.
4. ***"Vertical Adiabatic Taper for Efficient In-coupling in Nano-interferometric Waveguide Biosensors".*** **D. Grajales,** A. Fernández Gavela, C. Domínguez and L.M. Lechuga. Oral presentation at the European Conference on Lasers and Electro-optics – European Quantum Electronics Conference 2017. Optical Society of America. Munich, Germany. June 25th to 29th **2017**.
5. ***"Multiplexed detection of alternative spliced mRNA isoforms for cancer detection using a bimodal waveguide interferometer".*** D. Grajales, C. S. Huertas and L.M. Lechuga. Poster presentation at VIII International Congress on Analytical Nanoscience and Nanotechnology 2017. Barcelona, Spain. July 3rd to 5th **2017**.
6. ***"Multiplexed photonic nanointerferometric biosensors in silicon nitride for ultrasensitive analysis".*** R. Guiu, D. Grajales, A. Fernández-Gavela, C. Domínguez and L. M. Lechuga. Poster presentation at European Conference on Integrated Optics. Valencia, Spain. May 30th to June 1st **2018**.

OTHER ACTIVITIES

1. Participation in the project: EPISENS Lab-on-a-chip integration of biophotonic devices to study gene expression alterations in cellular pathways. Barcelona, Spain. 2013 –2015.

2. Participation in the project ***"Interferometric Detection in Bimodal Waveguide" project***. Acción Estratégica Economía y Sociedad Digital (AEESD) and Ministerio de Industria, Energía y Turismo (MINETUR). Participants: PROMAX S.L. and ICN2. **2015 –2017.**

3. ***"9th Advanced Studies Course in Optical Biochemical Sensors"***. Summer school attendance. Porto, Portugal. July 22nd – 29th 2015.

4. ***"Biosensors and DIY Biotechnology for food detection"***. **D. Grajales**. Seminar to Veterinary School PhDs at UAB. Barcelona, Spain. May 28th 2015.

5. **"*Student in the mornings, biohacker at night"***. Oral presentation. D. Grajales in CSIC. Barcelona, Spain. November 14th 2016.

6. ***"Biohackers and the DIY biologist".*** **D. Grajales**. Oral presentation in 2nd Scientific Meeting of BNC-b students. *UAB, Barcelona.* June 29th 2016**. Second price for best oral presentation**.

7. "Aproximació Interferométrica als Dispositius de Biosensing Basats en Tecnologies de Guies d'ones Bimodales – o ¿Que hi fa un alumne de primer de batxillerat en un centre de recerca de nanotecnologia?" Mentorship and co-tutoring of student Albert Lopez Serrano during his summer stay at ICN2 as part of the program for talented students "Bojos per la fisic" in collaboration with IFAE (High Energy Physics Institute), ICN2, BIST, Fundació la Pedrera and DiY Bio Bcn. July – November 2016.

8. ***"Principis Fotonics per a Sensors"*** *– 2nd edition of "Bojos per la Física"* by **D. Grajales**, E. Martin, G. Lopez. Workshop building a Low Cost PM10 dust sensor with Arduino UNO WIFI and Thingspeak IoT cloud service in collaboration with IFAE (High Energy Physics Institute), ICN2, BIST, Fundació la Pedrera, DiY Bio. Barcelona, Spain. February 4th **2017**.

9. ***"Biohacker: Garage vs Institutional Science".*** **D. Grajales**. Invited talk at the first Talentia network of Mexican talents meeting. Mexican Consulate, Barcelona, Spain. March 31st **2017**.

10. Attendance at ***Sonar +D*** and ***Maker Faire Barcelona 2017*** showing a spirulina DIY bioreactor, DIY webcam microscopes and a dust sensor in collaboration with ICN2. Barcelona, Spain. June 16th – 18th **2017**.

11. Attendance to ***X, XI and XIII Mobile World Congress*** (**2014, 2015, 2017**) in the quest for IoT technologies for future integration.
12. Attendance to the "***Photonics Integration Week 2017"*** in Valencia, Spain. January 16th – 20th **2017**.
13. Attendance to the ***"Second workshop on PICS for Telecom and Bio/life sciences"***. Organized by PIC4TB, network of excellence in Spain. CTTC Castelldefells, Barcelona, Spain. October 26th -27th **2017**